

Stress-wave monitoring of erosive particle impacts

By

Stephen Phillip Allen, Bachelor of Engineering (Mechanical)

Submitted to

The University of Newcastle

For the degree of

DOCTOR OF PHILOSOPHY

November 2004

Statement of Sources

I hereby certify that the work embodied in this thesis is the result of original research and has not been submitted for a higher degree to any other University or Institution

Stephen Phillip Allen

Acknowledgements

I would like to give special thanks to the Cooperative Research Centre for Advanced Composite Structures (CRC-ACS) who provided funding for this project. The staff at CRC-ACS were friendly and offered many words of encouragement, in particular I would like to thank Stuart Dutton, Murray Scott, Ian Crouch and Rodney Thompson for advice and constructive comments. I was also privileged to work closely with Bruce Cartwright of CRC-ACS and Bruce provided many hours of technical advice and words of encouragement.

I would like to thank the technical staff at the University of Newcastle. The workshop staff led by Phillip Reddy provided materials and expertise. I would like to thank Ian Miller who provided many hours of expertise in the design, construction and implementation of electrical instrumentation.

I would like to thank my supervisor Dr Paul Dastoor of the Physics department for motivation and guidance. I would like to give a special thanks to my supervisor Professor Neil Page who I regard in the highest esteem. I met regularly with Professor Page and he gave me the guidance and encouragement to pursue the task, typical of his own professional manner.

I would like to thank my parents Bob and Jean and my sisters Janette and Vicki for their support and words of encouragement. Lastly, I would like to thank my wife Corinna, who supported me in times of need and who encouraged me all the way to complete the task.

Table of Contents

Statement of Sources	ii
Acknowledgements	iii
Table of Contents	iv
Abstract	viii
Nomenclature	xi
Published Works	xii
CHAPTER 1	1
INTRODUCTION	1
1.1 Introduction to Erosion	1
1.1.1 Erosion mechanisms	2
1.1.2 The physics of the erosion process	6
1.1 Stress-waves and the study of erosion	9
1.3 FEA and the study of erosion	10
1.4 Thesis Objective	15
1.5 Thesis Outline	15
CHAPTER 2	17
LITERATURE REVIEW	17
2.1 Introduction	17
2.2 Erosion models	18
2.1.1 Erosion models for ductile metals	18
2.1.2 Erosion models for polymers	22
2.2 FEA Material Models	26
2.2.1 FEA material model for AISI 1020 steel	27
2.2.2 Review of mild steel at high strain-rates	28
2.2.3 FEA material models for polymers	29
2.2.4 Review of ductile polymer at high strain-rates	32
2.3 Past erosion studies involving stress-wave monitoring processes	34
2.3.1 Literature review of stress-waves produced by small particle impacts	34
2.4 Chapter summary	36

CHAPTER 3	39
EXPERIMENTAL METHODS	39
3.1 Introduction	39
3.2 Considerations for stress-wave monitoring process	40
3.2.1 Stress-waves and wave dispersion	40
3.2.2 Study of stress-time profiles for an elastic and elasto-plastic impact	45
3.3 Piezo-electric transducer design	47
3.3.1 Considerations for the design of a piezo-electric transducer	47
3.3.2 Matlab computer program for the design of piezo-electric transducer	48
3.3.3 Results of Matlab simulations	49
3.3.4 Piezo-electric transducer design	50
3.3.5 Piezo-electric materials	53
3.3.6 Natural frequency response of the piezo-electric transducer	60
3.3.7 Electrical coupling considerations for the piezo-electric transducer	61
3.3.8 Application of piezo-electric materials to stress-wave monitoring	62
3.3.9 Consideration of a three-dimensional stress state at the wear material sensing element interface	64
3.3.10 Recording device considerations	65
3.3.11 Rise-time consideration of piezo-electric transducer response	65
3.4 Apparatus	67
3.4.1 Stress-wave monitoring apparatus	67
3.4.2 Particle velocity calculations	73
3.4.3 Clamping of the wear material to the piezo-electric transducer	73
3.4.4 Stress-wave monitoring chamber and gas-blast apparatus	74
3.4.5 Particle characterisation	76
3.4.6 Erosion testing	79
3.4.7 Mass loss measurements	85
3.5 Chapter summary	87
CHAPTER 4	89
FEA MODELLING OF STRESS-WAVES	89
4.1 Introduction	89
4.2 Impact modelling by the FEA method	91
4.2.1 Implicit and explicit FEA modelling	91
4.2.2 The LS DYNA FEA code	92
4.2.3 Axisymmetric modelling techniques	93
4.2.3 Mesh size considerations	94
4.2.4 Numerical stability of the FEA model	97
4.2.5 Mesh size consideration for elastic stress-wave motion	99
4.2.6 FEA modelling of contact	101
4.2.7 Equation of State	106
4.2.8 Spatial averaging considerations of FEA model	107
4.3 Chapter summary	110

CHAPTER 5	113
STRESS-WAVE MONITORING RESULTS	113
5.1 Introduction	113
5.2 Experimental and FEA study of impacts and stress-wave motion of AISI 1020 steel	114
5.2.1 Implementing the Johnson-Cook FEA material model	114
5.2.2 Experimental and FEA stress-wave monitoring study of AISI 1020 steel under low velocity impact conditions	116
5.2.3 Experimental impacts to AISI 1020 steel at higher impact velocities	122
5.2.4 Comparison of experimental and FEA stress-wave recordings of AISI 1020 steel under higher velocity impact conditions	124
5.2.5 Sensitivity study of FEA model parameters due to strain-rate effects	128
5.2.6 Validation of Johnson-Cook model by impact crater study	131
5.2.7 Sensitivity of strain-hardening terms under high strain impact conditions	134
5.2.8 Strain-rate of impacts extracted from FEA model	135
5.2.9 Stress-strain curves related to stress-wave monitoring	135
5.3 Experimental and FEA study of impacts and stress-wave motion to polymer wear surfaces	137
5.3.1 Introduction	137
5.3.2 Implementation of the FEA material model	138
5.3.3 Specimen manufacture	142
5.3.4 High velocity impact and FEA modelling of polymer materials	142
5.3.5 Impact crater study	145
5.3.6 Stress-strain curve obtained from FEA model	150
5.4 Chapter summary	152
CHAPTER 6	157
EROSION MODELLING	157
6.1 Introduction	157
6.2 Stress-wave monitoring results applied for the study of erosion	158
6.2.1 Energy based approach to erosion	158
6.2.2 Development of FEA solid model for the study of erosive impacts	161
6.2.3 Erosion testing procedure	165
6.2.4 Specimen manufacture and material properties	165
6.2.5 Temperature and strain-rate values obtained from FEA simulations	167
6.2.6 Erosion results compared with erosion model prediction	170
6.3 Chapter Summary	173

CHAPTER 7	175
DISCUSSION AND CONCLUSION	175
7.1 Important findings	175
7.1.1 Introduction	175
7.1.2 Piezo-electric transducer design	175
7.1.3 Stress-wave interpretation	176
7.1.4 Effects of stress-wave recording from piezo-electric transducer coupling	177
7.1.5 Stress-wave monitoring of erosive particle impacts	178
7.1.6 Implementation of stress-wave monitoring process for the study of erosion	179
BIBLIOGRAPHY	181
APPENDIX A	185
MATLAB PROGRAMS	185
A.1 Matlab programs	185
A.1.1 Matlab program for the design of the piezo-electric transducer	185
A.1.2 Matlab program to measure volume loss of wear specimens	188
A.1.3 Matlab program to compare experimental stress-wave recordings with FEA model prediction	190
APPENDIX B	193
LS DYNA FEA PROGRAMS	193
B.1 LS DYNA programs	193
B.1.1 LS DYNA input code for stress-wave monitoring FEA model	193
B.1.2 LS DYNA input code for FEA erosion modelling	195
APPENDIX C	199
MATERIAL PROPERTIES	199
C.1 Material property specifications	199
C.1.1 Material property data sheets for AISI 1020 steel	199
C.1.2 Material property data sheets for AISI 1006 steel	200
C.1.3 Material property data sheets for UHMWPE	201
C.1.4 Material property data sheets for VER	202
C.1.5 Material property data sheets for piezo-electric material	203

Abstract

The impact of a small particle with a wear surface can lead to very high strain-rates in the material being encountered. Often predictive erosion models are based on material property parameters taken from quasistatic test conditions. However, the material properties of the impacted wear surface can change dramatically with strain and strain-rate, leaving some doubt as to the validity of an erosion model based on quasistatic parameter values. In this study, a new stress-wave monitoring process is developed for the study of material characteristics and erosion phenomena, at strain-rates approaching 10^6s^{-1} . For this study a newly designed piezo-electric transducer was used to monitor the stress-waves produced by small erosive particle impact events. A computational study was also conducted to aid in the transducer design and location distance from the impact source by considering the effects caused by spatial averaging. Spatial averaging affects the recorded stress-wave signal and is caused by the curvature of the stress-wave as the wave passes through the flat piezo-electric sensing element.

This study was conducted using a computational and experimental approach. The joint study allowed significant knowledge to be gained for the study of elasto-plastic impact and stress-wave motion. Finite element analysis (FEA) was used to model the experimental system in detail. The stress-waves produced by the experimental process were directly compared to the FEA model. Once the FEA model was validated, detailed information from the impact event at the surface could be obtained from the model, which would otherwise be difficult if not impossible to obtain experimentally.

The issues of wave dispersion have been an underlying problem in the correct interpretation of stress-wave phenomena for many years. The impact of the wear surface causes stress-waves with many frequency components, each component propagating through the wear material at distinct wave velocities. Wave dispersion causes the initial stress-wave pulse to be dispersed into many waveforms. In this study the longitudinal stress-wave was the main waveform studied. FEA simulations were conducted for a purely elastic impact and an impact causing significant plastic deformation of the surface. A comparison between these waveforms showed that in the case of impacts causing plastic deformation, the initial part of the stress-wave, measured from the time

of arrival to the first peak, corresponded to the elastic stress component of the impact event at the surface. The characterisation of the waveform in regards to elastic and plastic stress components at the surface was significant for validating model parameters of the Johnson-Cook material model.

The stress-wave monitoring process was applied in the first instance to erosive particle impacts to AISI 1020 steel at impact velocities up to 104m/s. A specially designed erosion apparatus, fitted with a modified double disc system was used to impact the 10mm thick steel plate. The piezo-electric transducer was firmly clamped to the rear surface, directly behind the point of impact to obtain the stress-wave signals produced by impacts of 0.4mm zirconia spheres. The study showed that the contact interface of the wear material and the piezo-electric transducer could cause a phase change and amplitude reduction of the stress-wave transmitted to the transducer at wave frequencies above 0.9MHz. The results showed that the most likely cause for the phase shift to occur was the restriction of tensile stresses across the contact interface. For wave frequencies below 0.9MHz, no phase shift or amplitude reduction was apparent in the experimental stress-wave recordings.

The combined experimental / FEA study was shown to be able to validate the strain-rate parameter of the Johnson-Cook model. The parameters, which could not be validated by the stress-wave monitoring process, were the parameters relating to plastic deformation of the surface, which were the strain-hardening terms of the Johnson-Cook model. These terms were later validated by studying the extent of plastic deformation at the surface, which occurred in the form of impact craters. By comparing the predicted impact crater depths from the FEA model with the experimental results, the strain-hardening parameters of the Johnson-Cook model could be validated.

The robustness of the stress-wave monitoring process was proven for the impact study of ultra high molecular weight polyethylene (UHMWPE) and vinyl ester resin (VER). Unlike AISI 1020 steel, little is known about the high strain-rate response of these polymers. Initial estimates of material property parameters were made by applying computational *curve fitting* techniques to the stress-strain curves of similar polymers, which were from published results obtained from split Hopkinson's pressure bar method. The impact and stress-wave study showed UHMWPE and VER to be highly

sensitive to strain-rate effects. The main effect was a substantial increase in hardness with increasing strain-rate and it was considered that the hydrostatic stress component contributed to the strain hardening of the polymers.

The stress-wave monitoring and FEA computational techniques developed in this study were implemented in the development of an improved erosion model. The model form is similar to that of the well-known Ratner-Lancaster model. The Ratner-Lancaster model assumes wear rate to be proportional to the inverse of deformation energy, where deformation energy is approximated as the product of the ultimate stress and ultimate strain. The improved Ratner-Lancaster model uses the Johnson-Cook model to obtain the von-Mises stress as a function of strain. The area integral of the stress-strain curve is used to derive the deformation energy capacity of the material in the deformed zone close to the surface. The model accounts for strain, strain-rate and thermal effects and is therefore more soundly based on material deformation characteristics valid for erosion events than the Ratner-Lancaster model assumptions. The model developed in this work was applied to the erosion study of 1020 steel, UHMWPE and VER, with good correlation being obtained between experimental erosion rates and model predictions.

Nomenclature

Quantity symbol	Term	Unit symbol	First text reference
<i>a</i>	The angle of the particle trajectory relative to the wear surface	Degrees	2.1.1
<i>H</i>	Material hardness	Pa	2.1.1
<i>m</i>	Mass	kg	2.1.1
<i>W</i>	Wear or erosion rate	mm ³ g ⁻¹	2.1.1
<i>r</i>	Density	Kg m ³	2.1.1
<i>V</i>	Velocity	m s ⁻¹	2.1.1
<i>E</i>	Energy	N m	2.1.1
<i>s_u</i>	Ultimate stress, defined by the stress at the point of failure	Pa	2.1.2
<i>e_u</i>	Ultimate strain, defined by the strain at the point of failure	Dimensionless	2.1.2
<i>m</i>	Coefficient of friction	Dimensionless	2.1.2
<i>s_{yield}</i>	Yield stress	Pa	2.1.2
<i>e_{yield}</i>	Yield strain	Dimensionless	2.1.2
<i>e_p</i>	Plastic strain	Dimensionless	2.2.1
<i>ė</i>	Plastic strain-rate	s ⁻¹	2.2.1
<i>T</i>	Temperature	Degrees C	2.2.1
<i>s_f</i>	Flow stress	Pa	2.2.2
<i>n</i>	Poisson's ratio	Dimensionless	3.1.1
<i>c_{el}</i>	Bulk elastic wave speed	m s ⁻¹	3.1.1
<i>E_T</i>	Plastic or tangent modulus	Pa	3.1.1
<i>V_{out}</i>	Output voltage	Volts	3.2.2
<i>X</i>	Electrical impedance	Ohms	3.2.5
<i>s_y</i>	Stress in the y direction	Pa	3.2.8
<i>B_m</i>	Elastic bulk modulus	Pa	5.2.1
<i>G</i>	Shear modulus	Pa	5.2.1
<i>C_p</i>	Specific Heat	J/kg K	5.4.1

Published Works

Journal Papers

Cenna A. A, Allen S. P, Dastoor P, Page N. W, (2002) "Modelling the three-body wear of UHMWPE particle reinforced composites" *Wear* Vol 254, pages 581-588

Cenna A.A, Allen S.P, Page N.W, Dastoor P, (2001) "A polyethylene-reinforced polymer composite abraded by bulk solids." *Wear* Vol 249 Pages 663-671 Refereed Conference Papers

Allen S. P, Page N. W, Dastoor P, (2002) "Stress-wave monitoring of individual particle impacts during erosion tests." *Proceedings of the 6th International Tribology Conference*. Published by Fineline, Perth WA. Volume 1 Pages 235-239

Allen S.P, Cenna A.A, Page N.W, Dastoor P, (2001) "Abrasive wear of PTFE and PTFE/UHMWPE particle reinforced vinyl ester resin by bulk solid material". Presented at the 7th International Conference on Bulk Materials Storage and Handling and Transportation. Vol 2 pages 50

CHAPTER 1

INTRODUCTION

1.1 Introduction to Erosion

Impacts at low velocity occur in a wide range of industrial applications. In the low velocity range up to 30m/s, erosive particle impacts occur in equipment used for the pneumatic conveying of bulk solids. In the mining industry, impacts occur as a result of falling bulk solid materials to various bulk solids containment equipment such as hoppers, bins and silos and transportation equipment such as dump trucks and railway wagons. At moderate velocities (up to 100m/s), impacts occur to the leading edges of wind turbine blades from dust particles swept up by wind and in pneumatic conveying equipment from particles entrained in the gas stream. At higher impact velocities (up to 800m/s), impacts occur to jet engine turbine blades, helicopter rotor blades and the leading edges of cruising jet and military aircraft from suspended dust particles, water droplets and ice crystals in the atmosphere.

Repeated impacts can cause damage to the surface in the form of plastic deformation, crack propagation or material fatigue failure. When material removal occurs through these mechanisms, erosion is said to occur.

The costs to industry from erosion of surfaces by solid particle impacts can be considerable. Continued erosion of a surface will ultimately result in loss of strength, lowering of the original design performance standard and lowering of safety standards. Materials commonly used in erosive environments are metals and metal alloys. However, there is growing interest in polymers and polymer composites in special applications. Metallic materials are often used for large-scale structures for the mining, storage and transportation of bulk solid materials. Also, metals and metal alloys are

used for machine components for example as jet turbine blades, pump impellers and housings, and in many other erosive environment applications. Polymer composites are being increasingly used for applications where their strength to weight ratio or chemical inertness creates a distinct advantage over metals; where typical uses are found in aircraft structural and fuselage applications, wind turbines blades and chemical processing applications.

Polymeric and elastomeric protective treatments are often used in industry to protect less erosion resistant structural components and machine parts from the effects of erosive impacts. Ultra high molecular weight polyethylene (UHMWPE) is one example of a polymer, which is widely used, in the mining industry for the lining of the walls of hoppers, bins, silos and dump trucks. Polyurethane is an example of an elastomeric material, which is widely used as a spray on or thin film protective treatment. Typical examples for the use of polyurethane can be found in the automotive industry as a chip resistant protective layer over painted body panels, as a spray on coating to increase wear resistance for slurry pipes and in the airline industry where polyurethane film is used for the protection of aircraft radomes and leading edges.

The erosion performance of polymers and polymer composites is still a relatively unexplored field of research. In the past, dating back some fifty years, much of the attention of impact and erosion studies has focused on metallic materials. The reason for this is that metallic materials were more widely used as structural materials than polymers were. However, with the increasing development of polymer composite technology, advantages can be gained in the form of wear resistance, strength to weight ratio and costs. These advantages now see polymer and polymer composite materials being considered more widely as replacements for more traditional metallic materials in applications where their properties provide an advantage.

1.1.1 Erosion mechanisms

Erosion mechanisms are broadly categorised as either ductile or brittle. In general, the mechanical properties of engineering materials depend on temperature, strain and strain-rate. At commonly experienced loading conditions, examples of ductile materials include mild steel, aluminium, brass and thermoplastic polymers such as nylon and

UHMWPE. Likewise, examples of brittle materials include glass, high carbon steel, ceramics and some thermosetting polymers.

For ductile and brittle materials, the material removal mechanism is strongly dependant on the particle impact angle. Figure 1.1 shows characteristic erosion rates as a function of impact angle for ductile and brittle materials, where the dimensionless erosion rate in figure 1.1 is defined as the ratio of mass loss to the mass of the impacting particle. In general, ductile and elastomeric materials show lowest erosion rates at high impact angles. The resistance to erosion as a result of high impact angles is due mainly to the energy absorption qualities of the material where, for elastomers, the impact energy is absorbed as elastic strain energy whilst tough ductile materials absorb impact energy by elasto-plastic deformation of the wear surface. Harder more brittle materials perform better at lower impact angles mainly because, at lower impact angles, particle penetration is lower, which minimizes the effects of cutting and chip removal from the surface.

In many past erosion studies, the erosion rate is defined as the ratio of volume loss to the mass of impacting particles. By using this method, it allows more even comparisons to be made between materials of varying density. In this study, steel and polymer wear surfaces are considered. The volume loss approach is therefore more ideally suited for this study and was adopted in later Chapters.

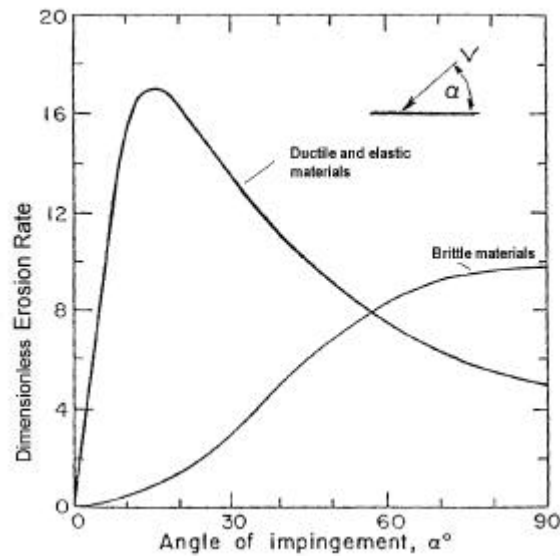


Figure 1.1 Typical erosion curves for ductile and brittle materials as a function of impact angle α . After Finnie (1995)

Figure 1.2 shows the erosion performance of some engineering materials over a wide range of impact velocities at normal impact angle. As shown for the materials considered, by far the best performer is rubber up to 150m/s, and then followed by mild steel. For normal impact situations, rubber makes an excellent choice, however rubber has very little structural strength and is therefore limited as a lining material only. Conversely, fiberglass (GFRP), which is widely used as a structural material shows poor erosion resistance and requires a lining or coating to prolong erosive wear life.

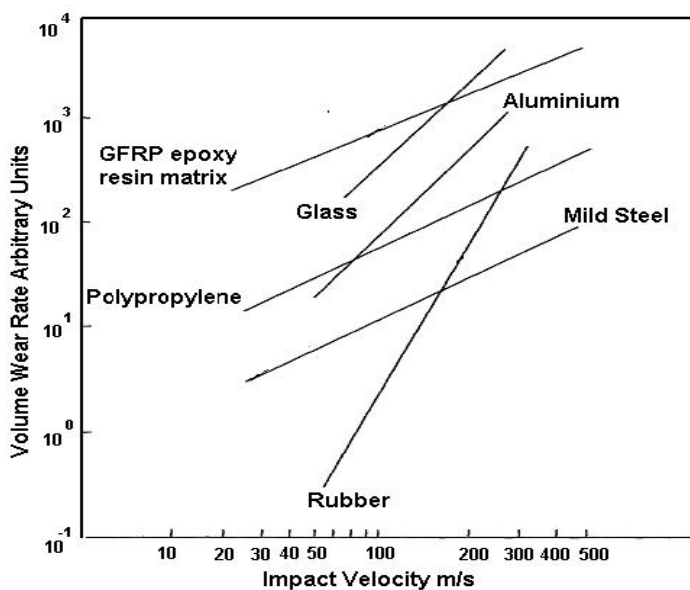


Figure 1.2 Erosion resistances of various engineering materials according to impact velocity; impact by 125 μ m silica particles at 90 $^{\circ}$. After Waterman *et al*, 1997

Other important parameters, which determine erosive response of wear surfaces, are; particle size, particle angularity, impact velocity, flux and operating temperature range and these parameters can vary significantly depending on the application. In previous erosion studies it has been found that the erosion rate of materials can be influenced by particle size. Erosion studies of aluminum and aluminum alloy by Tilly (1969) showed that the erosion rate W increased almost linearly, when plotted on a log-log scale, up to the particle size of $100\mu\text{m}$ where a plateau was reached (as shown in figure 1.3) and then the erosion rate was independent of particle size. The linear region is consistent with a power-law relationship between the parameters over this range. However, in the same study epoxy resin did not show the same plateau effect and showed a nearly linear relationship between erosion rate and particle size when plotted on log-log axes.

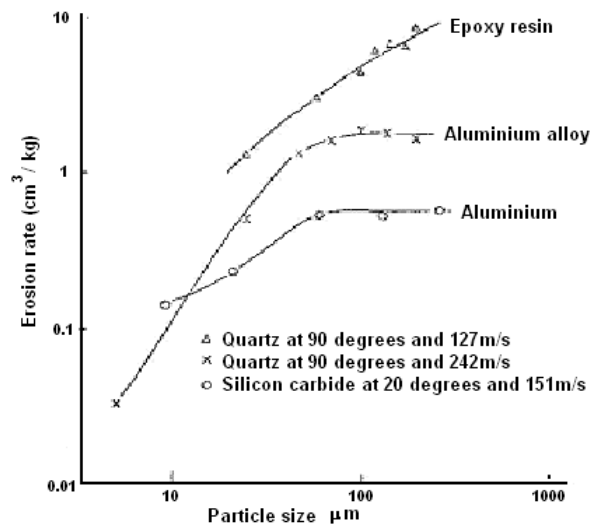


Figure 1.3 Erosion rate of aluminium and epoxy resin as a function of particle size. After Tilly (1969)

The influence of impact velocity to erosion rate is an important consideration for many erosion applications. Finnie (1960) found that the erosion rate for ductile metallic materials as a function of impact velocity could be described by a simple power law equation as

$$W = bV^n \quad (1.1)$$

where b is a constant and n ranged from 2 to 2.44 depending on the material used. Typical values for aluminium were 2.26, AISI 1045 steel 2.23 and tool steel 2.35.

1.1.2 The physics of the erosion process

The simplest impact situation to gain a physical understanding of the deformation leading to erosion is to consider the normal impact of a rigid sphere impacting a ductile steel wear surface. The deformation of the material can be modeled as two distinct zones where material plastic flow is likely to be high or low. Zone 2 in the figure 1.4 represents the material, which has undergone bulk deformation at relatively slow strain-rates and would be similar to the deformation zone produced by a static hardness indent. In zone 2 the material is constrained by the bulk material surrounding the deformation zone. In zone 1 however, the material is not as constrained, and this allows much more dynamic shear deformation to occur, which can also be intensified by localized heating. Levy (1981, 1986), describes the region of zone 1 as platelet formation, which is essentially formed by an extrusion process between the cold-work hardened region of zone 2 (the anvil) and the impacting particle (the hammer). The platelet is then subsequently forged by repeated impacts until finally it fractures off, causing erosion to occur. This process is typical of the shot peening process often used in industry for de-scaling, or alternatively surface strain-hardening of metal components.

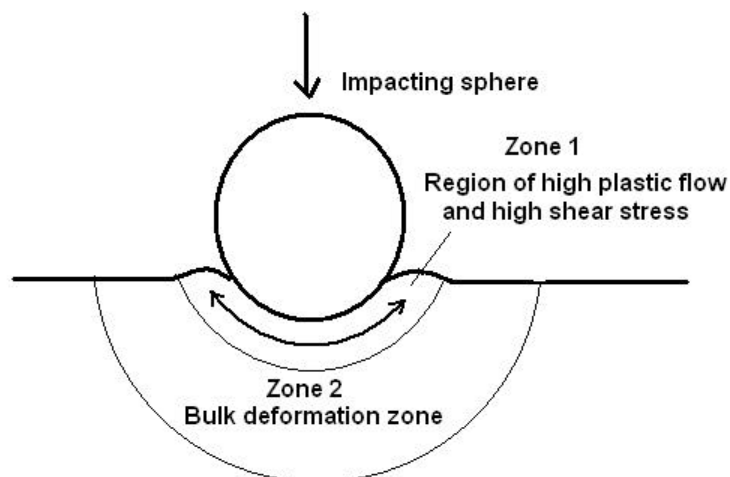


Figure 1.4 General characteristic shape of an impact crater produced by a normal impact of a spherical particle with a ductile metal surface

The simple model can be extended to oblique angle impacts as shown in figure 1.5. Shewmon *et al* (1983) considered the oblique impact of a rigid sphere with a ductile steel wear surface and noted that it is the lip volume of zone 1 which is the important parameter in erosion models, as this highly strained region of the impact crater is more likely to be detached by subsequent impacts on or near the lip area. Sundararajan (1983) found that the lip volume could also vary independently of the crater volume, where a maximum is reached at some intermediate impact angle, presumably the angle corresponding to maximum erosion.

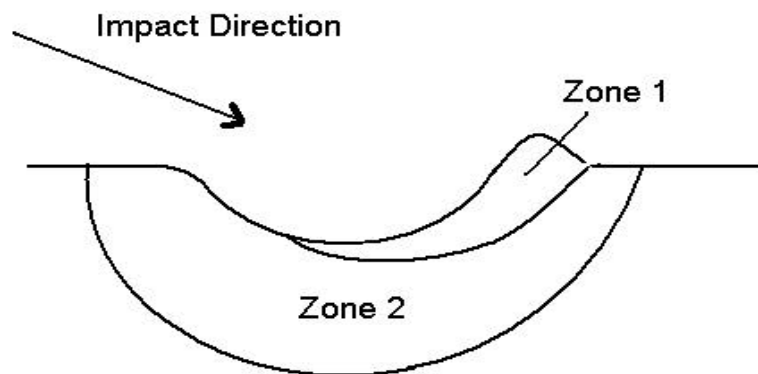


Figure 1.5 Schematic cross section of oblique impact crater of a ductile steel wear surface. Zone 1- dynamic shear, zone 2- slow compression. After Shewmon *et al* (1983).

Extending now to angular particle impacts, Winter *et al* (1974), studied material removal mechanisms of ductile steel specimens by single angular particles and considered the rake angle, defined by the angle of the leading edge of the particle with the wear surface as a defining parameter of ductile material removal. For particles of high rake angle (figure 1.6a), the impacting particle caused micro-cutting action as the leading edge of the particle dug and rotated into the wear surface, producing a raised prow, which could be detached by subsequent impacts on or near the prow as illustrated in figure 1.7a.

Winter *et al*, also detected adiabatic shear bands, by etching the cross-sectional impact craters and raised prows. Adiabatic shear bands are caused by intense heat where deformation becomes concentrated and occurs along shear planes. These shear planes are clearly visible when the cross section of the etched crater and prow formation is viewed under a microscope. The temperature rise in the prow region was estimated at 1000K at the strain-rate of $5 \times 10^5 \text{s}^{-1}$, which is clearly high enough to cause thermal softening effects and adiabatic shear planes to occur. For particles of smaller or negative rake angles (figures 1.6b & c), ploughing of the wear surface occurred by plastic flow causing material to be pushed ahead and to the sides of the impacting particle, as shown in figures 1.7b and 1.7c. This process leads to crater and lip formation, or as described earlier by Levy (1981, 1986), the mechanism of platelet formation.

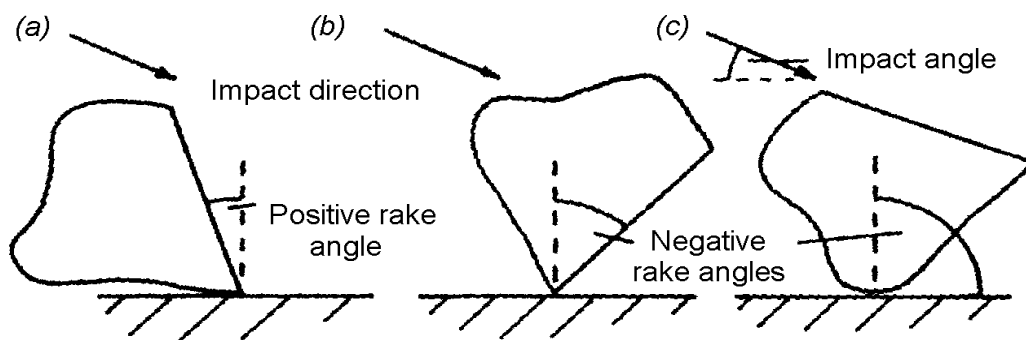


Figure 1.6 Rake angle defined by the angle of particle leading edge with the wear surface. After Winter *et al* (1974).

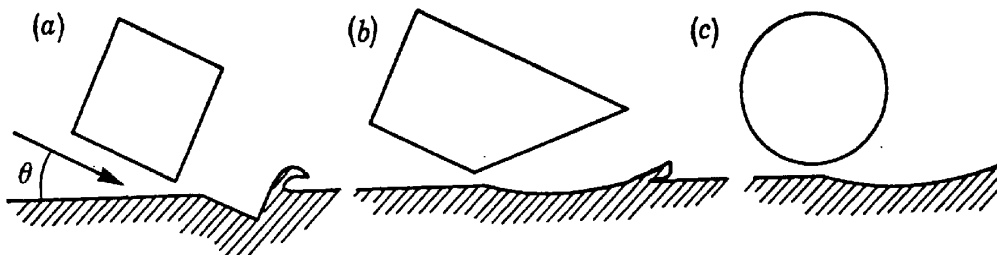


Figure 1.7 Impact of angular and spherical particles having (a) large rake angle and producing cutting mechanism (b) & (c) small rake angle, producing ploughing mechanism. After Hutchings *et al* (1975)

1.1 Stress-waves and the study of erosion

Erosion is a complex phenomenon, which can depend on many variables. However the modelling aspect of erosion does not need to be complicated. In the past, erosion models have relied basically on quasistatic mechanical testing to obtain material properties such as; hardness, yield strength, ultimate tensile strength and ultimate strain for the development of erosion models. However, material property values can change dramatically under high strain-rate impact conditions typical of erosive environments and this can lead to serious deficiencies in the development of an erosion model.

The main limiting factor for erosion studies is how to measure material properties at strain-rates encountered in erosive impact conditions, which can typically be in the order 10^6s^{-1} (Field and Hutchings in Blazynski, 1987) [‡]. The difficulties involved are the small size and velocity of the erosive particle, which can typically range between 10-500 μm diameters and impact velocities ranging from 5-800m/s. On this scale it is difficult to monitor single particle / surface interactions as visual techniques such as high speed photography and laser velocity measurements do not have either the required temporal or spatial resolution. However, stress-waves, which are initiated from the particle impact event, may be a useful tool for recording the time history of the particle / surface interaction and obtaining dynamic material properties of the wear surface.

In this study, it is proposed to monitor the stress-waves produced by small spherical particle impacts. The purpose of using spherical particles is to obtain an idealized system, which can be more easily modelled, for instance by the FEA method. Once the wear surface material properties are ascertained by the stress-wave monitoring method, angular particle and oblique particle impacts, which represent more severe erosion conditions, can be studied in more detail.

[‡] Based on normal impacts by 100 μm spherical particles, impacting mild steel at 100m/s

In the study, a piezo-electric transducer was designed and built especially for stress-wave monitoring purposes. Calibration of the newly designed piezo-electric transducer was conducted using a simple reference case of the normal impact of a sphere onto a flat steel wear surface. Experimental and computational (using FEA) studies were conducted around the impact of 0.5mm steel spheres to mild steel at an impact velocity of 2.5m/s. Stress-wave monitoring of impacts using 0.4mm zirconia spheres, at velocities up to 104m/s are then studied. The stress-waves produced under the higher velocity impact conditions are from impacts causing erosive damage to the steel and polymer specimens at strain-rates in the order of 10^6s^{-1} .

The study of stress-waves for material characterisation at high strain-rates is not a new field of study. With the advancement of experimental studies involving the split Hopkinson's pressure bar (SHPB), stress-strain curves can be obtained for a test material from stress-wave histories on either side of the test specimen. Results can be obtained at strain-rates up to 10^4s^{-1} , when a conventional 25mm diameter bar is considered. The main limiting factor to achieving higher strain-rates in SHPB experiments are the effects of wave dispersion caused by lateral inertia effects (Kolsky, 1953).

The development of a new experimental stress-wave monitoring technique to obtain material properties above strain-rate limitations of SHPB method would be a significant advancement in the study of materials at high strain-rates

1.3 FEA and the study of erosion

Finite element analysis (FEA) offers the freedom of being able to model erosive impacts using a variety of material models. FEA is also an ideal tool to study stress-wave motion including wave dispersion effects. This makes FEA ideally suited to conduct a joint experimental / computational study of erosive particle impacts and the consequential stress-wave motion and material deformation arising from the impact event.

An erosion model is essentially a model describing the erosion rate according to the relevant material property parameters contained in the model. Similarly, an FEA material model is essentially a model that will describe the physical deformation characteristics and failure mechanism of a material for use by computational FEA method. Similar parallels exist between an erosion model and an FEA material model. This close relationship allows the understanding of the erosion process to be enhanced by also considering FEA as a valid tool for the study of high strain-rate impacts, causing erosion.

The combined experimental / FEA stress-wave monitoring process developed in this study is ideally suited for

- Validating the structure of FEA material models
- Validating material property parameters of the FEA material model
- Developing new FEA material models / erosion models

Already, a vast knowledge base of FEA material models exists, which are designed specifically for high strain-rate impact study. In particular, the Johnson-Cook model (1983) is widely regarded as a suitable FEA material model for high strain-rate impact loading of steel materials.

The challenging aspect of implementing the use of FEA for this study is the small size of the impacting particle (0.4mm) relative to the size of the impacted plate (10mm thick). The analysis of small particle impact events by stress-wave methods is simplest if the time of contact is shorter than or comparable with the time required for repeated reflections of stress-waves to return to the impact point. This is why the impacted plate needs to be large so that wave reflections from the boundaries do not interfere with the stress-wave recording process. The size disparity between the impacting particle and the wear plate places considerable demands on developing the FEA mesh to firstly account for the deformation zone, which must have a fine mesh to correctly model surface deformation and secondly to model stress-wave motion through the bulk material. Correct modelling of surface deformation, which is the primary driver of stress-wave motion, will be an extremely important aspect of the FEA impact and stress-wave study.

In order to achieve the correct mesh size in the contact zone, elastic theory was used to verify FEA results of surface deformation under low velocity impact conditions.

The initiation of stress-waves from the impact event is not restricted to the wear surface. Multiple wave reflections will also occur within the impinging particle. However, the small size of the particle means that these reflections will occur on a timescale that is much shorter than that associated with the stress-wave travelling through the wear surface. Moreover, the fact that there will be a superposition of reflections from the entire particle surface, and that the small area of contact between the particle and the wear surface, would suggest an extremely low transmission of stress-waves from the impacting particle into the wear material.

The impact of the wear surface causes many frequency modes of stress-wave motion, with each frequency mode having its own characteristic phase velocity. The differing phase velocities of the stress-wave waveform means the initial stress-wave pulse emanating from the impact site at the surface cannot travel through the impacted medium without some form of wave dispersion occurring (Goldsmith, 1960). Wave dispersion will result in the initial stress-wave pulse to be separated into smaller wave pulses. The issues of wave-dispersion become more complex for impacts involving plastic deformation of the surface (as will be discussed in detail in Chapter 3). In this case an elastic wave and a plastic wave will emanate from the impact site. To introduce and visualize the effects of wave-dispersion, figure 1.8 shows an FEA simulation of stress-waves produced by the impact of a 0.4mm sphere to a AISI 1020 steel wear surface at 104m/s [‡]. As shown, stress-wave activity is dispersed throughout the thickness of the plate. The longitudinal stress-wave has the fastest phase velocity and is first to arrive at the piezo-electric transducer followed by the slower moving shear wave.

[‡] FEA analysis of impact by 0.4mm zirconia particle to 1020 steel at 104m/s. Input parameters for the FEA model available in chapter 5, tables 5.1 and 5.2

Since the longitudinal wave is the fastest moving wave it is not affected by slower moving wave activity and this allows the wave to be studied in detail without other influencing factors being involved. The main aim of studying the longitudinal stress-wave is to develop an understanding of how the wave can be related to surface material properties and ultimately erosion.

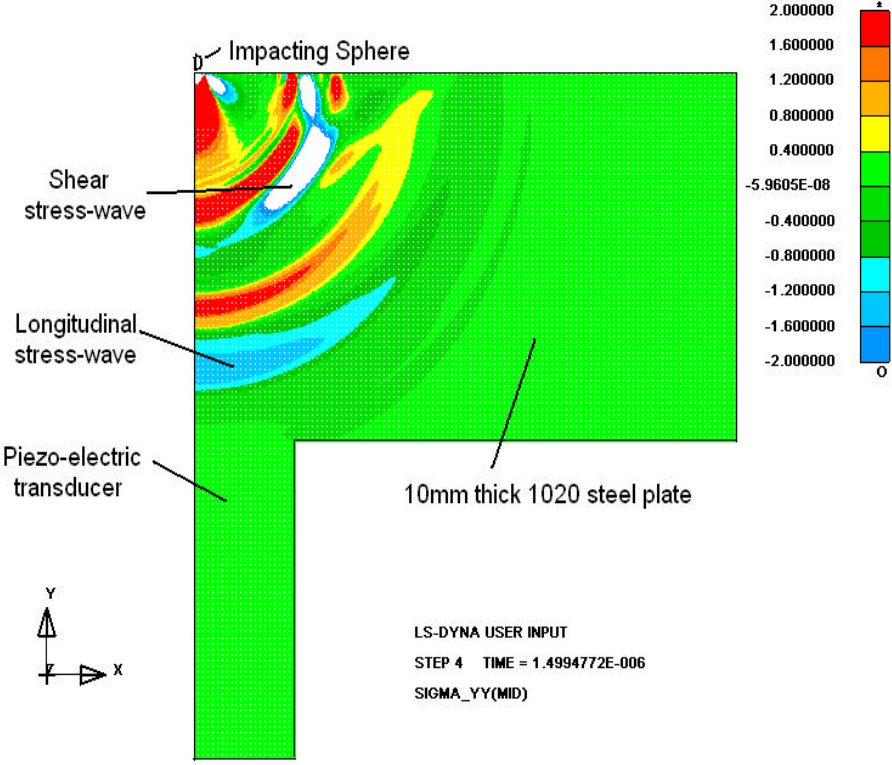


Figure 1.8 FEA simulation of impact and stress-wave motion produced by impact to AISI 1020 steel at 104m/s, compressive stress shown as negative on scale.

This page left intentionally blank

1.4 Thesis Objective

The intention of this work is to develop a method whereby the erosion process can be better understood. The objectives of this thesis are to enhance the knowledge and understanding of:

- Stress-waves initiated by small particle impact events
- Design of piezo-electric transducer for stress-wave monitoring purposes
- FEA modelling techniques for the study of impacts, stress-wave motion and erosion phenomena
- Material property characterisation at high strain-rates typical of erosive environments
- Stress-waves related to erosion phenomena
- Building more accurate models to predict erosive wear, and provide better guidance as to the design of materials to resist that wear.

1.5 Thesis Outline

Chapter 2 is devoted to reviewing the relevant literature and shows the progression towards the thesis objectives. In section 1, some past erosion models of ductile metals and polymers are reviewed. The next section of Chapter 2 is devoted to reviewing past studies involving materials at high strain-rates. In this section the Johnson-Cook material model is introduced and discussed for later use for the FEA simulations of Chapters 5 and 6. The last section of Chapter 2 focuses on past attempts of monitoring small particle impacts by stress-wave method.

In Chapter 3, the experimental methods are developed. In section 1, the issues arising from wave dispersion are discussed. Knowledge and understanding of wave dispersion will be essential background information not only for the design of the piezo-electric transducer, but also how the stress-wave recording can be related to the contact stresses at the surface. In section 2, the issues involving the design of the piezo-electric transducer are discussed. In this section a computational study is conducted to aid in the design and placement of the piezo-electric transducer. In the last section of Chapter 3, the apparatus used for the experimental stress-wave and erosion study are explained in detail.

In Chapter 4 the challenging issues surrounding the modelling of small particle impacts and stress-wave motion by FEA methods are discussed. The LS DYNA code was used in this study to model the impact of a sphere with the wear surface and for oblique impacts by angular particles (Chapter 6). The challenging issues in developing the FEA models were the small size of the impacting particle (0.4mm) relative to the size of the wear surface (10mm thick). The size disparity meant that a fine mesh at the impact zone was required to accurately model surface deformation. Also discussed in this chapter are the effects of numerical instability associated with the monitoring of stress-wave motion. Numerical instability caused high frequency *noise* to be encountered in some stress-wave results. The possible causes of numerical instability are discussed.

Chapter 5 contains the results of the experimental / FEA impact and stress-wave study of the steel and polymer materials respectively. This Chapter contains interpretation and discussion of results. In the first section, experimental results are discussed for low velocity impacts to the AISI 1020 steel wear surface. The low velocity impact experiments represent an experimental system, which can be more readily modelled by the FEA method. Results are then presented for higher velocity spherical particle impacts (up to 104m/s) to AISI 1020 steel, ultra high molecular weight polyethylene (UHMWPE) and vinyl ester resin (VER). The higher velocity impacts are typical of erosive impact events, occurring at very high strain rates. The combined experimental/FEA modelling is designed to determine material property parameters of the materials at strain rates in the order of 10^6s^{-1} .

In Chapter 6, the results obtained from the stress-wave monitoring sections are implemented for the study of erosion. In this Chapter an FEA model is developed for the study of angular and oblique particle impacts. An improved version of the Ratner-Lancaster model is developed and a comparison is made between experimental erosion rates and erosion model predictions.

Chapter 7 contains the summary and final conclusions of all major work presented in this thesis.

CHAPTER 2

LITERATURE REVIEW

2.1 Introduction

This Chapter is divided into three main sections. In section 1, a review is presented on past erosion models relating to ductile metals and polymeric materials. As will be shown, the erosion models presented are primarily based on material property parameters and the review therefore defines the important material parameters relating to the study of erosion.

The second section of this Chapter is devoted to the deformation characteristics of metal and polymer materials under high strain-rate loading conditions. In order to use FEA modelling techniques effectively, in particular the selection of a suitable FEA material model, the deformation characteristics of these materials under high strain-rate conditions needs to be considered. In this section, the Johnson-Cook material model is introduced for later use in Chapters 5, for the impact and stress-wave study of AISI 1020 steel, UHMWPE and VER.

In the last second section of this Chapter, the literature is reviewed relating to past studies of stress-waves resulting from small particle impacts. The limited amount of material in this area illustrates the novelty of the current study to provide valuable insight into using stress-waves for the study of erosive particle impacts.

2.2 Erosion models

2.1.1 Erosion models for ductile metals

Finnie (1960) was an early pioneer in the study of erosion and the first to introduce the theory of erosive wear for ductile materials subjected to low grazing impacts by angular particles. Microscope images of the eroded steel wear surfaces, which were studied by Finnie, showed that some particle impacts removed a chip from the wear surface whilst other impact sites showed material piled up at the sides or at the end of the impact crater. The Finnie model developed from these observations is applicable to ductile metals such as mild steel and aluminium. Aspects of the model may also be applicable to the wear process of polymers and it is therefore worthy to present the model here in brief form, i.e. without extended calculations.

The theory behind the model assumes that a hard angular particle, impinging on a smooth surface with an angle of attack α , will cut into the surface, much like a sharp tool. Figure 2.1 shows the protruding tip of a particle, which plows a trajectory (x_t, z_t) into the ductile surface. As the centre of mass of the particle translates and rotates the tip of the particle pushes material to form a raised prow ahead of the impacting particle. A chip is removed if the rotation of the particle is sufficient to cause the particle tip to meet the wear surface.

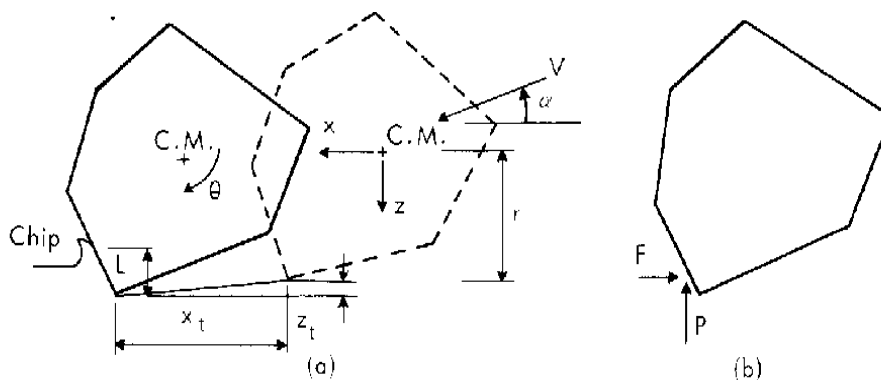


Figure 2.1. Impact of a particle cutting into a ductile wear surface at an angle of attack α , (a) Cutting geometry; (b) Contact forces acting on the particle during cutting. After Finnie, 1960

By using Newton's second law and solving the equations for the three components of motion, x , z and \mathbf{q} , the resultant prediction for the volume of material removed is given by Finnie as:

$$W = \frac{km^2V^n}{H} f(\mathbf{a}) \quad (2.1)$$

where m is the mass of abrasive particles impacting the wear surface, H is hardness, n is the velocity exponent, which typically lies between 2.2-2.4 for mild steel, and k is a constant related to the efficiency of material removal by impacting particles.

The dependence of the Finnie model on the impact angle \mathbf{a} is best described by considering the physics of the impact event. At low impact angles (below 20°), material is more likely to be swept out by the impinging particle. Moving to higher impact angles, just beyond the angle of maximum erosion, the particle comes to rest in the surface whilst cutting, producing a raised prow ahead of the particle. In the raised prow region, material is more likely to be vulnerable to removal by subsequent particle impacts.

The best *curve fit* for relating the erosion rate to impact angle \mathbf{a} is obtained using the function, $f(\mathbf{a}) = \cos^2\mathbf{a}$ as shown by the dashed line in figure 2.2. However, this relationship predicts no erosion at normal impact angle, so in a sense, the functional relationship is best described between impact angles of 20 - 45° . Finnie (1995) also points out that once the surface is roughened by normal impacts, a range of surface angularity is possible and erosive wear can also proceed by an oblique impact erosion process i.e. by cutting and ploughing mechanism.

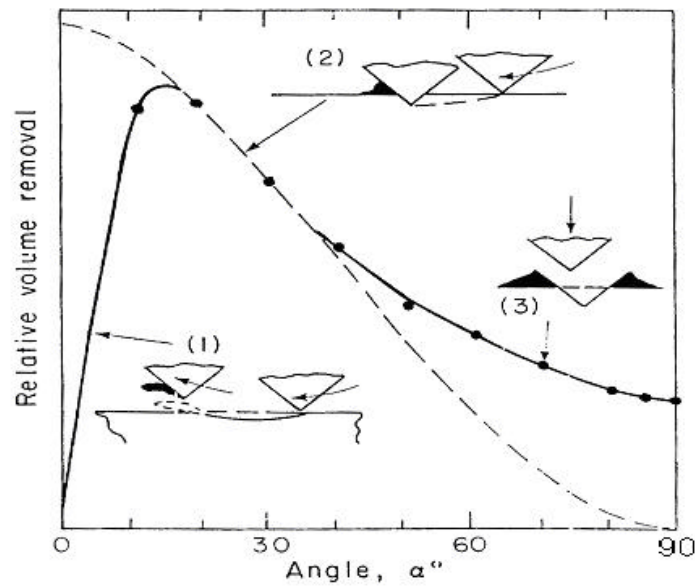


Figure 2.2 Predicted variation of volume removal for ductile metals as a function of impact angle ($f(\alpha) = \cos^2 \alpha$ dashed line) and experimental values (solid line) normalized to same values of maximum erosion. After Finnie, 1995

Of the models, which may be used to characterize materials for wear resistance, the Rabinowicz (1965) model must be one of the simplest to apply. The model predicts the wear rate W to be inversely proportional to surface hardness H .

$$W = \frac{1}{H} \quad (2.2)$$

Hardness is essentially a measure of resistance to penetration. The simple model applied to erosion suggests that the penetration of the impacting particle will define the extent of erosion. As presented in chapter 1, cutting and ploughing mechanisms essentially cause erosion of ductile materials. As explained, as penetration of the wear surface by the impacting particle occurs, material will be raised around the area of particle penetration. It is the highly strained raised material (prow), which will be more prone to material removal. The simple Rabinowicz hardness model portrays a valid testament to the concept of erosion, however it does not explain the effects of impact angle, which causes higher erosion rate for ductile materials as impact angle is decreased. In previous erosion studies, Finnie *et al* (1967) found that the erosion rate was inversely

proportional to Vicker's Hardness measurements for a number of annealed face centred cubic metals. It was reported that these materials show similar stress-strain characteristics in terms of strain-hardening effect. In contrast, erosion rates increased for materials with low strain-hardening capacity, which is typical of materials that have been heat-treated for increased hardness. The Finnie *et al* (1967) study showed the hardness relationship to erosion is not necessarily relevant for heat-treated steel.

The *damage number* D was proposed by (Field and Hutchings, in Blazynsky 1987) to give an indication of the magnitude of inertial forces with respect to the yield strength of the impacted material, and is defined as:

$$D = \frac{\rho V^2}{\sigma_{yield}} \quad (2.3)$$

where ρ and V^2 are the density and velocity of the impacting particle and σ_{yield} is the yield strength of the wear material. The damage number provides a useful scaling factor as to the type of erosion mechanism that may occur for a certain velocity regime. Figure 2.3 shows the type of damage mechanisms possible for ductile materials such as mild steel and aluminium and for brittle materials, such as ceramics and glasses. For $D < 10^{-5}$, (less than 1ms^{-1} particle velocity) individual particle impacts cause little damage to the target material and fatigue mechanism is the main cause of erosion. In the range of $10^{-5} < D < 1$, corresponds to the regime of most industrial erosive environments, where the particle velocity can range from $5\text{-}500\text{ms}^{-1}$. In this range, ductile materials exhibit plastic flow while brittle material will fail from fracture and to a lesser extent plastic flow. For the range $D > 1$, extends through the ordinance velocity range and is applicable to ballistic impact events ($500\text{-}3\text{kms}^{-1}$, which is outside the scope of this study). At greater values of $D > 10^3$ ($> 3\text{Kms}^{-1}$) is considered to be in the hypervelocity regime. In the hypervelocity range the material properties of the target material become less influential as fluid like behavior becomes more apparent.

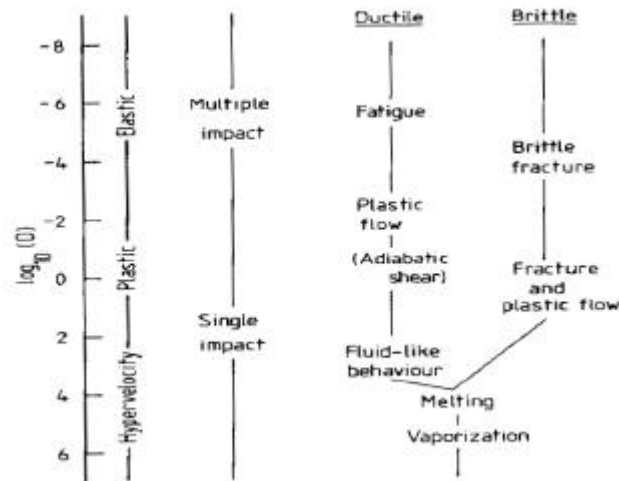


Figure 2.3 Diagram showing the change in erosion mechanism as the damage number changes. After Field and Hutchings in Blazynski 1987

Hutchings (1993) further developed the hardness approach and showed that the wear rate could be expressed in terms of the ratio of the kinetic energy of the impact particle (i.e. $rV^2/2$) to the hardness of the wear surface

$$W = \frac{k r V^2}{2H} \quad (2.4)$$

The severity of erosion is determined by the coefficient k , where k can be thought of as a measure of the efficiency of material removal by a number of particle impacts, where typical values for k lie between the ranges of 5×10^{-3} to 10^{-1} for ductile materials.

2.1.2 Erosion models for polymers

Introduction

The erosion characteristics of polymers to this date remain a relatively unexplored area of study. In the past, there has been little research carried out on the development of erosive wear models for polymers. Often, erosive wear rate is correlated with models derived from abrasive wear studies. One such abrasive wear model often quoted and showing good correlation for erosive wear of polymers, is the well-known Ratner-Lancaster model.

Ratner *et al* (1967) was one of the first researchers to examine the relationship between measurable material properties of polymers and abrasive wear resistance. The model proposed by Ratner *et al* suggests that three stages are involved in the wear process: deformation of the wear surface to an area of contact determined by the indentation hardness; relative motion opposed by the frictional force, $F = \mathbf{mNL}$ (where \mathbf{m} is the coefficient of friction and L is the sliding distance over which the force acts and N is the normal force); and deformation of the material resulting in an amount of measurable work defined by the integral of the area under the stress-strain curve. In the Ratner *et al* model, the area under the stress-strain curve (also called deformation energy capacity) was defined assuming a linear approximation of the stress-strain curve at the point of failure, where the product of the ultimate stress \mathbf{s}_u and the ultimate strain \mathbf{e}_u was used. The Ratner *et al* model for abrasive wear of polymers gives the wear rate as

$$W = \frac{\mathbf{mL}}{H\mathbf{s}_u\mathbf{e}_u} \quad (2.5)$$

Lancaster (1969) studied the wear rate of some eighteen different polymers and concluded from experimental results, that the more important parameter from the Ratner *et al* model was the deformation energy term comprising of the product of the ultimate stress and the ultimate strain. The Lancaster model assumes that the energy required to remove a unit volume of the material is inversely proportional to the bulk deformation energy capacity of the material i.e.

$$W \propto \frac{1}{\mathbf{s}_u\mathbf{e}_u} \quad (2.6)$$

For materials with high deformation energy values, it is intuitive to consider, the more deformation energy a material can absorb, the greater the resistance to critical damage in the form of plastic deformation, cutting wear or crack growth causing cumulative fatigue wear. The close relationship between the Ratner *et al* model and the Lancaster model has resulted in equation 2.6 being known as the Ratner-Lancaster model.

In another abrasive wear study by Budinski (1997), the deformation energy capacity of a wide variety of thermosetting and thermoplastic polymers was investigated. Budinski's model is based on the assumption that the hysteresis in the force deflection curve during indentation to a fixed depth is proportional to deformation energy. The procedure used by Budinski was to indent the materials with a 6mm hemispherical indenter to a prescribed depth. The force deflection curves were then analysed and deformation energy determined by the area difference between the loading and unloading curves, as shown in figure 2.4. The greater the area difference between the two curves the greater the amount of energy dissipated in the form of plastic deformation as a result of the indentation process.

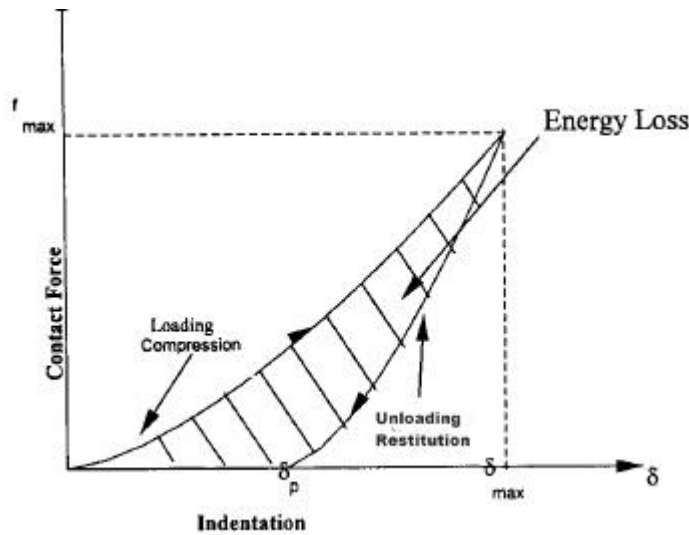


Figure 2.4 Force deflection curve produced by a spherical indenter. After Talia *et al* (1999)

In the study by Budinski, good correlation with abrasive wear rates was obtained only when the coefficient of friction m of the polymers was taken into account i.e.

$$W = \frac{1}{S_u e_u m} \quad (2.7)$$

However, by using the indentation process to measure deformation energy it does not explain the erosive wear characteristics of elastomeric materials, which of course are highly deformable and show little if any plastic deformation capacity. The force deflection curve for an elastic material would therefore show little variation from the path of the loading and un-loading curve and hence the material would show little deformation energy capacity. The theory of wear resistance being proportional to deformation energy capacity therefore does not extend to elastomers. A term more suitable for elastomeric materials would be tearing energy capacity, which could be estimated by mechanical tensile testing procedures.

In the study of elastomeric materials, erosive wear tests were conducted by Hutchings *et al* (1987), using eight unfilled elastomers, four natural rubbers, expodised natural rubber, butyl rubber, polybutadiene and polyurethane. The results of the study showed on average, that the erosion rates of the elastomers were approximately ten times higher at an angle of incidence of 30° as compared to 90°. Highly resilient natural rubber showed the lowest erosion rate. In trying to correlate erosion resistance with material mechanical properties, the glass transition temperatures, the elastic modulus at 100% strain and the ultimate tensile strength were examined, however no correlation was found. An empirical relationship was however found between the rebound resilience and the erosion rate. It was found that the erosion rate was proportional to $(1-r)^{1.4}$, where r is quoted as the fractional rebound resilience measured when a 6.3mm ball is dropped onto the rubber material from a height of 150mm. The results of the Hutchings *et al* study indicate a relationship exists between impact energy and resilience, where materials with high resilience, i.e. high elastic strain energy capacity, erode less.

Erosion studies of natural rubber by Arnold and Hutchings (1992 & 1993) and cast polyurethanes by Li and Hutchings (1990) showed the main damage mechanisms were crack propagation. The studies showed that at high impact angles, repeated elastic stretching and unloading of the surface by impacting particles caused fine fatigue cracks to develop and progressively grow into the interior of the wear surface. Where these cracks intersected, material loss (erosion) occurred. At glancing impact angles a series of ridges were formed running transverse to the erosive particle flow. Material was removed as repeated impacts caused cracks to appear at the base of the ridges and propagate into the wear surface.

Arnold and Hutchings (1993) presented a model for the erosion of rubber, for normal impact angle. The model uses data from a flat punch fatigue testing apparatus, which was designed to simulate repeated particle impacts causing fatigue cracking of the wear surface. In the punch testing method the volume V of material removed by repeated punch impacts is given by Arnold and Hutchings as

$$V = \frac{2pR}{D} \frac{dc}{dn} \quad (2.7)$$

where D is the total volume of crack surface per unit volume, R is the radius of the circular crack and dc / dn is the rate of tensile crack growth.

2.2 FEA Material Models

Introduction

Over the years, hundreds of various material models have been developed for use with FEA computational methods. An FEA material model is designed to essentially model the perceived physical deformation characteristics of the material in question. The design of an FEA material model is essentially based on *curve fitting* of experimental data and then developing material property parameters into a mathematical model to account for stress as a function of strain, strain-rate and temperature.

With so many FEA material models available, selecting the correct model can be a daunting task. Understanding the physical nature of the impact and deformation process is therefore essential for selecting a suitable material model for study by the FEA method.

2.2.1 FEA material model for AISI 1020 steel

Of the extensive range of FEA material models available, the Johnson-Cook (1983) material model is widely accepted as a suitable model for high strain-rate impact loading of mild steel. In the model shown below, the von-Mises flow stress is expressed as

$$\mathbf{s}_{vm} = [A + B\mathbf{e}_p^n][1 + C \ln \dot{\mathbf{e}}][1 - T^{*b}] \quad (2.13)$$

where the von-Mises stress is defined as:

$$\mathbf{s}_{vm} = \left[\frac{(\mathbf{s}_1 - \mathbf{s}_2)^2 + (\mathbf{s}_2 - \mathbf{s}_3)^2 + (\mathbf{s}_1 - \mathbf{s}_3)^2}{2} \right]^{\frac{1}{2}} \quad (2.14)$$

where $\mathbf{s}_{1,2,3}$ are the principal stresses. In the first bracket of the Johnson-Cook model, parameters are obtained from quasistatic tensile tests. The parameter A corresponds to the yield stress, B and n are strain-hardening terms, \mathbf{e}_p is the effective plastic strain and $\dot{\mathbf{e}}$ the plastic strain rate. In the second bracket, the parameter C is a strain-rate hardening parameter and in the last bracket thermal softening effects are accounted for by the homologous temperature T^* and the exponent b , where T^* is given as

$$T^* = \frac{T - T_{room}}{T_{melt} - T_{room}} \quad (2.15)$$

where T is calculated from the amount of plastic deformation occurring, where it is assumed that for adiabatic conditions, typical of erosive particle impacts, 90% of the work to cause plastic deformation is converted to heat, T_{melt} is the melting temperature and T_{room} is the room temperature at testing. The Johnson-Cook model is simple to apply and is well suited for FEA computational analysis as it uses applicable variables used in most FEA codes.

To understand the basic structure of the model, a Matlab program was used to obtain a stress-strain curve for mild steel. Figure 2.5 shows the stress-strain curve for AISI 1006 steel using published values of model parameters obtained from Johnson-Cook (1983). As shown the main effect of increasing the strain-rate was to increase the von-Mises stress, when the temperature was held constant. Increased temperatures would naturally tend to decrease stress values, as thermal-softening effects would cause increased plastic strain and lead to lower stress levels.

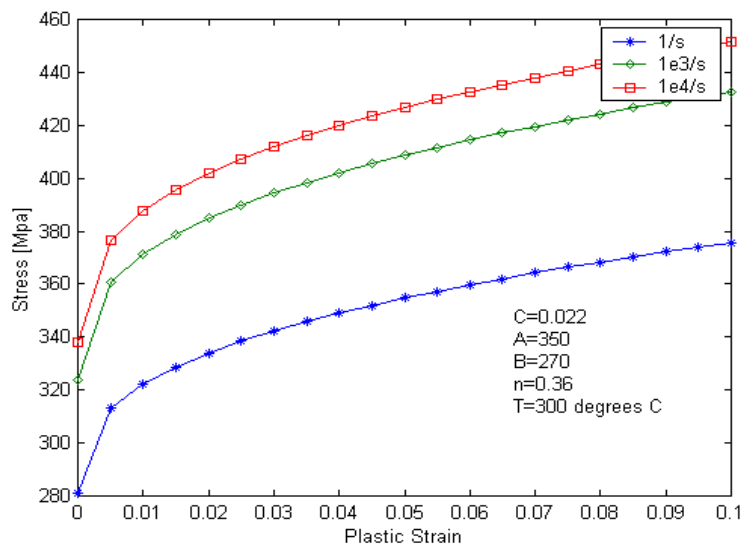


Figure 2.5 Numerical simulation of stress-strain curve for AISI 1006 steel obtained by inserting relevant model values into the Johnson-Cook model for varying strain-rates, the temperature was assumed to be 300⁰C (an arbitrary value) for the simulation

2.2.2 Review of mild steel at high strain-rates

The strain-rate sensitivity of mild steel causing increased yield and flow stress measurements is well recognised in high strain-rate studies involving Split Hopkinson's Pressure Bar (SHPB) testing. However, in the study of erosion, strain rate sensitivity of mild steel and polymeric materials has not been studied to the same extent. To gain an insight into strain-rate effects of mild steel, this section reviews a previous study conducted by SHPB method. Figure 2.6 shows quasi-static tensile tests and higher strain-rate SHPB tensile test results for mild steel at strain-rates ranging from 10⁻³s⁻¹ to

1750s⁻¹ (results from Harding in Blazynski, 1987). The main features of the stress-strain curves for the strain-rates involved are a three-fold increase in upper yield stress and a 50% increase in flow stress is observed at the highest strain-rate. Another feature of the curves at the highest strain-rate is a sharp drop in stress just after the upper yield point is reached. The absence of strain-hardening at the highest strain-rate (which is evident for quasi-static loading) suggests evidence of thermal softening.

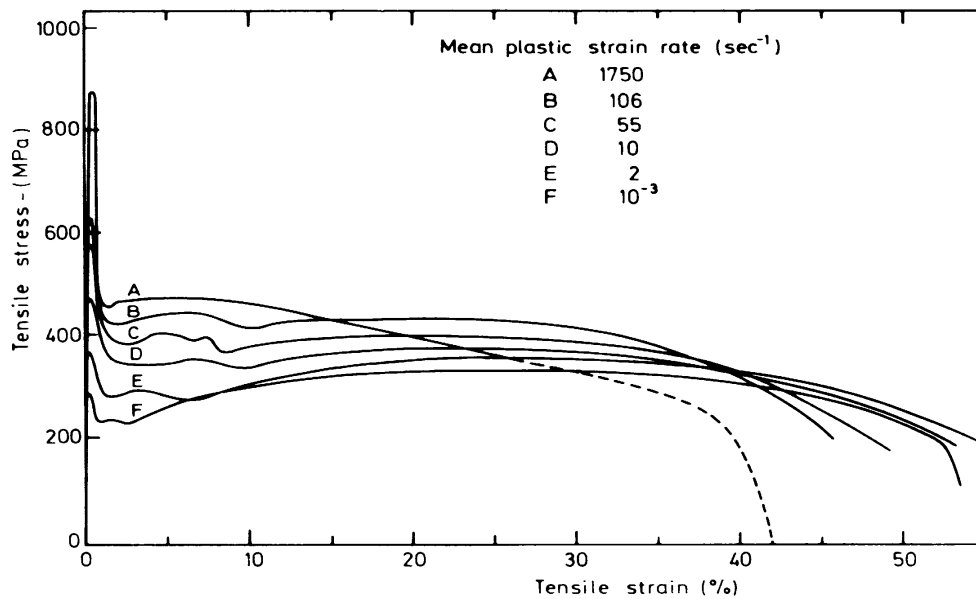


Figure 2.6 Stress strain characteristics of mild steel obtained from SPHB tensile testing. After Harding in, Blazynski, 1987

2.2.3 FEA material models for polymers

Introduction

The potential for the stress-wave monitoring process is not limited to metal materials. Polymers are now being increasingly used in erosive environments; however, little knowledge is known of the strain-rate effects of polymer wear surfaces under erosive impact conditions.

Later in this study (Chapter 5), the FEA / experimental stress wave monitoring process is extended for the study of ultra high molecular weight polyethylene (UHMWPE) and vinyl ester resin (VER) and this will require the use of a suitable FEA material model.

Under low strain-rate conditions often physical descriptors are used to describe polymers for post yield deformation characteristics. The term *glassy* usually refers to polymers, which have a highly cross-linked amorphous molecular chain structure. *Glassy* polymers usually fail by fracture soon after the yield stress is reached, as depicted in figure 2.7. Many thermosetting polymers fall into the *glassy* category and in this study VER could be classed as a *glassy* polymer.

Semi-crystalline polymers have a molecular chain structure, which is more oriented (crystalline) and repeating than amorphous polymers, and these polymers usually show more ductile deformation characteristics as shown in figure 2.7. Nylon, low and high-density polyethylene and UHMWPE (as used in this study) are typical examples of thermoplastic, semi-crystalline polymers.

Depending on the density of cross-linking, elastomers can be stiff (highly cross linked) or flexible (low cross linking). Inherently, most elastomers show non-linear elastic deformation exhibiting an upward trend of the stress-strain curve as strain increases, little if any plastic flow is observed as strain increases and tensile fracture occurs at the elastic limit as shown in figure 2.7.

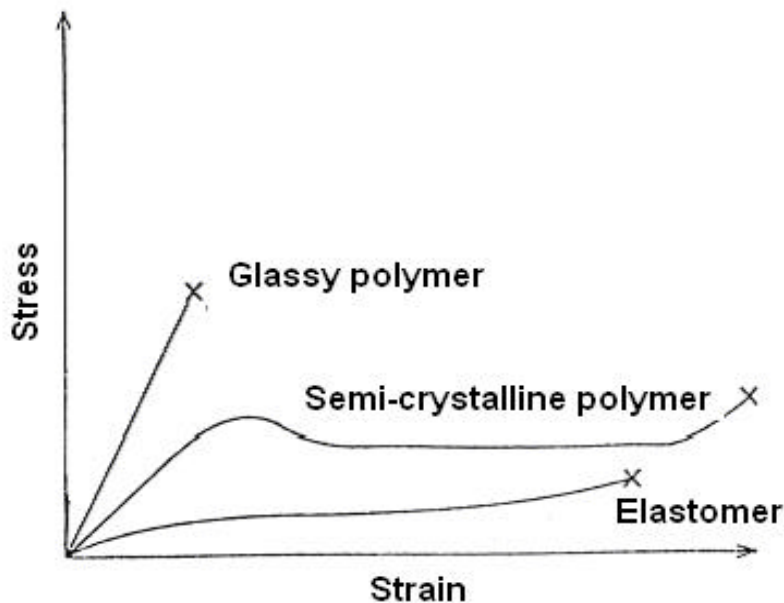


Figure 2.7 Quasistatic (low strain-rate) stress-strain characteristics of various polymers. After Stein (1998)

Under high strain-rate impact conditions, the stress-strain characteristics of polymers encompassing a wide range of molecular structure may not be as diverse as those described above. The effects of strain-rate can cause ductile to brittle transition or elastic to brittle transition.

UHMWPE on the other hand is well known for its ductile, energy absorbing nature. Most ductile polymers inherently exhibit strain-rate effects causing an increase in yield and flow stress, similar to the strain-rate effects of metals. Other factors common to metals and shared by ductile polymers, are strain-hardening and thermal-softening. Since strain-rate and thermal softening effects are similar for metals and polymers, often polymers are modelled using FEA material models designed for metals. In fact, the Johnson-Cook model described in the previous section takes into account strain-rate hardening and thermal softening characteristics. However, a literature search failed to find any evidence of the Johnson-Cook model having been previously applied to polymers.

As with metals, the study of polymers by an FEA method requires the use of a suitable yield criterion. Polymers are also sensitive to hydrostatic stress, which is due to volumetric dilatation as molecular chains are ruptured as a result of plastic flow. The simplest yield criterion for polymers takes the form (Dean and Read, 2001)

$$\mathbf{s} = \mathbf{s}_{vm} + \mathbf{h}\mathbf{s}_m \quad (2.16)$$

where \mathbf{s}_{vm} is the von-Mises stress defined by equation 2.14, \mathbf{h} is the sensitivity of the polymer to the hydrostatic stress component and \mathbf{s}_m is the hydrostatic stress defined by

$$\mathbf{s}_m = \frac{\mathbf{s}_1 + \mathbf{s}_2 + \mathbf{s}_3}{3} \quad (2.17)$$

To examine the effects of strain-rate further, the next section reviews ductile polymers subjected to high strain-rates loading conditions

2.2.4 Review of ductile polymer at high strain-rates

In figure 2.8 the stress-strain behavior of thermosetting Bisphenol A epoxy resin (BPA) is shown for strain-rates of 10^{-3} to $4.5 \times 10^3 \text{ s}^{-1}$ (Buckley *et al*, 2001). The figure shows a doubling in yield stress and flow stress at the highest strain-rate. Evidence of strain-hardening is also present as indicated by the upward trend of the stress-strain curves in the region of plastic flow. Also noted but not discussed by Buckley is an apparent increase in the slope of the initial part of the stress-strain curves (as shown by the gray lines), indicating an increase in Young's modulus may be occurring as strain-rate increases. Infrared radiometer was used in the study to show the rise in temperature during stages of compression. For the highest strain-rate considered, a modest rise in temperature to 35°C was shown in the region from post yield (at approx 10% strain) to just before fracture (approx 85% strain). At the point of fracture a sharp rise in temperature to 75°C was shown. The sudden increase in temperature indicates that much of the mechanical work to cause fracture was instantly turned into heat at the moment of fracture.

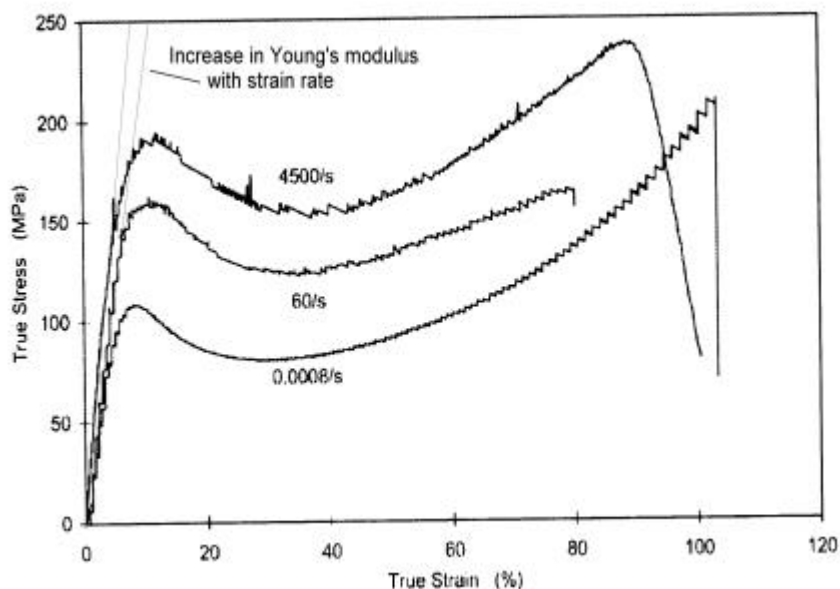


Figure 2.8 Stress strain characteristics of BPA epoxy resin, using compression SPHB testing. After Buckley 2001

In another study, the strain-rate sensitivity of propylene-ethylene copolymers was studied both experimentally and computationally (using FEA) by Dean and Read (2001). Figure 2.9 shows tensile test results for propylene-ethylene copolymer for strain-rates up to 93 s^{-1} . As shown the flow stress has nearly doubled at the highest strain-rate. Dean and Read quote the Eyring (1936) equation as a suitable expression for the increase in flow stress due to strain-rate effects

$$\sigma_f = A + C \log \dot{\epsilon}_p \quad (2.18)$$

where A is the quasistatic yield stress and C is the strain-rate constant. The form of equation 2.18 is similar to the Johnson-Cook model, with the exception of thermal softening and strain-hardening effects. The close agreement of the two models indicates that simple scalar terms may be all that is needed to describe the stress-strain characteristics of ductile polymers as a result of strain-rate effects.

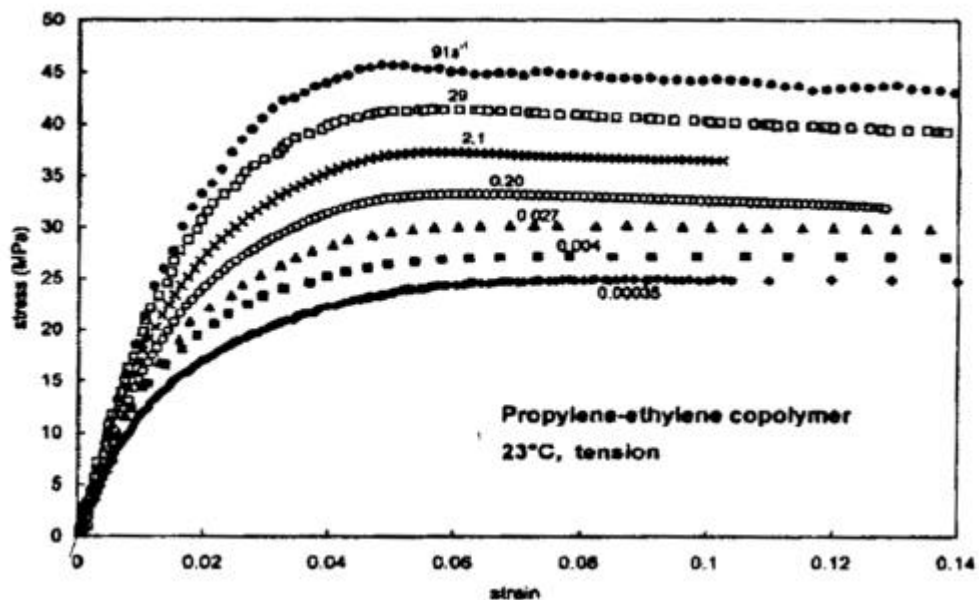


Figure 2.9 Tensile test results of propylene-ethylene copolymer. After Dean and Read (2001)

2.3 Past erosion studies involving stress-wave monitoring processes

2.3.1 Literature review of stress-waves produced by small particle impacts

Introduction

The literature review on past studies of stress-waves resulting from small particle impacts revealed very little has been carried out in this area, again emphasizing the relevance of the current study.

Ultrasonics is a method used for non-destructive testing of materials. The acoustic emission process involves placement of a piezo-electric transducer onto the test material to initiate small amplitude high frequency stress-waves into the medium. The same transducer can also be used to detect the reflected signal from the boundary (i.e. pulse echo mode) or another transducer is placed on the opposite boundary (i.e. through transmission mode) to pick up the initial stress-wave pulse. Ultrasonic methods are capable of detecting flaws in materials and determining material properties parameters such as elastic and shear modulus, Poisson's ratio and the longitudinal and shear wave velocities of isotropic materials (Krautkramer, 1969, Szilard, 1982).

Ultrasonic sensors have been used in past studies to detect stress-waves from small particle impacts. Buttle and Scruby (1990) studied stress-waves produced by low velocity impacts (up to 7m/s) to steel and bronze plates. In that study, the force time-curves were derived at the surface by using a mathematical process involving deconvolution of the wave equation. However this process is limited to elastic impacts only. For impacts causing plastic deformation of the surface, the stress-waves produced fall outside the realms of elastic wave theory. As described in the study by Buttle and Scruby, a conical ended transducer was placed at the rear of the impacted plates to record the *displacement-time* profiles of the stress-waves. Figure 2.10 shows a typical *displacement-time* profile produced by the normal impact of a 53-75 μ m bronze particle to a 6mm thick steel plate. It is not clear however, how the piezo-electric probe can measure displacement of the rear face of the wear material as displacement will only be

measured if the rear backing face of the piezo-electric element is infinitely stiff. As will be described later in this study (section 3.2.7), the voltage-time signal produced by the passage of the stress-wave through the piezo-electric sensing element needs to be interpreted into the correct mechanical terms by considering the deformation of the piezo-electric sensing element and the piezo-electric backing material.

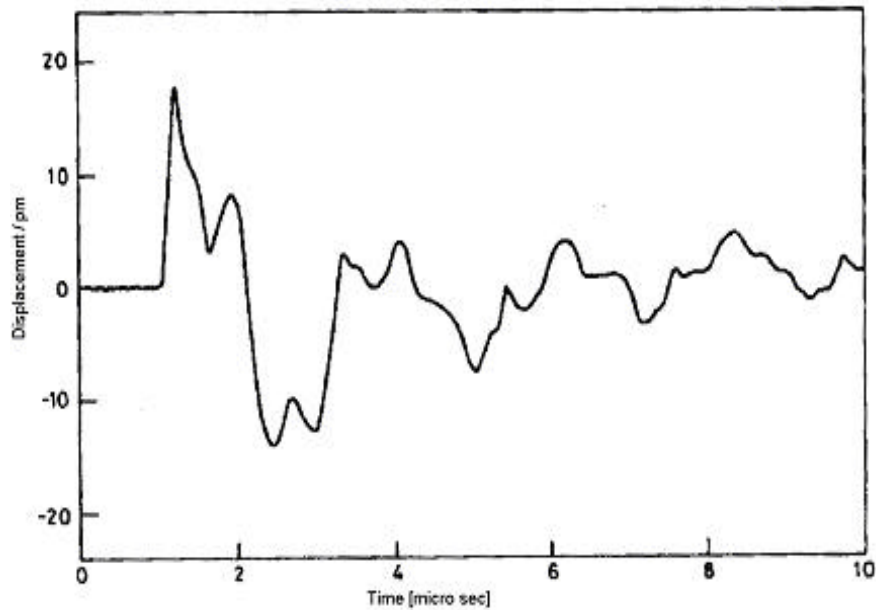


Figure 2.10 Displacement-time profile produced by 53-75µm glass particle impact to 6mm bronze specimen at 7m/s. After Buttle and Scruby (1990)

In another previous stress-wave study, Ferrer *et al* (1999) used a piezo-electric transducer placed at the rear of 3mm thick stainless steel plates to obtain voltage-time signals from single and multiple particle impacts for the study of slurry erosion. Figure 2.11 shows typical acoustic signals produced by impacts of 125µm silicon carbide particles impacting 3mm thick stainless steel plates (AISI 304 stainless steel). The figure shows considerable high frequency ‘noise’ and it is difficult to see individual stress-wave signatures. In the study, the transmitted acoustic energy AE , from the impact events was estimated by taking the integral of the stress-wave signal as defined by

$$AE = \int [A(t)]^2 dt \quad (2.19)$$

where A is the amplitudes of the stress-waves. In the study by Ferrer *et al*, it was found that a linear relationship existed between the transmitted acoustic energy and the initial kinetic energy of the impacting particle.

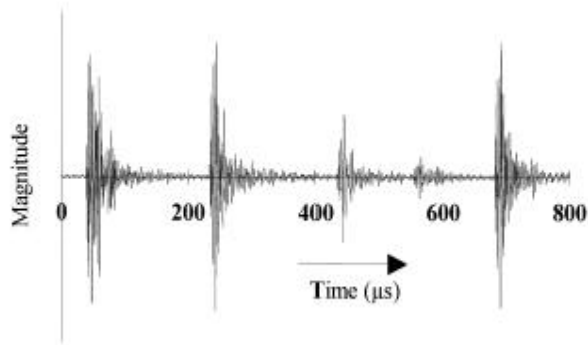


Figure 2.11 Acoustic emission bursts obtained from impacts to 3mm stainless steel by 125µm silicon carbide particles. After Ferrer *et al* (1999).

2.4 Chapter summary

This chapter reviewed three key areas relevant for the basis of the stress-wave monitoring and erosion study being developed here; erosion modelling, FEA material models of materials subjected to high strain-rate loading conditions and related stress-waves studies of small particle impact events.

The erosion model review, showed the dependence of material properties in erosion models. Finnie (1961) investigated the physical aspects of erosion by examining steel wear surfaces with the aid of a microscope. The equations of motion were solved for a single angular particle impacting the wear surface at an oblique angle, and causing a chip formation. The classic Finnie model also depicts hardness as a key term as well as impact velocity and impingement angle. The Rabinowicz (1967) hardness model is simple to apply and depicts wear rate to be inversely proportional to hardness. Hardness is a measure of resistance to penetration and this model assumes that less particle penetration will result in less wear. However, the hardness approach to erosion

resistance does not explain the erosion resistance of heat-treated steels. Finnie (1967) found that heat-treated steels eroded more quickly than ductile steels. The findings by Finnie suggested that strain-hardening was an important factor as steels with low strain-hardening capacity eroded at a higher rate than steels with high strain-hardening capacity. The Ratner-Lancaster model introduced a new term, which accounted for the work being done on the wear surface by the erosion process. This term is defined as deformation energy, which describes the *toughness* of the wear surface in resisting material removal by the erosion process.

Of the erosion models discussed, no mention however is made in regards to strain-rate hardening or thermal softening effects, which may alter the wear material physical and therefore erosion characteristics. The accuracy of an erosion model may therefore be in doubt if strain-rate and thermal softening effects are not accounted for in the model. The need for accurate measurement of material properties under erosive conditions is therefore essential for the development of an erosion model.

The next section of the review exemplified the importance of strain-rate and thermal softening effect when trying to model deformation characteristics of metals and polymers. For both ductile metals and polymers, increases in yield and flow stress was shown for these materials subjected to high strain-rate loading conditions. The Johnson-Cook material model is designed to account for strain-hardening, strain-rate as well as thermal softening effects and is well suited for implementation by the FEA method. The yield criterion for the Johnson-Cook model is the von-Mises stress, which states that plastic flow will begin when the von-Mises stress surpasses the yield stress of the material. A literature search revealed that the Johnson-Cook model is yet to be applied to polymer materials. The review of polymers at high strain-rates nonetheless did show similar trends to the strain-rate characteristics of mild steel, however the yield criterion for polymers does include the addition of a hydrostatic stress component as well as the von-Mises stress criterion.

The application of the Johnson-Cook model for the impact study of polymers such as UHMWPE and VER would present a worthwhile study considering the similarities of the strain-rate characteristics of ductile polymers and metals. The similarities allows an excellent opportunity to implement and review the Johnson-Cook model for the

computational stress-wave study of UHMWPE and VER, as will be presented later in Chapter 5.

The literature review of similar stress-wave studies involving small particle impacts revealed very little work has been carried out in this area. The stress-wave profiles produced by Buttle and Scruby (1990) did show detailed stress-wave characteristics. A deconvolution process involving the wave equation was used to obtain the force-time profile at the surface. However this process can only be used for elastic stress-wave motion and would not be relevant for studies involving elasto-plastic stress-wave motion, as the equations of motion would be non-linear. In this study, FEA will prove to be a powerful tool for the study of elasto-plastic impacts at the surface and elasto-plastic stress wave motion. The study by Ferrer *et al* (1999) showed considerable high frequency “noise” of the stress-wave profiles, which would make it difficult for a detailed stress-wave analysis to be pursued.

CHAPTER 3

EXPERIMENTAL METHODS

3.1 Introduction

In this chapter, the experimental methods are developed for the monitoring of stress-waves resulting from small particle impact events. The Chapter is broken down into three main sections. In section 1, the issues of wave dispersion and the interpretation of the effects to the recorded stress-wave are discussed. The study of wave dispersion will aid in gaining an overall understanding of how the stress-wave profile recorded at the rear face of the impacted material, can be related to impact stresses at the surface. To visualize the effects of wave dispersion, an FEA study is conducted to investigate effects of wave dispersion of the longitudinal stress-wave, for an elastic impact and an elasto-plastic impact at the surface.

One of the novel aspects of this project was the development of a piezo-electric transducer, which was specifically designed for sensing stress-waves at the rear face of impacted plates. The impact of the particle at the wear surface will cause stress-wave motion to propagate through the impacted plate, on a spherical path. The challenging aspect for the design of the transducer was to account for spatial averaging as the curved stress-wave passed through the flat sensing element. In section 2 of this Chapter, a numerical study is presented on the effects of spatial averaging to the stress-wave recording. The results of the study are used to aid in the transducer design and to locate the transducer a safe distance from the impact site so that spatial averaging effects are minimised.

In following section of this Chapter, the stress-wave monitoring and erosion apparatus are explained in detail. A novel aspect of the stress-wave monitoring apparatus was the development of a modified double disc system, purposely designed for accurate control of particle velocity and flux.

3.2 Considerations for stress-wave monitoring process

3.2.1 Stress-waves and wave dispersion

In the study of impact and stress-wave motion from small particle impacts, the effects of wave dispersion have been an underlying problem, making correct interpretation of how the stress-wave can be related to surface stresses a difficult task (Goodier *et al*, 1959). Wave dispersion occurs when different modes of vibration, of the initial stress-wave pulse travel through the bulk material at different phase velocities, where the phase velocity is defined as the velocity of the dispersed stress-wave c divided by the un-dispersed stress-wave velocity c_0 (Goldsmith, 1960).

As a result of wave dispersion, the initial stress-wave pulse is degenerated into smaller pulse trains, each arriving at the sensing location at different times. By using the principle of superposition, it is possible to obtain the initial stress-wave pulse of a dispersed stress-wave by taking the Fourier transform of the stress-wave and time shifting the pulse trains by an amount corresponding to the phase velocity difference of each frequency mode. This superposition method however, relies on two sensing locations, usually one behind the other, to determine the phase velocities of individual stress-wave pulses (see for instance, Gorham *et al*, 1996, Kaczmarek, 2001 and Zhao, 2002).

The issues of wave dispersion become more complex when plastic deformation of the surface is involved. One-dimensional stress-wave theory predicts the velocity c_P of the plastic wave travelling through a region of plastic deformation to be (Goldsmith, 1960)

$$c_P = \sqrt{\frac{E_T}{\mathbf{r}}} \quad (3.1)$$

where E_T is the local slope of the stress-strain curve in the plastic deformation zone. For materials exhibiting elastic - perfectly plastic deformation i.e. zero slope of the stress-strain curve after the yield point, equation 3.1 depicts zero wave velocity of plastic

stress-waves, hence only elastic stress-wave motion will be encountered until the yield stress is reached. The stress-strain curve of most materials however does not change from elastic to perfectly plastic suddenly. Added to this are affects of strain-hardening, which may result in at least part of the plastic component of the stress-wave pulse having a wave speed velocity somewhere near the bulk longitudinal elastic wave speed velocity of the material, which is defined as (Goldsmith, 1960)

$$c_{el} = \sqrt{\frac{E}{\mathbf{r}(1-\mathbf{n}^2)}} \quad (3.2)$$

It should be pointed out that the wave speed of the plastic wave defined by equation 3.1 is only relevant for the zone of plastic deformation close to the surface. Away from the plastic deformation zone, where the stress-levels are below the yield stress of the material, the longitudinal vibration mode of plastic stress-waves will travel through the wear material at the bulk elastic wave speed velocity, defined by equation 3.2

Of interest for the study of erosion is whether plastic deformation of the wear surface can be detected at the rear face of the impacted wear material. Being able to detect plastic deformation at the surface will be dependent on the degree of wave dispersion, and, in particular the extent of wave separation of elastic and plastic stress-waves.

To show the effects of wave dispersion for an elasto-plastic impact, a comparative study was conducted with a stress-wave initiated by a purely elastic impact †. For the study, an FEA simulation was conducted for an elastic model and elasto-plastic model of an impact by a 0.4mm zirconia sphere to AISI 1020 steel at 104m/s. In reality, the elastic impact is not possible, as the impact event will cause significant plastic deformation of the surface. Nevertheless, the comparison study will show the effects of wave-dispersion when the elastic model is compared with the elasto-plastic model. To best view the results, the elastic model has been *mirrored* and placed next to the elasto-plastic model as shown in figure 3.1a and 3.1b.

† Impact to AISI 1020 steel at 104m/s by a 0.4mm zirconia sphere. Elastic material properties detailed in Chapter 5, table 5.1, elasto-plastic material properties based on Johnson-Cook material model, detailed in table 5.2, full details of the FEA modelling geometry is available in Chapter 4.

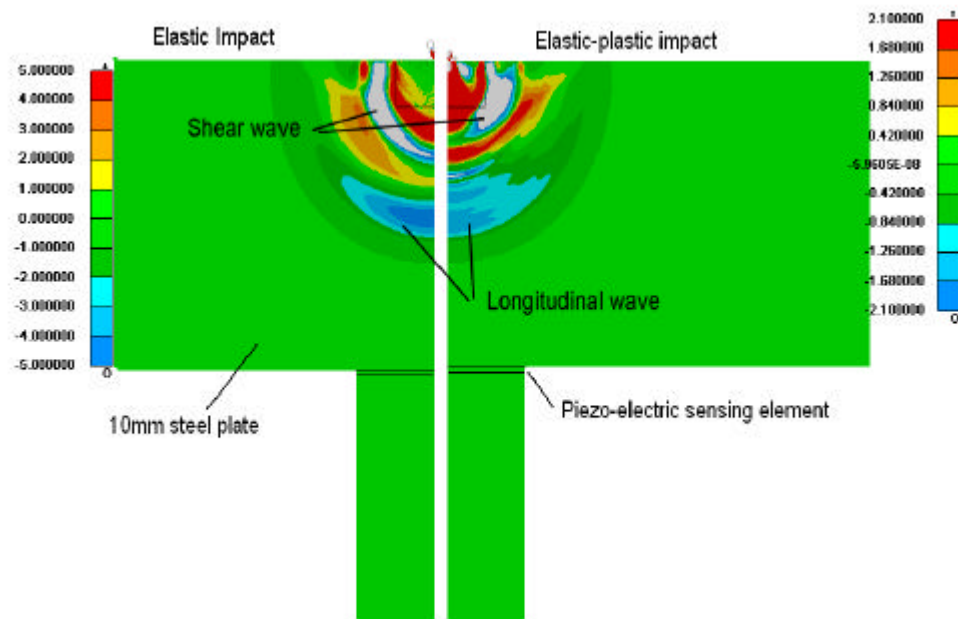
In figure 3.1a, the impact has occurred at the surface and the leading longitudinal stress-wave has traveled halfway through the 10mm steel plate. In both models, the leading longitudinal wave has separated from a trailing shear wave. The longitudinal and shear waves correspond to particular modes of vibration with each mode traveling at different velocities. The longitudinal wave causes vibration in the direction of wave propagation, whilst the shear wave causes transverse vibration across the wave front. The longitudinal stress-wave is the fastest moving wave and will arrive at the sensing location ahead of other waves. This makes the study of the longitudinal stress-wave an important consideration in this study, as the wave will not be affected by other slower moving wave activity.

When comparing the two model systems of figure 3.1a, the main differing feature is that the longitudinal stress-wave of the elasto-plastic model has broadened more than the corresponding stress-wave of the elastic model. Figure 3.1b shows the leading longitudinal stress-wave nearing the piezo-electric sensing location at 10mm from the impact site. As shown in this figure, the relative size difference of the longitudinal waves is proportionally the same as shown in figure 3.1a.

The main conclusion to be drawn from the comparison study is that the broadening of the longitudinal stress-wave of the elasto-plastic model is consistent with wave dispersion effects. As shown in both models, the longitudinal stress-wave maintained the same relative size as the wave traveled from the location of 5mm to 10mm from the impact site. The results indicates that the effects of wave dispersion may be more predominant close to the zone of plastic deformation where in this zone elastic waves are most likely to separate from plastic waves.

In drawing some conclusions from the study, it was shown, for an elasto-plastic impact at the surface, the main effects of elastic and plastic wave separation (dispersion) were shown to be a broadening of the longitudinal stress-wave. For the study of erosion, it would be beneficial to know which part of the recorded stress-time profile obtained at the piezo-electric sensor corresponded to elastic stress and which part corresponded to plastic stress at the surface. This subject will be discussed in detail in the next section.

(a)



(b)

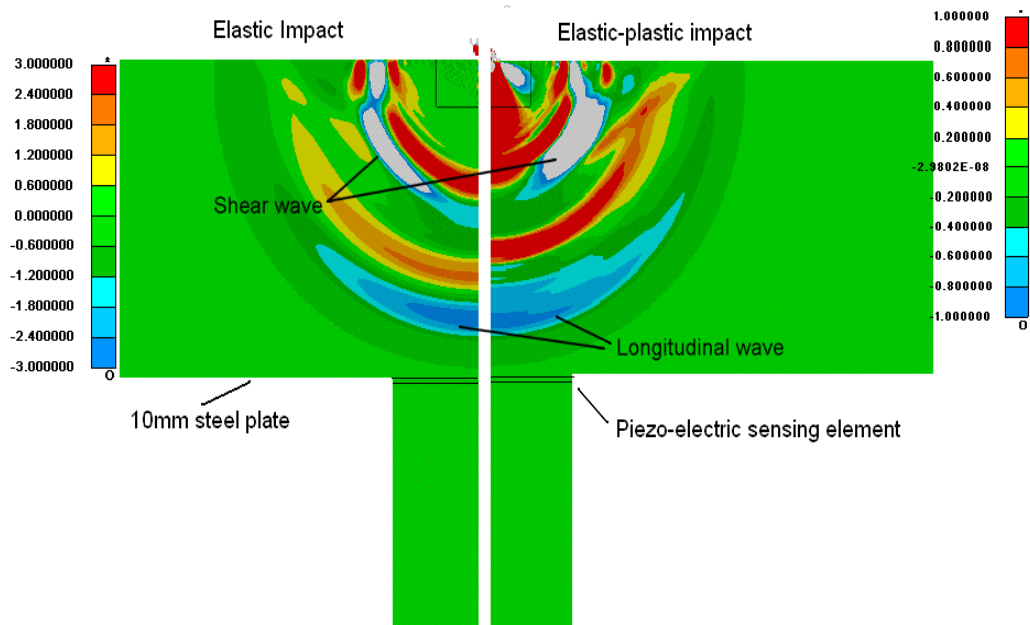


Figure 3.1 FEA simulations of stress-wave motion produced by impact of 0.4mm zirconia sphere to a 10mm thick AISI 1020 steel plate at 104m/s, colour bars indicate stress in the normal direction, negative values indicate compressive stress (a) Stress-wave at 6mm from impact site (b) Stress-wave at 9mm from impact site

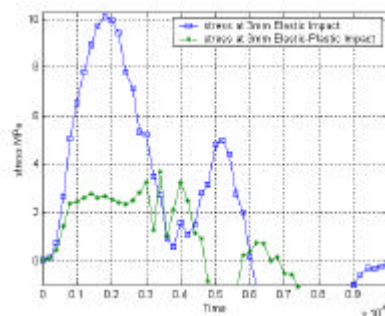
This page left intentionally blank

3.2.2 Study of stress-time profiles for an elastic and elasto-plastic impact

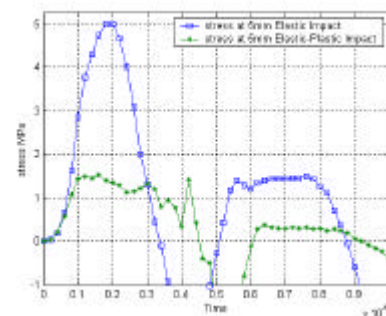
As discussed in section 2.2.1, the Johnson-Cook FEA material model contains a number of terms, which must be obtained in order to use the model for FEA simulations. Understanding key aspects of the recorded stress-wave profile in regards to elastic and plastic stress-wave motion would be beneficial for effectively reducing FEA computational time for model validation. As will be discussed in this section, this can be achieved by identifying key waveform characteristics and how they may be related to elastic or plastic material property parameters of the FEA material model.

To illustrate the processes involved, the comparative study of section 3.2.1 is continued by comparing stress-time profiles obtained at 3, 5, 7 and 10mm below the point of impact. Figures 3.2 (a), (b), (c) and (d) show the stress-time profiles arising from the elastic and elasto-plastic model [‡].

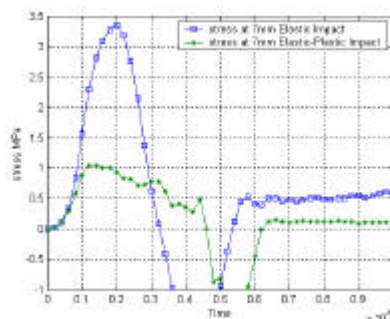
(a)



(b)



(c)



(d)

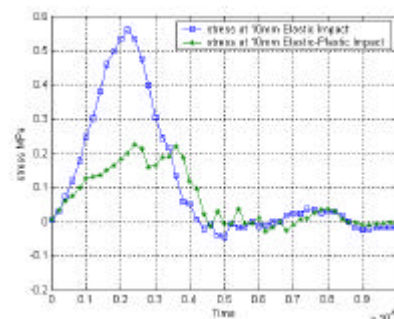


Figure 3.2 Stress-time profiles produced by elastic and elasto-plastic impact models of AISI 1020 steel surface, impact by 0.4mm zirconia sphere at 104m/s (a) stress-time profile at 3mm below impact site (b) 5mm (c) 7mm (d) 10mm

As shown in figures 3.2, the rise times of the elastic model closely matches the elasto-plastic model except at the 10mm location. The amplitude of the elastic model is approximately 3 times higher than the elasto-plastic model. No direct conclusion can be drawn from the amplitude comparison, as the elastic model would portray unrealistic stress values at the surface. The stress-time profile of the elasto-plastic model after the initial rise is shown to level off in comparison to the parabolic shape of the elastic model in each figure (3.2a, b, c and d). The abrupt change in the profile of the elasto-plastic model suggests wave dispersion may be evident. Also there is evidence of higher frequency components embedded in the latter part of the stress-wave produced by the elasto-plastic model at the 3 and 5mm locations. The higher frequency components indicate greater effects of wave-dispersion may be occurring in this part of the stress-wave profile.

As shown in figures 3.1a, b, c and d, if later parts of the stress-wave profiles of the elasto-plastic model correspond to plastic deformation of the surface then the initial part of the profiles, from time zero till the first peak, must then correspond to elastic deformation of the surface, which should in effect, scale to the yield stress at the surface. That is if the yield stress at the surface is increased then the amplitude of the initial part of the stress-time profile should also increase in a linear manner. As determined in this section, the relationship between yield stress and stress-wave amplitude will be important for validating the strain-rate parameter of the FEA material model in the stress-wave monitoring sections, 5.2 and 5.3.

The main conclusion to be drawn from the comparative study is that plastic deformation of the surface can be detected in the stress-wave profile of the elasto-plastic model. The main evidence for this was

- The plateau effect of the stress-time profile after the initial stress rise at the locations of 3, 5, and 7mm
- Shallowing of rise-time at the 10mm location
- The evidence of higher frequency components imbedded in the latter part of the stress-wave profiles
- The larger wave duration as evident by the first zero crossing

3.3 Piezo-electric transducer design

3.3.1 Considerations for the design of a piezo-electric transducer

The design and location of the piezo-electric transducer is crucial for the stress-wave monitoring process. Not only will wave dispersion occur (as described in the previous section), the stress-wave will be of spherical geometry centred on the impact point and will propagate radially outwards from the impact site. When monitoring a curved stress-wave with a flat piezo-electric transducer placed at the rear face of the impacted wear specimen, the stress-wave recording may be distorted due to spatial averaging effects as the curved stress-wave passes through the flat piezo-electric sensing element.

When considering the design of a piezo-electric transducer, it is advisable to minimise any potential effects that may corrupt the recorded stress-wave signal during the design process. The influencing factors relating to the quality of the recorded stress-wave are the curvature of the stress-wave, the wave period and the dimensions of the piezo-electric sensing element.

The wave period of the stress-wave will be related to the size and velocity of the impacting particle, the elastic modulus of the particle and the wear material and whether elastic or plastic deformation of the wear surface occurs. The choice of suitably sized particles is easily controlled. The dimensions of the piezo-electric sensing element however are not as straight forward. A small diameter and thin piezo-electric element would negate the effects of spatial averaging; however limitations come in the form of commercial availability of thin piezo-electric materials and manually machining the piezo-electric material to achieve small diameters. Because of these limitations a computational approach was needed to determine the optimum diameter of the piezo-electric sensing element and the optimum distance the sensing element needs to be from the impact site to minimise the effects of spatial averaging.

3.3.2 Matlab computer program for the design of piezo-electric transducer

A Matlab computer program was written to investigate the effects of spatial averaging and as an aid for the design of the piezo-electric transducer. For the computer simulation a stress-time profile produced by an impact to AISI 1020 steel at 104m/s was used (similar to the FEA stress-time profile as shown in figure 3.2d). This stress-time profile represents the shortest wave period of any stress-waves encountered in the study and thus provides a valuable upper limit for the transducer design.

Figure 3.4 shows a schematic diagram of the stress-wave approaching the piezo-electric sensing element which is divided into small annuli elements of volume $V_{i,j}$. Essentially, the numerical integration process was the summation of each annuli element $V_{i,j} / V_P$ (where V_P is the total volume of the piezo-electric sensing element) multiplied by the initial FEA stress-time profile $f(t)$. The time scale $t_{i,j}$ for spatial averaging calculations commenced at the time of arrival of the stress-time profile at each annular element i.e. $t_{i,j} > R_{i,j} / c_1$ or $t_{i,j} > R_{i,j} / c_2$ where $R_{i,j}$ is the radial distance of the centre of each annuli volume from the point of impact, c_1 is the bulk wave speed of AISI 1020 steel, c_2 is the bulk wave speed of the piezo-electric sensing element and V_P is the volume of the sensing element.

The spatially averaged voltage signal V_{out} after numerical integration is

$$V_{out}(t) = \sum_{i=1,n} \sum_{j=1,m} f(t)_{i,j} V_{i,j} / V_P \quad (3.4)$$

The number of rows and columns of annular elements used for the computer simulation corresponded to values of $m = 25$ and $n = 50$, respectively. There was little effect in the numerical results when a finer mesh (i.e. higher values of m and n) was used.

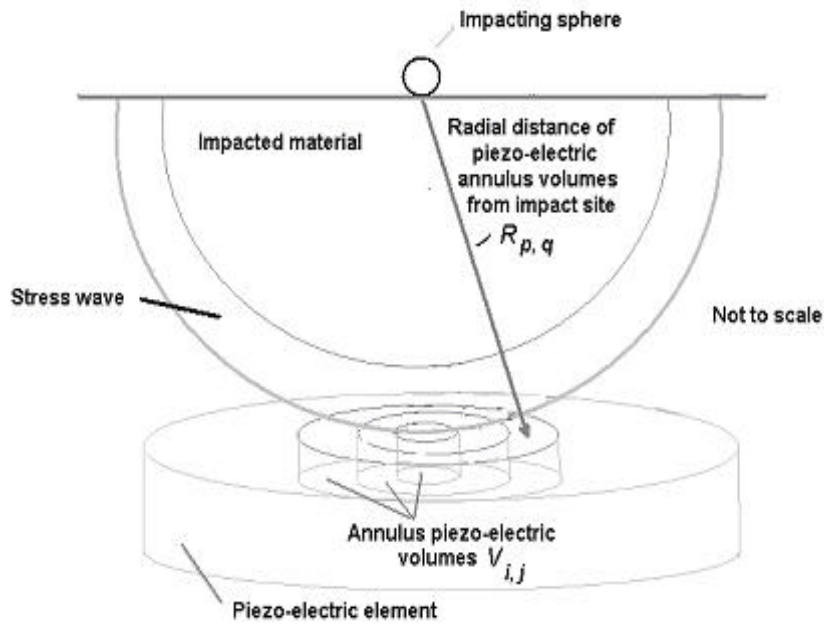


Figure 3.4 Schematic diagram of numerical integration process

The wave profile after numerical integration could be classed into two categories; the first is where the wave profile is distorted and bears no real resemblance to the initial stress-time profile, the second is where the wave profile does resemble the initial stress-time profile, however an amplitude reduction and time period increase has occurred. The first case is undesirable and shows that the parameters, which influence the stress-wave recording, namely the distance from the impact site, the pulse length and the dimensions of the piezo-electric sensing element are outside the resolution of sensing element. The latter however, allows for easy scaling of the wave amplitude and the wave time period to be carried out if required.

3.3.3 Results of Matlab simulations

A number of Matlab computer simulations were conducted to obtain a choice of impacting particles, piezo-electric sensing element diameter and the distance the sensing element needed to be from the impact site in order to minimise spatial averaging effects. Full details of the Matlab program are available in Appendix A. The simulations were based on a piezo-electric thickness of 0.2mm, which was the thinnest material available from the manufacturer. The results of the study are shown in Figures 3.5a and 3.5b.

Figure 3.5a shows negligible spatial averaging effects for the piezo-electric dimensions of 6mm diameter, located at 10mm from the impact site. The simulations were conducted for 0.4mm diameter zirconia sphere impacts. To assess the sensitivity of this result to the dimensions of the sensing element, the simulation was repeated with the diameter of the sensing element doubled (i.e.12mm). In this case, the effects of spatial averaging have become more apparent, as shown in figure 3.5b, where the main effects are lower amplitude and an increase to the period of the stress-wave.

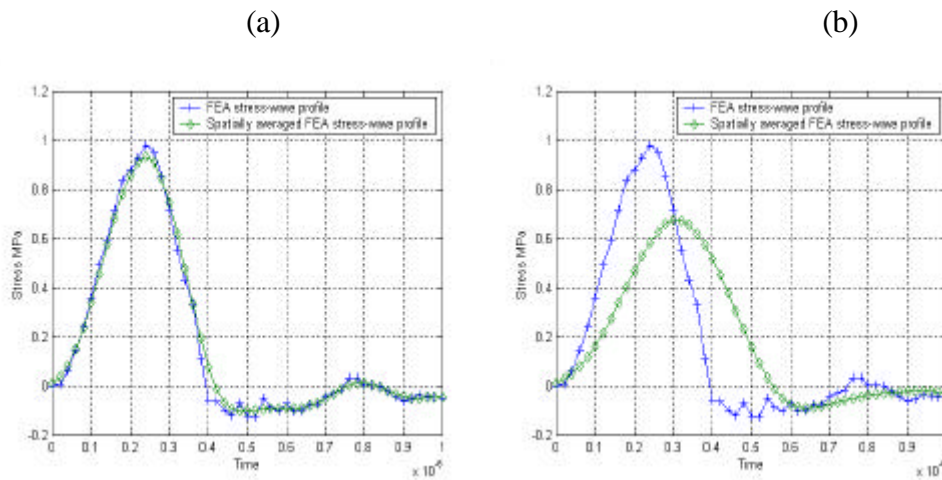


Figure 3.5 Results of numerical study into spatial averaging effects **(a)** shows the results for the diameter of the sensing element of 6mm placed 10mm from the impact site **(b)** shows the results when the diameter of the sensing element was doubled to 12mm. The impacting sphere was 0.4mm diameter and the impact velocity was 104m/s

3.3.4 Piezo-electric transducer design

Introduction

In the early stages of this project, a commercially available piezo-electric transducer was used to record the stress-wave signals. However, it soon became clear that in order to model the experimental system by FEA methods, details of the inner workings of the transducer needed to be understood. Approaches were made to the transducer manufacturer to obtain specifications, however, the manufacturer understandably would not divulge the information due to confidentiality reasons. It was therefore decided to design and build a piezo-electric transducer for the stress-wave study.

The main advantages of pursuing the task of designing and building a transducer for the stress-wave study was

- The transducer could be designed to minimize any distorting effects of the stress-wave recording i.e. to minimize effects caused by spatial averaging (as discussed in the previous sections)
- The effects caused by internal wave reflections could be minimized by the use of a long backing rod
- The specifications of all material used in the transducer were available for FEA modelling purposes
- Knowledge and understanding of piezo-electric materials is gained for transducer design, benefiting future stress-wave studies

Design of the piezo-electric transducer

Figure 3.6 shows a schematic diagram of the piezo-electric transducer. The machining process of the piezo-electric materials was essentially done by hand grinding, using an aluminium oxide tool-grinding wheel. Attempts were made to turn the piezo-electric material on a lathe, however, the material shattered very easily.

The active element, which is the sensing element for stress-wave recording, was hand machined to 6mm diameter and was available in standard thickness of 0.2mm[‡]. The active element was bonded using non-conductive adhesive to a rod machined to 6mm diameter by 12mm thick (standard thickness) of the same piezo-electric electric material[‡]. The matching of the backing rod with the active piezo-electric sensing element eliminated internal stress-wave reflections within the sensing element during the recording period. The thickness of the backing rod is also important, as the time required for stress-wave reflections from the back surface of the backing rod must be large enough so that no interference will be caused to the initial stress-wave signal being recorded.

[‡] Piezo-electric material PIC 151, supplied by P.I. Ceramics

The piezo-electric material was housed in a PVC tube with epoxy resin encasing the piezo-electric materials and wiring system. The low acoustic impedance of the epoxy and PVC tube, in comparison to the piezo-electric material, will ensure low stress-wave transmission to surrounding areas and thus ensuring stress-wave characteristics to be preserved.

The top surface of the piezo-electric active element was covered with a thin coating of colloidal silver, which completed an open-loop electric circuit with the insulated copper wire soldered on the underside of the active element. The top surface of the transducer was lightly ground down, using 2000 grit silicon carbide paper to give a true flat surface so that good contact between the piezo-electric element and the underside of the wear materials could be achieved.

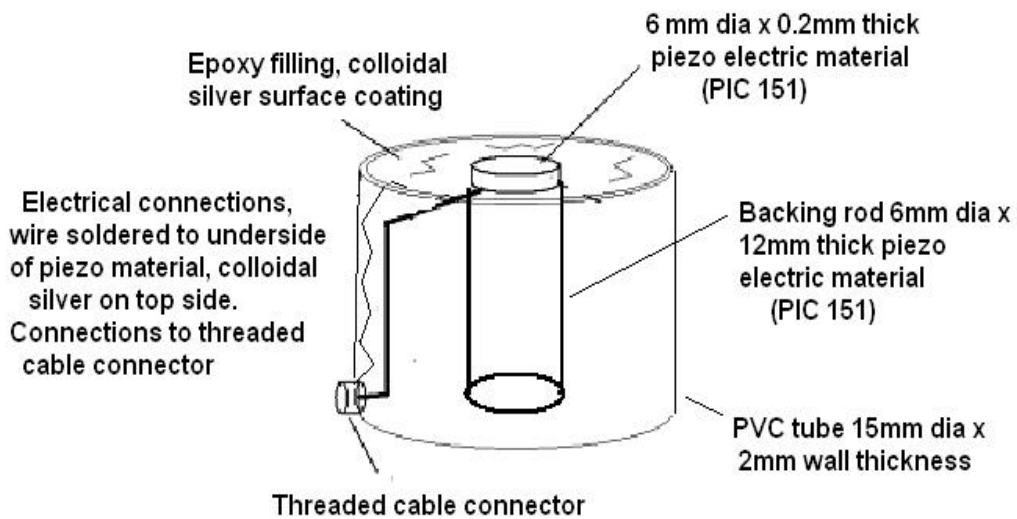


Figure 3.6 Schematic diagram of piezo-electric transducer

3.3.5 Piezo-electric materials

Introduction

In order to understand the fundamentals of the transducer operation; it is appropriate to review the basics of piezo-electric materials. Piezo-electric materials are used extensively for micro positioning applications, vibration sensing and in ultrasonic testing for the generation and detection of stress-waves. In this study, the small piezo-electric sensing element located in the transducer will be used primarily for the detection of stress-waves. In order to interpret the output voltage signal from the piezo-electric sensing element as a result of the passage of the stress-wave through the sensing element, the fundamentals of piezo-electric materials must be firstly understood.

The Piezo-electric materials

In nature, some naturally formed materials such as quartz and tourmaline are known to possess a relatively small piezo-electric effect. The piezo-electric effect can be increased dramatically over naturally formed materials by using a special manufacturing process. Today, commercially manufactured lead zirconate titanate, or PZT is the most widely used piezo-electric material. PZT is manufactured in bulk from granulated constituent materials and then sintered under heat and pressure at 1250⁰C. The ceramic block is then ground, polished and cut to the desired shape. Electrodes are then applied to each face of the material by sputter coating process so that the poling process can be carried out. Polarization is achieved by heating the ceramic to a temperature above the Curie temperature of the material and then applying an intense electric field (>2000V/mm) across the intended polarization axis. Application of the electric field causes the ceramic to expand along the polarization axis and to contract perpendicular to the axis (as shown in figure 3.7).

This page left intentionally blank

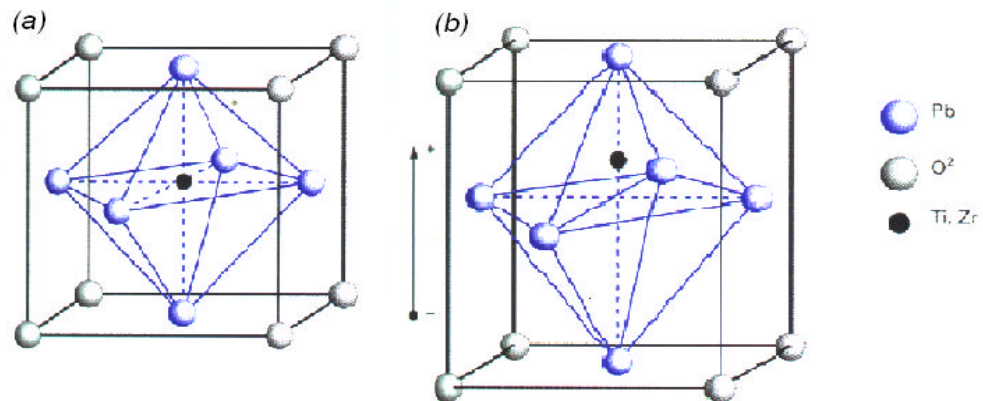


Figure 3.7 PZT unit cell shape, (a) cubic shape attained at temperatures above Curie temperature (b) rhombohedral cell structure after polarization. After PI Ceramics, 2000

Groups of unit cells with the same polarization orientation are called domains. During polarization, groups of unit cell structures (domains) align themselves to the intended polarization axis as shown in figure 3.8b. When the electric field is removed and the material cooled, the material domains are now more uniformly orientated to the intended polarization axis, as shown in figure 3.8c.

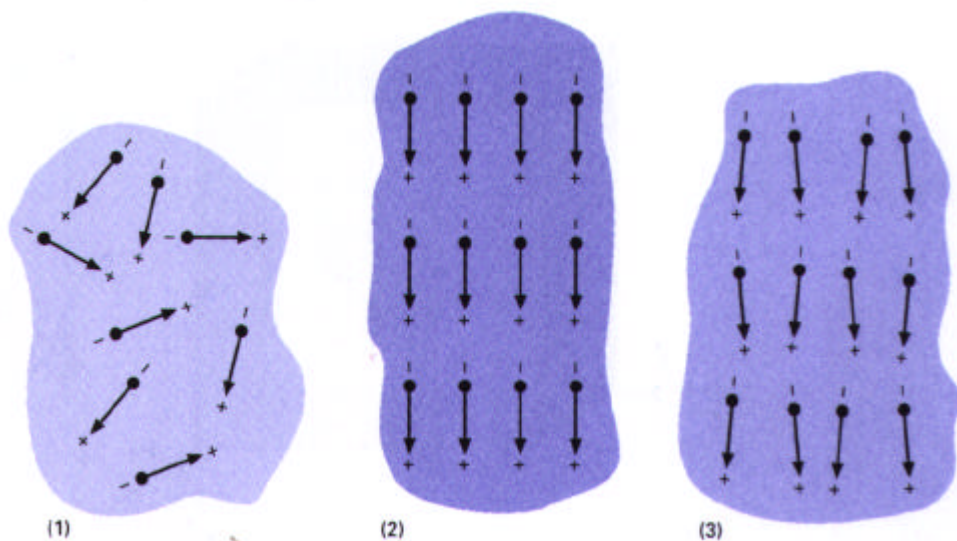


Figure 3.8 (a) Orientation of domains before polarization (b) During polarization (c) Final orientation after polarization. After PI Ceramics, 2000

This page left intentionally blank

The orientation of the polarization axis defines the axis most sensitive to charge output as a result of deformation. The coordinate system commonly used to define the polarization axis is shown in figure 3.9. In the coordinate system, X, Y and Z directions are defined as axis 1, 2 and 3 and axis 4,5 and 6 define rotations about axis X, Y and Z. To link electrical and mechanical quantities, double subscripts are used. For example the strain coefficient $d_{i,j}$ defines the strain developed per unit of electric field strength applied, where the subscripts i gives the direction of excitation and j the direction of material response. In this study, the orientation of the polarization axis was normal to the face of the piezo-electric sensing element. Therefore subscript identities i,j for the relative coefficients used are 3,3.

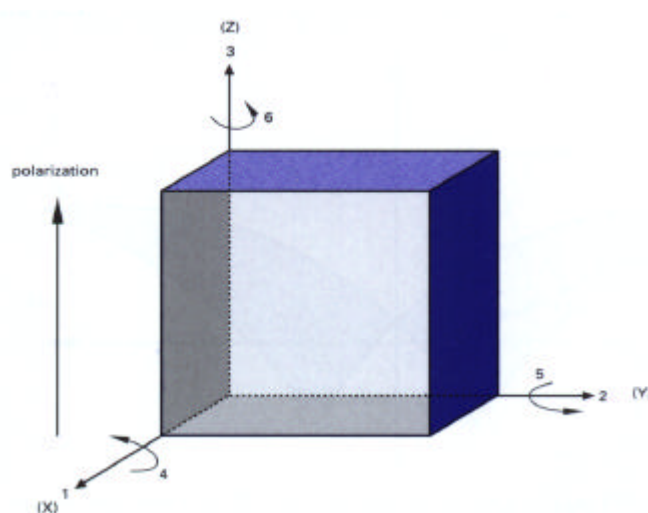


Figure 3.9 Orientation of polarization vectors for piezo-electric materials. After PI Ceramics, 2000

When an applied force deforms a piezo-electric material, a charge will appear on each face of the material. However, this charge will eventually leak back to zero through the path of least resistance. Because of the charge leakage effect, only dynamic forces can be monitored using piezo-electric materials. In this study, the timescale of the stress-wave monitoring process (micro-seconds) is much, much smaller than the timescale (seconds) for charge leakage to be considered.

This page left intentionally blank

Piezo-electric materials develop purely electrostatic charge and typically have high internal resistance, which must be matched to suitably high external resistance. For low frequency applications (kHz range and below), it is recommended that a charge amplifier be used to convert the high impedance output signal to low impedance signal so that a typical recording device such as a cathode ray oscilloscope may display the signal. However for high frequency applications (MHz range and above), charge amplifiers are generally not suitable due to high frequency filtering effects. In this case, connection directly to a high input impedance oscilloscope is preferable without loss of signal integrity (Szilard, 1982).

Piezo-electric materials are electrically modeled (in open circuit configuration) as essentially a capacitive device in series with a voltage source, as illustrated in figure 3.10 (Krautkramer, 1969).

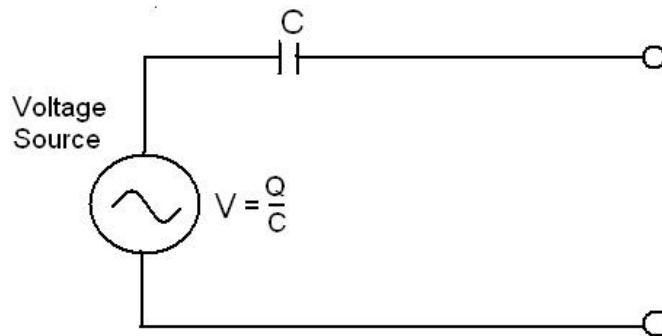


Figure 3.10 Open circuit model of piezo electric material

The piezo-electric material also has measurable internal impedance where charge can be dissipated through the material. The impedance of the piezo electric sensing element will have a real resistive component R as well as a frequency dependant component iZ , where the total impedance is the sum of the real and frequency dependant components i.e

$$X = R + iZ \quad (3.6)$$

By measuring the frequency dependant component it is possible to obtain the resonant frequency of the transducer and this will be described in the next section.

3.3.6 Natural frequency response of the piezo-electric transducer

Introduction

The natural frequency response of the piezo-electric transducer will be an important consideration for the study of stress-waves, detailed in later Chapters. Ideally, the natural frequency response of the transducer should be higher than the stress-wave frequency, to ensure natural frequency effects do not corrupt the stress-wave recording. A frequency bridge was used to measure the natural frequency of the piezo-electric transducer. For the study, a 10mm thick 1020 steel plate was firmly clamped to the face of the piezo-electric transducer, as would normally be the case in the experimental setup. This setup represents the natural frequency response of the transducer under the load applied by the clamping force and also taking into account the resonant frequency of the steel plate.

The real resistive component of the piezo-electric sensing element was measured with a multi meter and found to be 5.1M Ohms. The frequency dependant component was measured with the impedance bridge device.

Figure 3.11 shows the measured frequency dependant impedance values as a function of \log_{10} of the input voltage frequency. The maximum voltage frequency the bridge could apply was 3MHz. At this frequency it was shown that the impedance of the piezo-electric transducer was still falling. The resonant frequency of the piezo-electric sensing element will correspond to the minima of the frequency dependant impedance. As shown the minima of the frequency dependant impedance response may not have been reached, suggesting that the natural frequency of the piezo-electric sensing element was some value greater than 3MHz.

In the stress-wave monitoring section (Chapter 5) it can be shown that the maximum frequency of the stress-waves obtained from experimental impact of the wear surfaces is in the order of 1MHz (for a steel wear surface impacted at 104m/s). By operating below

the resonant frequency of the piezo-electric sensing element, the resultant stress-waves profiles should not be distorted by any natural frequency response of the sensing element.

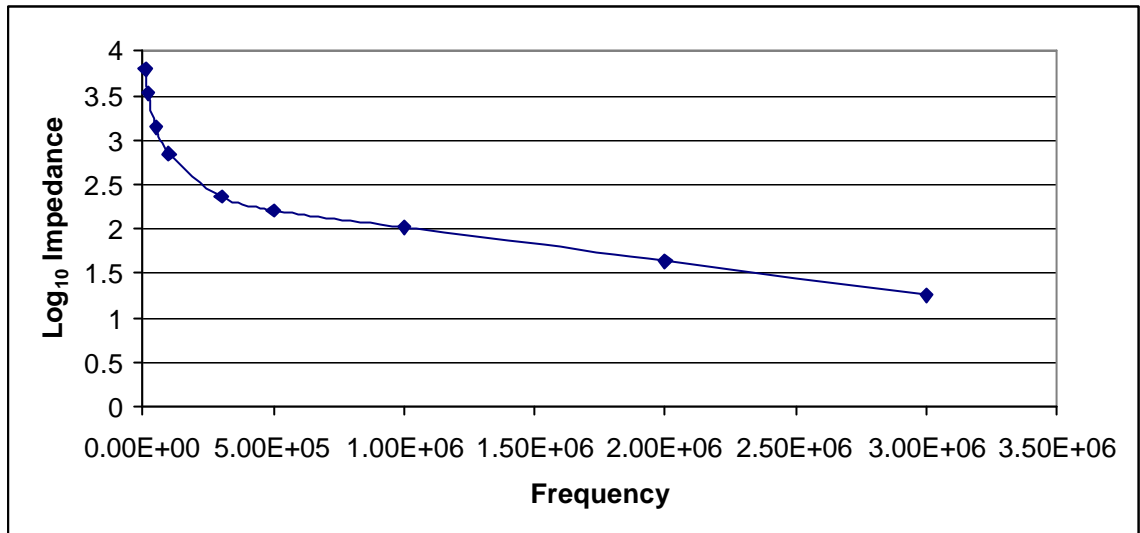


Figure 3.11 Frequency dependant impedance Vs frequency of the piezo-electric sensing element used for stress-wave monitoring

3.3.7 Electrical coupling considerations for the piezo-electric transducer

When the piezo-electric transducer is connected to the cathode ray oscilloscope, the equivalent circuit can be modeled as a simple voltage divider circuit, as shown in figure 3.12 (Krautkramer, 1969).

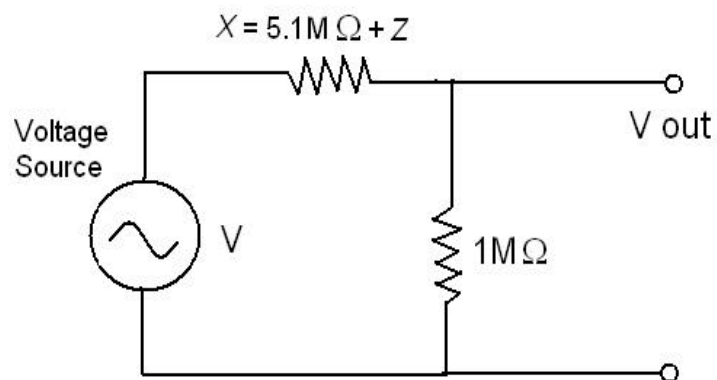


Figure 3.12 Equivalent electric circuit of piezo-electric transducer when connected to the cathode ray oscilloscope for stress-wave monitoring purposes

In the operating frequency range of 0.5 to 1MHz (the frequency range of the experimental stress-wave recordings) the frequency dependant impedance value iZ of the piezo-electric sensing element was shown to be negligibly small (100 - 160 Ω) and could therefore be neglected from electrical coupling considerations. From figure 3.12, the voltage output V_{out} can be defined by the voltage divider formula as

$$V_{out} = \frac{1M\Omega}{(5.1M\Omega + iZ) + 1M\Omega} V_s \approx \frac{1}{6.1} V_s \quad (3.7)$$

where V_s is the source voltage from the piezo-electric transducer. As shown the output voltage V_{out} will drop by a factor of 6.1 when connected to the cathode ray oscilloscope. The voltage drop essentially means the amplitude of the recorded stress-wave signal must be scaled by a factor of 6.1 in order to determine stress values directly from the piezo-electric sensing element.

3.3.8 Application of piezo-electric materials to stress-wave monitoring

The acoustic matching of the piezo-electric sensing element and the backing rod (as described in section 3.2.4) allowed the passage of the stress-wave through the piezo-electric sensing element without any wave reflections affecting the recorded signal. With this passage of the stress-wave, a voltage-time signal will be recorded by the cathode ray oscilloscope, which must then be interpreted as some measurable mechanical quantity, which can be compared with the FEA model. In this section, the interpretation of the voltage-time signal is discussed with the aid of a simple one-dimensional analysis.

Figure 3.13 shows the displacement profile of a stress-wave passing from the wear surface (axi-symmetric model) to the piezo-electric sensing element (wave reflections at the wear material / piezo-electric interface are not discussed). As described in section 3.2.5, an electrostatic charge will occur to each face of the sensing element when the

element is deformed in the direction of the polarization vector. With the passage of the stress-wave through the sensing element, the buildup of electrostatic charge at any instance in time can be shown by figure 3.13 to be proportional to the displacement of the front face d_1 less the displacement of the back face d_2 , of the piezo-electric sensing element. The zero charge reference state is the unstressed thickness of the sensing element L . When L is used to divide the change in displacement; strain will be measured directly by the sensing element.

A Voltage-time signal will be measured directly when the transducer is connected to the cathode ray oscilloscope, which in this study has an input impedance of 1M Ohms. Therefore the recorded voltage signal at any instance in time will be proportional to the strain of the sensing element, and when multiplied by the elastic modulus of the piezo-electric sensing element, stress will be measured directly i.e.

$$s = \frac{d_1 - d_2}{L} E \quad (3.8)$$

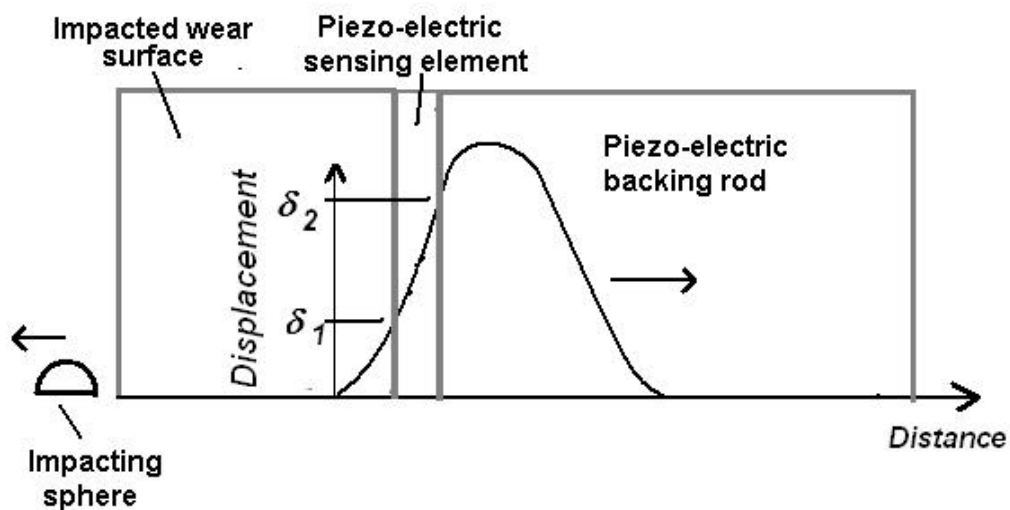


Figure 3.13 Illustration of displacement-time profile of a stress-wave passing through a piezo-electric sensing element

3.3.9 Consideration of a three-dimensional stress state at the wear material sensing element interface

The simple one-dimensional example of the stress-wave passing through the sensing element would be valid if the stress-state at the sensing element was one-dimensional. The stress-wave is however curved (2-D analogy) and therefore a multiaxial stress state will exist at the wear material / piezo-electric interface.

The stress state at the interface however can be simplified by considering the physics of the contacting surfaces as follows. Stress-wave transmission can be improved by excluding air between the two contacting surfaces and this was achieved in this study by using an oil-coupling medium. The lubrication of the contacting surfaces by the oil will in effect reduce other stress-components \mathbf{s}_x and \mathbf{s}_z , due to sliding of the interface and enhance the normal \mathbf{s}_y stress transmission across the interface. Shear-waves will travel at approximately half the wave speed of the longitudinal waves and will therefore not be encountered in the recording period of the longitudinal stress-wave. Also, the sensitivity of the piezo-electric sensing element due to the polarization process is such that the main component of stress being measured would in fact be the normal or \mathbf{s}_y stress component of the longitudinal stress-wave.

For the experimental stress-wave recordings, the voltage-time signal from the piezo-electric transducer was converted to \mathbf{s}_y stress, using the following expression

$$\mathbf{s}_y(t) = \frac{V_{out}(t)}{g_{33}L} \quad (3.9)$$

where V_{out} is the voltage time signal, L is the thickness of the piezo-electric sensing element (0.2mm) and g_{33} is the voltage to stress conversion factor for the piezo-electric material (PIC 151 supplied by PI Ceramics, see appendix C for details).

3.3.10 Recording device considerations

To record the experimental stress-waves accurately, a cathode ray oscilloscope was used with 100MHz bandwidth resolution. For the highest impact velocity considered in this study, an impact by a 0.4mm zirconia sphere at 104m/s to steel, the wave period was shown to be approximately 0.6 μ s (i.e. from the time of wave arrival to the first zero crossing of the time axis). The 100MHz oscilloscope would therefore be capable of obtaining approximately 60 data points for the highest impact velocity, stress-wave profile. With such a high number of data points, the stress-time profile of the stress-waves should be well defined by the oscilloscope recording.

3.3.11 Rise-time consideration of piezo-electric transducer response

Introduction

Fast response to an applied stress field is a characteristic feature of the piezo-electric materials. The rise-time could be described as the time required for the piezo-electric material to strain from a value of zero strain to maximum strain under the action of a suddenly applied stress (i.e. step stress input). In order to monitor the stress-wave successfully, the rise time should be considerably smaller than the wave period in order to avoid unwanted phase lag, which may distort the stress-wave recording.

Rise-time calculations

In this section, the rise-time response of the transducer is considered. The rise time of the voltage signal to a suddenly applied stress is approximately 1/3 the resonant frequency of the piezo-electric active element. The resonant frequency f_0 of the piezo-electric sensing element (which was shown to be greater than 3MHz in section 3.2.6) was calculated as (see Krautkramer, 1969)

$$f_0 = \frac{c_{el}}{2d} \quad (3.10)$$

Using equation 3.10, the resonant frequency of the piezo-electric transducer was found to be approximately 6.75 MHz (based on the piezo-electric material longitudinal wave speed $c_{el} = 2700\text{m/s}$ and piezo-electric thickness of 0.2mm). This gave a rise-time value of approximately

$$t_{\min} \approx \frac{1}{3f_0} \approx 4.9 \times 10^{-8} \text{ sec} \quad (3.11)$$

The rise-time value is approximately 12.25 times faster than the period of the experimental stress-wave recording obtained in this study, with the smallest wave period being for AISI 1020 steel at 6×10^{-7} seconds. The rise-time or response lag to an applied stress field means that the entire stress-wave curve will be shifted in time by a small amount (i.e. 4.9×10^{-8} sec), which should not affect the stress-wave recording.

3.4 Apparatus

3.4.1 Stress-wave monitoring apparatus

The stress wave monitoring experiments were carried out with a gas blast erosion rig, which was originally designed for erosion testing to ASTM standard G76-95. For the stress-wave monitoring experiments, a novel method was used to control the velocity of particles striking the wear surface (Allen *et al*, 2002). Usual methods of calibrating the velocity of the impacting particles involve the use of a laser velocity device or a double disc system (see Ruff *et al*, 1975 for designs of double disc system), which are primarily used prior to testing and then removed for erosion testing. However, by removing the velocity-measuring device prior to erosion testing, the velocity of the impacting particles cannot be assured as subtle changes in experimental conditions can vary particle velocity. Added to this effect is the problem associated with plume divergence, where particles exiting the acceleration nozzle can show considerable velocity differences across a divergent plume.

To control particle velocity, a specially modified double disc system was continually operated during the impact and stress-wave monitoring experiments. The main modification to the double disc system was the addition of a small diameter hole (1.5mm diameter) placed in the second disc. The small diameter hole allowed only particles with the intended velocity to strike the wear surface.

Figure 3.14 shows a schematic diagram and figure 3.15 shows a picture of the stress-wave monitoring apparatus. The double disc system is shown mounted on a 8mm diameter stainless steel shaft, which had two small electric motors attached at each end. Shaft rotational speed was controlled using a segmented 60mm diameter by 3mm thick aluminum disc mounted on the shaft. The aluminium disc (pictured in figure 3.16) had ten slots of 1.5mm wide cut into the periphery of the disc. A light sensitive diode was used to detect a beam of light shone through the slotted disc as they rotated with the resultant voltage impulses counted by a frequency counter. In this way, the rotation of the shaft could be monitored accurately.

This page left intentionally blank

A variable voltage DC power supply was used to control the voltage hence rotation speed of the electric motors mounted to the double disc shaft. For most experiments the double discs rotated at 95 revs per second. Two focus plates were also used to limit the flow of particles to those entrained in the center of the gas stream as shown in figure 3.14. The effects of the double discs and focus plates was to control the velocity of the particles to a fine degree and to limit the flux of particles so that stress-wave monitoring could be carried out on individual particle impacts.

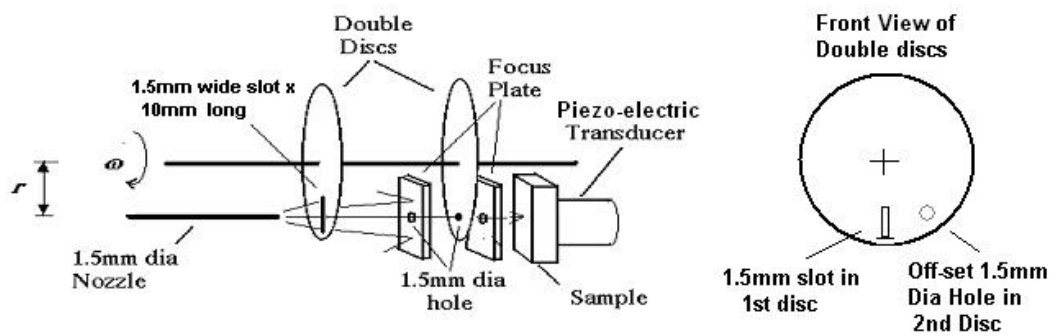


Figure 3.14 Schematic diagram of stress wave monitoring apparatus. After Allen *et al*, 2002



Figure 3.15 Stress-wave-monitoring apparatus

This page left intentionally blank

This page left intentionally blank

3.4.2 Particle velocity calculations

The velocity of the impacting particles was calculated as follows: By knowing the offset angular distance S of the hole in the second disc, from the slot in the first disc and the angular velocity of the double disc system, the velocity V of the particles travelling through the hole in the second disc can be calculated by

$$V = \frac{r \omega D}{S} \quad (3.12)$$

where D is the distance between the double discs (20mm), r is the distance of the particle acceleration nozzle to the centre of the double disc shaft (46.5mm) and ω is the angular velocity of the double disc.

3.4.3 Clamping of the wear material to the piezo-electric transducer

Clamping of the wear specimen to the piezo-electric transducer was achieved with four stainless steel hold down lugs, which were screwed to the wear specimen housing as shown in figure 3.18. The stainless steel lugs provided firm downward spring force to the wear material; ensuring good contact was made between the rear of the wear material and the face of the piezo-electric sensing element. The wear material housing was mounted on a rotating arm so that the angle of impact could be varied if required.

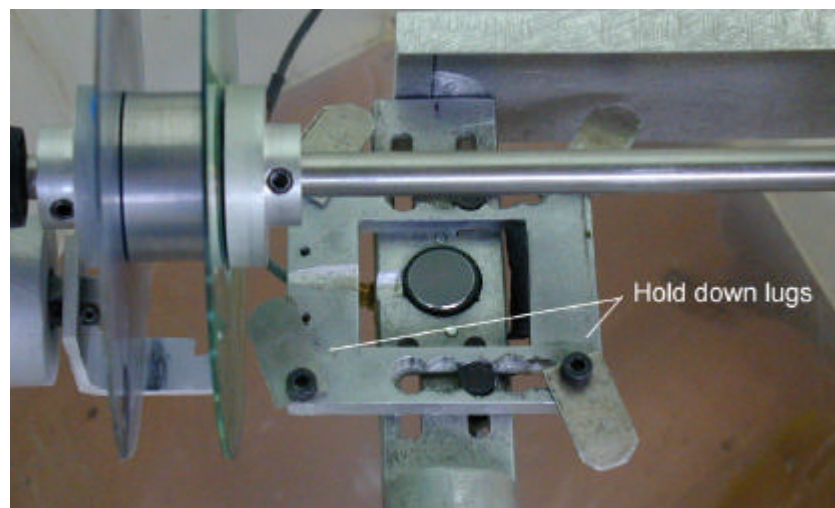


Figure 3.18 Double disc system and wear specimen-clamping device

This page left intentionally blank

3.4.4 Stress-wave monitoring chamber and gas-blast apparatus

The system pictured in figure 3.19 shows the *Swam-Blaster* ‡ abrasive blasting apparatus (left) and the perspex erosion / stress-wave monitoring chamber (right). The Swam-blaster apparatus is essentially designed for the mixing of the abrasive particles under air-pressure. The impacting particles are contained in a pressurized stainless steel housing, with vibration-gravity feed method used for particle / air mixing. Abrasive particle mass flow and air pressure was controlled with the relative dials located on the *Swam-Blaster* apparatus. The particles entered the perspex erosion chamber under air pressure by a plastic tube and exited a tungsten carbide acceleration nozzle. The acceleration nozzle was 1.2mm inner diameter and 50mm long. The perspex erosion chamber housed the rotating double disc system, the piezo-electric transducer and wear material.



Figure 3.19 Swam-blaster abrasive blasting apparatus (left) and erosion chamber (right)

‡ Swam-blaster apparatus supplied by Crystal Mark, USA

This page left intentionally blank

3.4.5 Particle characterisation

The impacting spheres used for the stress-wave monitoring study were ceramic spheres, based on a material structure of 66% zirconia and 33% silica glass. The ceramic spheres are specifically designed for abrasive blasting and shot peening applications and are sold under the trade name of Zirblast spheres[‡]. Typical material properties of the ceramic beads are shown in table 3.1 (and detailed in Appendix C)

Table 3.1 Material properties of zirconia ceramic spheres used for impact and stress-wave study

Specific gravity	3.85 g/cm ³
Young modulus	133 MPa
Bulk density	2.3 kg/l
Vickers hardness	700 HV
Equivalent Rockwell HRC	60
Poisson coefficient	0.27

The spheres as shown in the microscope image of figure 3.20, were sieved by hand to particle sizes between 355-500 μ m. The particle size distribution, based on 100 measurements of the spheres is shown in figure 3.21. As shown, the highest percentage of the spheres was 0.4mm diameter and this size was subsequently used for the FEA model.

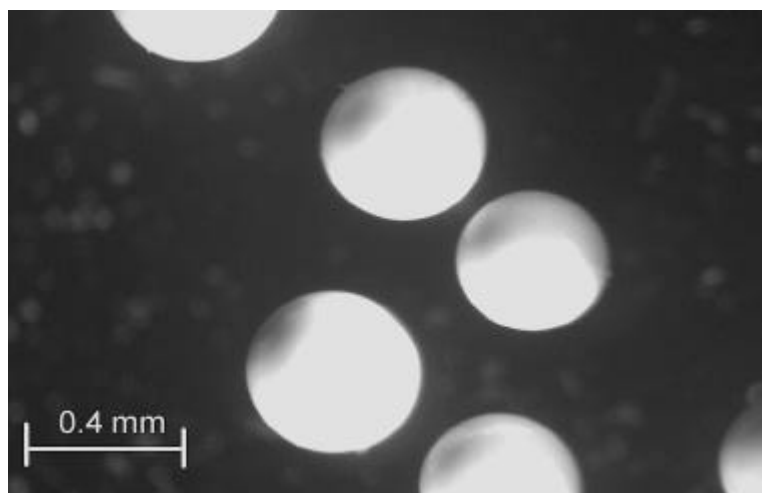


Figure 3.20 Microscope image of 0.4mm *Zirblast* zirconia spheres used for impact and stress-wave monitoring experiments

[‡] Zirblast ceramics beads supplied by SEPR, Queensland

This page left intentionally blank

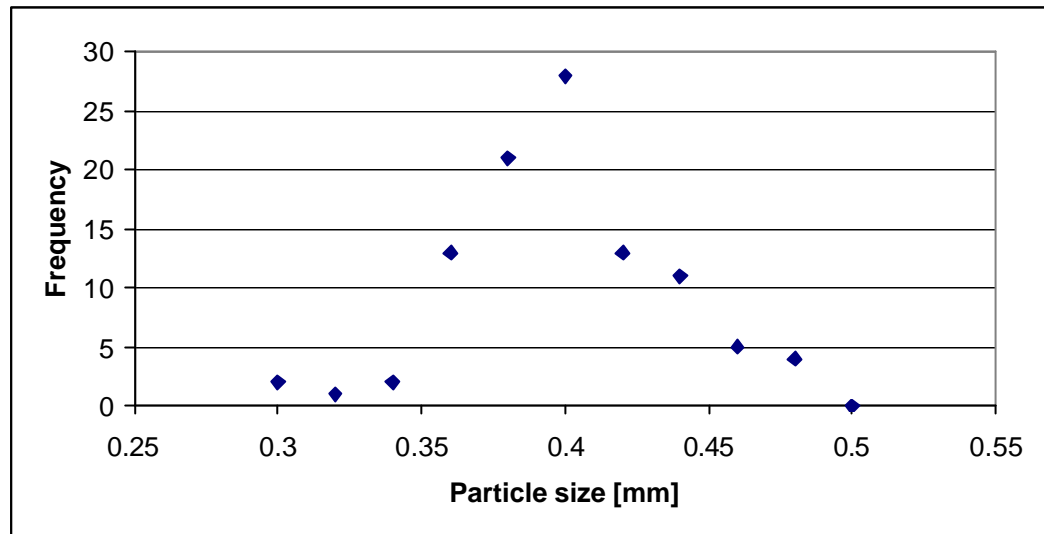


Figure 3.21 Particle size distribution of 100 zirconia spheres used for the impact experiment

3.4.6 Erosion testing

The stress-wave monitoring study using spherical particle impacts is essentially designed to obtain material property parameters at strain-rates typical of erosive impact events. The impact of a sphere at normal incidence may cause some degree of erosion, however sphere impacts are not generally encountered in most industrial environments. Angular particle and oblique angled impacts are more common. In Chapter 6, results from erosion tests are used to develop an erosion model with material property data obtained from the stress-wave monitoring study of Chapter 5.

To obtain erosion rates of each material, erosion tests were conducted using aluminium oxide as the abrasive and particle impact trajectory of 45-degrees to the particle flow. The erosion test procedure represents a hostile erosion environment and will cause ploughing and cutting erosion mechanisms of the ductile steel and polymer wear surfaces.

This page left intentionally blank

Erosion testing was conducted using the stress-wave monitoring apparatus, which was modified by removing the double disc system prior to erosion testing. Figure 3.22 shows a schematic diagram of the erosion test procedure. As shown, a 1.2mm diameter tungsten tube nozzle (50mm long) was used for particle acceleration and the wear specimen was inclined to 45-degrees relative to the particle flow. In these erosion tests at oblique incidence, effects of plume divergence were minimized with the placement of two steel focus plates (5mm apart), placed directly in front of the nozzle and at a distance of 5mm from the nozzle. The intention of the focus plates was two fold; firstly plume divergence can result in velocity variations across the plume where highest particle velocities are located at the center of the plume and slower particle velocities occur moving progressively out towards the edge of the plume. Secondly plume divergence also causes variations in the intended impact angle. With the addition of the focus plate, only abrasive particles with a very narrow velocity range would strike the surface and at the correct impact angle, thus increasing the accuracy of the erosion testing procedure as compared with conventional erosion testing techniques.

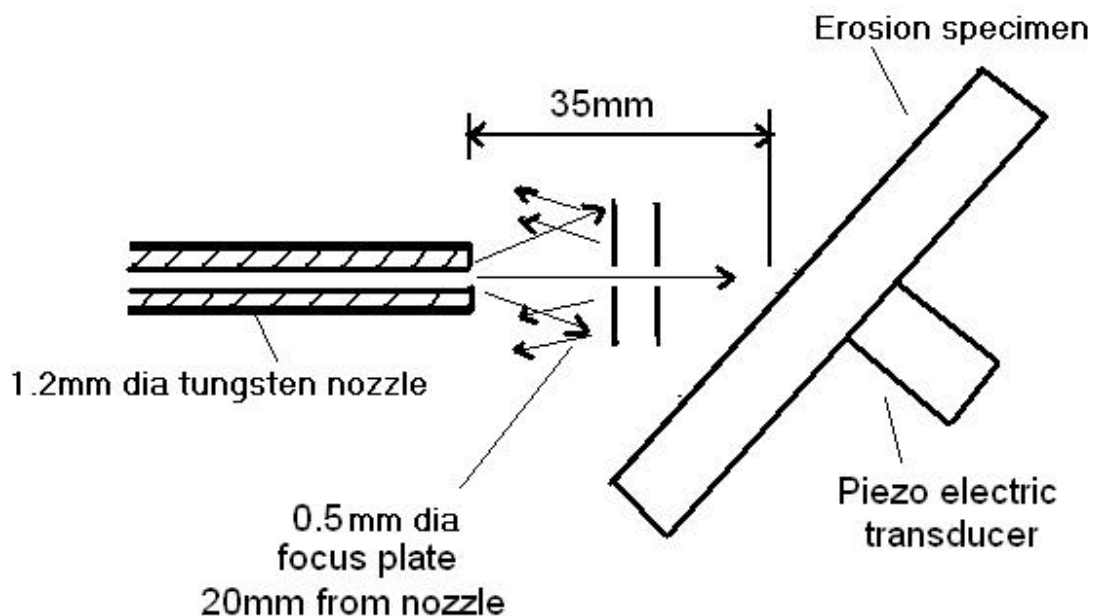


Figure 3.22 Schematic diagram of erosion testing apparatus

This page left intentionally blank

Particle velocity was measured with the double disc system prior to erosion tests and then removed for erosion tests. During erosion testing, the number of particles striking the wear surface was counted by monitoring the stress-waves produced by individual particle impacts. In the experiments, a frequency counter was used to count the stress-wave pulses received by the piezo-electric transducer, placed at the rear of the wear specimens. The particle mass flow rate was set at approximately 1mg/min, which equated to approximately 40,000 impacts for one hour of erosion testing. It was found that recognizable erosion for the materials considered in this study occurred after 20,000 impacts.

Aluminium oxide particles sieved to 90-125 μ m particle sizes were used for the erosion experiments. The morphology of the particles could be described as highly angular as shown in the microscope image of figure 3.23. As described in Chapter 1, particle angularity plays an important role in erosion, as the erosion rate will increase as particle angularity increases. On a scale from spherical to angular particles, spherical particles would cause lowest erosion rates, followed by semi-angular (i.e. sand or dust particles), causing moderate erosion, then highly angular particles such as aluminium oxide causing highest erosion rates.

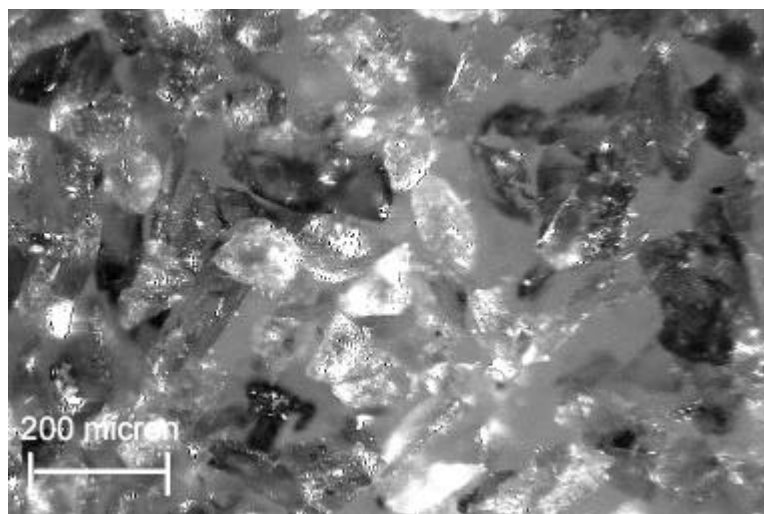


Figure 3.23 Microscope image of 90-125 μ m aluminium oxide particles used for erosion testing

This page left intentionally blank

3.4.7 Mass loss measurements

In earlier preceding erosion experiments, mass loss for erosion rate calculations was obtained by weighing the specimens before and after erosion testing using a balance with gram measurement accuracy of 10^{-4} . However, it was shown that the balance was very susceptible to environmental disturbances and weight measurements could also be compromised by specimen contamination by moisture or embedded particles from erosion testing.

As a result of the weighing difficulties, a profilometer was subsequently used to measure specimen volume loss by performing a series of traverses across the erosion scar, to eventually build a 3-dimensional map of the eroded surface. The procedure used was to clamp the wear specimen to a compound microscope table and position the profilometer near the erosion crater. A series of traverses was then performed using the profilometer with the compound table moved incrementally inwards by 0.15mm between each profilometer traverse. Figure 3.24 shows the Mitutoyo profilometer and the compound table. A series of approximately 10 to 12, 2-dimensional depth profiles was obtained by this method. A Matlab computer program (detailed in Appendix A) was then used to develop a three-dimensional map of the eroded surface and to calculate the volume of material lost from each specimen. Figure 3.25 shows a typical surface profile of the 1020 steel wear surface after erosion testing at the impact velocity of 150m/s.



Figure 3.24 Compound table and Mitutoyo profilometer used to develop 3-dimensional maps of erosion surface

This page left intentionally blank

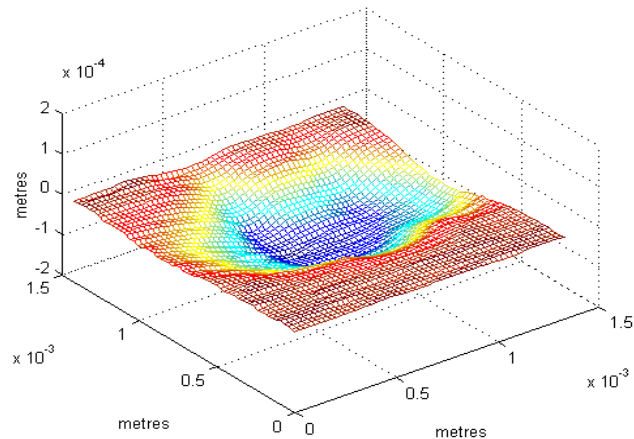


Figure 3.26 Profile of AISI 1020 steel wear surface. Erosion tests carried out at 45-degrees to particle flow, impacting particles were 90-125 μ m aluminium oxide at the impact velocity of 150m/s

3.5 Chapter summary

This Chapter covered many challenging issues associated with the monitoring of stress-waves produced by small particle impacts. In the first section of this Chapter, the issues of wave dispersion for an elastic impact and an impact causing substantial elasto-plastic deformation of the surface were discussed. It was shown that the main effects of wave dispersion for an elasto-plastic impact was the broadening of the stress-wave period, a stress plateau was reached after the maximum stress amplitude and high frequency components were encountered in the latter section of the stress-wave profile. It was concluded that wave dispersion causing elastic and plastic waves to separate occurred in the zone of plastic deformation close to the wear surface. It was concluded that as a result of wave dispersion, the amplitude of the stress-wave should scale with the yield stress at the surface. The findings will be essential for validating parameters of the Johnson-Cook model relevant for yield stress calculations of the wear material.

In the following section, the piezo-electric transducer design was discussed. The main issue concerning the design was the effects caused by spatial averaging due to the passage of a curved stress-wave through the flat piezo-electric sensing element. The effects of spatial averaging can be minimized by careful consideration of the parameters, which will influence the stress-wave recording namely; the wave period, the

distance the piezo-electric sensing element needs to be from the impact site and the dimensions of the sensing element. To aid in the analysis, a numerical study was conducted. The numerical study was very useful for choosing the size of the impacting particles, the wear material plate thickness and obtaining dimensions for the piezo-electric sensing element.

In the following section of this Chapter, it was shown that the natural frequency of the transducer was sufficiently high enough to be used without distortion occurring to the recordings of experimental stress-wave. In the following section, an electrical model of the piezo-electric transducer was developed. It was shown that when the transducer was connected to the cathode ray oscilloscope, a voltage amplitude reduction of approximately 6.1 would occur to the stress-wave signals.

In the last section of this Chapter, the stress-wave monitoring and erosion apparatus were described in detail. The apparatus consisted of a novel double disc system to accurately control particle velocity throughout the duration of the stress-wave monitoring experiments.

CHAPTER 4

FEA MODELLING OF STRESS-WAVES

4.1 Introduction

In this Chapter, the FEA modelling technique is developed for the study of normal impacts to the wear surface and resultant stress-wave motion. In section 1, a general introduction is presented on FEA analysis by *implicit* and *explicit* methods. The next section of Chapter 4 discusses how the FEA model can be simplified by using axisymmetric modelling techniques.

The following section of this Chapter discusses some of the challenging aspects of developing the FEA model for the study of small particle impacts and stress-wave motion. In particular, one challenging aspect is the small size of the impacting particle (0.4mm) relative to the size of the impacted plate (10mm thick). The size disparity places considerable demands on developing the FEA mesh to firstly account for the deformation zone, which must have a fine mesh to correctly model surface deformation and secondly to model stress-wave motion through the bulk material. Correct modelling of surface deformation, which is the primary driver of stress-wave motion, will be an extremely important aspect of the FEA stress-wave study. In order to achieve the correct mesh size, elastic theory was used to verify FEA results for surface deformation.

In the following section of this Chapter, the issues relating to numerical instability of the FEA model are discussed. In this study, it was found that the effects of numerical instability became a major issue of concern when trying to model stress-wave motion by the FEA method. Numerical instability was evident in the form of high frequency *noise* and the apparent corruption of the stress-wave profile when certain material property and contact model algorithms were used in the FEA model.

To model impact problems by the FEA method, a contact algorithm needs to be applied to the FEA model. The LS DYNA FEA program (as used in this study) has available many contact algorithms to model a variety of contact situations. A contact algorithm was required to model the impact of the sphere with the wear surface and the contact of the wear material and the piezo-electric transducer. The latter contact algorithm was required, as it cannot be assumed that the wear material and the piezo-electric sensing element are a continuum. If a continuum model were assumed, then one-dimensional stress-wave theory would apply for stress-wave transmission across the contact interface (see for instance Goldsmith, 1960). In the experimental system, an oil-coupling medium was used between the wear material and the piezo-electric transducer to enhance stress-wave transmission across the contact interface. As a result, the oil-coupling medium may alter the stress-wave characteristics as the wave passes through the contact interface. In this section of Chapter 4, the issues surrounding the modelling of the contact interface by the FEA method are discussed.

In order to compare the FEA stress-wave profiles with experimental results, the FEA stress-wave recordings must undergo the same spatial averaging transformation as would occur in the experimental recording process[†]. In the last section of Chapter 4, the computational process to produce a FEA representation of a spatially averaged stress-wave recording at the piezo-electric transducer location is described.

[†]See section 3.3.2 for further elaboration of spatial averaging of the experimental stress-wave recordings

4.2 Impact modelling by the FEA method

4.2.1 Implicit and explicit FEA modelling

When studying the behaviour of impacts causing plastic deformation of the wear surface, the governing equations of motion are generally non-linear and cannot be solved by analytical methods (see for instance Hamouda *et al*, 1996). Computational methods based on physical laws are therefore generally used to solve complex impact and stress-wave motion problems. The best-known computational technique for solving impact problems is by FEA method. In FEA, the physical system to be modelled is replaced by a discretized system or computational mesh of small elements.

FEA relies on a time step integration method to update stress and strain at each time increment and there are basically two methods; *implicit* and *explicit*. In the *implicit* method the solutions at any time $t + \Delta t$ is obtained by solving for nodal accelerations at each time step. The *implicit* method defines various parts of the model in terms of global stiffness and mass matrices. If the matrices are large, as in the case of complex models, the computational time can be long (Hamouda *et al*, 1996).

In contrast to the *implicit* method, the *explicit* method relies on solving the governing equations of motion at time $t + \Delta t$, based on the knowledge of force equilibrium of individual nodes at time t . The *explicit* method requires much less memory storage as the equilibrium equations can be solved on an element basis rather than on a global basis as required in the *implicit* method. The solution by *explicit* method is stable if the time step is sufficiently small to account for the high frequency modes that dominate the response in wave propagation problems (Hamouda, *et al*, 1996). For axisymmetric shell elements (as used in the stress-wave monitoring sections of this study), the time step Δt for the *explicit* time integration method is automatically determined by the LS DYNA code at the commencement of a simulation and is based on the smallest element size of the model as follows (see for instance the LS DYNA theory manual, 2003)

$$\Delta t = \frac{L_s}{c_{el}} \quad (4.1)$$

where L_s is usually taken as the smallest cross section distance of the smallest element in the model and c_{el} is the bulk elastic longitudinal wave speed defined by equation 3.2

The main advantage of the *explicit* method over the *implicit* method is a significant reduction of the size of the stiffness and mass matrices at each time step, which can result in the reduction of computational time when equations of motion are being solved simultaneously. Generally, the *explicit method* is more suited to dynamic impact problems where the stresses and strains occur over short time frames with stress-wave phenomena being encountered. The *implicit method* is more suited to static or ramped mechanical loading problems, where impact is generally not encountered.

4.2.2 The LS DYNA FEA code

In this study, the LS DYNA[†] FEA code was used as the primary code for the impact and stress-wave monitoring simulations of Chapter 5 and the erosion study of Chapter 6. LS DYNA is specially designed for impact analysis and is used in many applications such as crash analysis modelling in the transport industry, deep drawing and metal forming modelling of sheet metal, explosion modelling i.e. mine explosion and blasting, ballistic impact modelling for military applications and in many other applications where impacts are involved. LS DYNA has both *explicit* and *implicit* solving capabilities and in this study the *explicit* solver was used for the impact simulations. LS DYNA has a vast range of material models ranging from simple elastic models to more complex elasto-plastic models.

As discussed in Chapter 3, the Johnson-Cook material model is available in the LS-DYNA code and was used in this study to model high velocity impacts causing elastic plastic deformation of the wear surfaces. In this study, the FEA model of the experimental system of the sphere, plate and piezo-electric transducer was built using the FEMB[‡] model building software.

[†] LS DYNA produced by Livermore Software Technology Corporation, Livermore CA, USA

[‡] FEMB model building software produced by Engineering Technology Associates, Troy, MI, USA

4.2.3 Axisymmetric modelling techniques

Finite element models can take many forms depending on the geometry of the solids being modelled. The elements available to build the model are generally either solid brick or shell elements. Solid elements are generally used to model thick solid parts, whilst shell elements are used to model thin plate structures. Solid parts with natural symmetry allow the FEA model builder to significantly reduce computational time by slicing the part into one segment (usually quarter or half), thus reducing the number of solid elements required for the model.

If a part has natural symmetry about an axis of rotation (i.e. a solid of revolution), then axisymmetric modelling techniques can be applied. In an axisymmetric model, the geometry and boundary conditions are revolved around 360° and only the cross section of the part needs to be modelled as shown in figure 4.1. The solution for an axisymmetric model will be valid if the loading of the model and material properties are independent of the rotation angle θ .

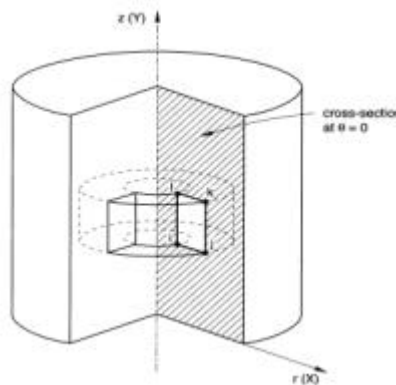


Figure 4.1 Showing an axisymmetric solid. After Hibbett *et al*, 2000

In the stress-wave monitoring sections of this study (Chapter 5), an axisymmetric FEA model of the impacting sphere, wear surface and piezo-electric transducer was used. By using an axisymmetric model rather than a solid model, a number of advantages could be gained in regards to mesh refinement for the purpose of stress-wave analysis.

Later in Chapter 6, the FEA study is extended to investigate impacts and erosion by angular particles impacting the wear surface at oblique impact angles. The angular particle impacts represent experimental erosion test conditions as detailed in section 3.4.

However, to model the erosion test conditions, axisymmetric modelling techniques cannot be used, as the boundary and loading conditions no longer comply with axisymmetric conditions. As will be detailed later in Chapter 6, a solid FEA model was developed for the FEA / experimental erosion comparison study.

4.2.3 Mesh size considerations

One of the main influencing factors involving FEA analysis is the effect of mesh size. In the FEA method, strain hence stress in an element is calculated by a numerical integration process involving the use of *gauss points* within each element. The accuracy of the solutions by the FEA method is related to the number of *gauss points* within each element and the size of the element with respect to the applied stress field (Cook, 1995).

As an example of the numerical integration process, a second order numerical integration solution of the stress field within the element will be obtained when four *gauss points* are used and a third order solution when nine *gauss points* are used. The distance between the *gauss points* will also affect the accuracy of the solution and therefore the way in which deformation of the element occurs. If the *gauss points* are located too far apart (i.e. large element size with respect to the applied stress field), then the solution, hence the deformation of the element may not be accurate. Usually when the elements are too large, the model becomes overly stiff. The numerical integration method of *gauss points* usually *errs* on the side of over stiffness rather than under stiffness. If the element size was progressively reduced from a coarse mesh size, then convergence to a closer agreement of the correct solution can be achieved, which is the method used in this study.

For the impact of a sphere to an infinite elastic plate, Hertz theory provides a valid solution for force, time of contact and surface deformation, which can be used to validate the FEA model solution. To investigate the effects of mesh size in the plate-sphere contact zone, a comparative study was made with Hertz theory for three different mesh sizes of 25, 12.5 and 6 micron, which define the impact zone of the wear surface as shown in figure 4.2. The mesh size of the impacting sphere was maintained at **9mm** for the study.

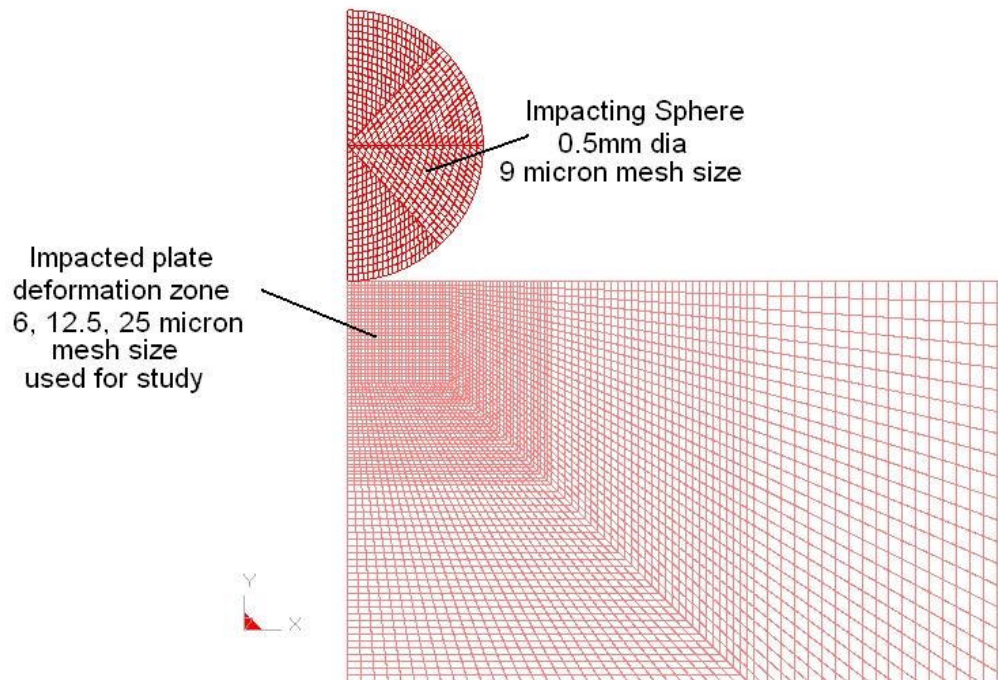


Figure 4.2 FEA model shows the mesh configuration in the contact zone of the 0.5mm sphere and steel plate.

For the study into mesh size effects, an axi-symmetric model was used with constraints placed on all degrees of movement at the base of the plate. Non-reflecting boundary conditions were used on the base and upright edge of the steel plate so that internal wave reflection within the steel plate could be neglected (i.e. to simulate a plate of infinite through thickness and lateral dimensions).

Table 4.1 shows the elastic material properties used for the FEA model / Hertz theory comparison.

Table 4.1 Relevant elastic material properties of AISI 1020 steel and steel spheres, used for the FEA simulation, see Appendix C for material specifications

Material Name	Poisson's ratio	Density	Young's Modulus
Units		kg/m ³	GPa
AISI 1020 steel plate			
0.5mm steel sphere	0.29	7830	205

From Hertz theory, the maximum combined compression z (where $z \equiv z_1 + z_2$, where z_1 is the compression of the sphere and z_2 the compression of the plate) of the spherical particle and steel surface can be calculated as (see for instance, Timoshenko and Goodier, 1970 or Johnston, 1985)

$$z = \left\{ \frac{2.5mV^2}{2K} \right\}^{\frac{2}{5}} \quad (4.2)$$

Where K is the combined stiffness parameter for a sphere impact to an elastic half space, and is given by:

$$K = 0.424 \frac{R^{\frac{1}{2}}}{(h_1 + h_2)} \quad (4.3)$$

where R is the radius of the sphere and h_i is given by:

$$h_i = \frac{(1 - \nu_i^2)}{\rho E_i} \quad (4.4)$$

where in this application $i = 1$ for AISI 1020 steel and 2 for the steel sphere. The time of contact t_c is given by

$$t_c = \left(\frac{m^2}{RE^{*2}V} \right)^{\frac{1}{5}} = 1.45 \text{ ms} \quad (4.5)$$

where E^* is: $E^* = \frac{1}{(X_1 + X_2)}$ and $X_i = \frac{(1 - \nu_i^2)}{E_i}$.

Figure 4.3 shows the results of the FEA simulations for the three mesh sizes considered. The displacement / time curve for Hertz theory can be modelled using the approximation that the displacement profile will be similar in form as the curve defined by $(\sin(\pi t/t_c))^{3/2}$ (see Johnston, 1985). As shown the smallest mesh size of 6 micron gave the closest agreement with Hertz theory for surface displacement and time of contact. For the larger mesh sizes (12.5 and 25 μm), the smaller displacement values are consistent with an overly stiff mesh in the contact zone.

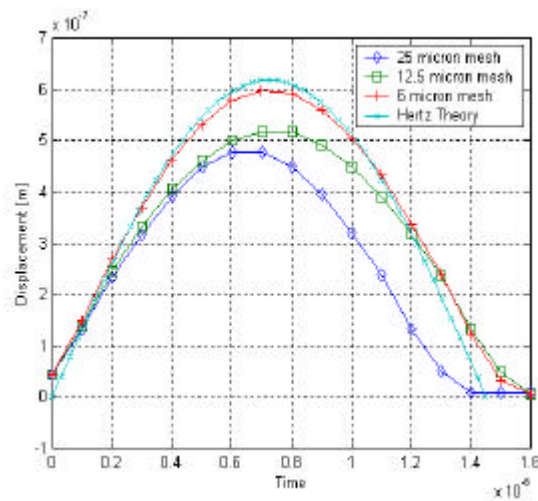


Figure 4.3 FEA model results for three different mesh sizes, which are compared with Hertz elastic theory prediction for surface displacement as a results of an elastic impact by a 0.5mm steel sphere impacting AISI 1020 steel at 2.5 m/s

4.2.4 Numerical stability of the FEA model

In this section, the effects of numerical instability to the stress-wave profile are discussed. In FEA, numerical instability can be caused in a number of ways. Common causes are mesh transitions from smaller to larger elements, insufficient global damping of the structure and hourglass effects. Hourglass effect is a form of numeric instability in which an element may show nodal displacements, however the calculated stress and energy in the element are zero.

Throughout the development of the FEA model it was found that the main effect of numerical instability was the corruption of the stress-wave by high frequency *noise*. Another form of numerical instability was encountered when the contact algorithm was applied for the contact between the wear material and the piezo-electric transducer. The issues relating to numerical instability when the contact algorithm was applied will be discussed later in section 4.2.6. To overcome the high frequency *noise* problem, various mesh configurations were investigated to improve the quality of the stress-wave profile. Global damping was also investigated, however the *noise* caused by the numerical instability was of a much higher frequency than the actual stress-wave signature, and therefore any attempt to damp out the high frequency noise would also result in the damping of the stress-wave as well. Further investigation of the numerical instability revealed that it was sensitive to the material model used to model the plastic deformation of the surface. This material model was the Johnson-Cook model. To overcome the numerical instability, it was decided to model the impact zone of the wear surface where the plastic deformation would occur with the Johnson-Cook material model, and away from the wear surface where the stress levels were well below the yield stress of the material, an elastic material model was used. By using a two-model approach, the Johnson-Cook material model would be used for elasto-plastic deformation of the wear surface and the elastic model used for the elastic wave propagation through the bulk material.

It is unclear as to the cause of the numerical instability when the Johnson-Cook model was used to model the whole of the impacted wear material (i.e. the whole 10mm thick plate). Other LS DYNA material models (e.g. plastic kinematics model, see for instance the LS DYNA theory manual (2003) for full details) which is also designed to model plastic deformation were trialed and were found to be stable for stress-wave motion for the whole of the impacted wear material. As described in Chapter 2, the Johnson-Cook model is well suited for high strain-rate impact analysis and it was therefore important to retain it in the final FEA model. The next section describes the model configuration using the Johnson-Cook model for the impact zone and the elastic model for the bulk wear material.

4.2.5 Mesh size consideration for elastic stress-wave motion

As described in section 4.2.3, the comparative study with Hertz theory showed that a fine mesh of $6\mu\text{m}$ for the steel plate was desirable to model the surface deformation characteristics of the impact event. However, maintaining the same mesh size throughout the bulk of the steel plate would be undesirable, as the number of elements would be high (approaching 1 million to model the plate / sphere system) and significantly slow down computational time. Also a million elements are at the limits of the FEA model-building program (FEMB) and the post analysis program (Post GL) as used in this study[‡]. The trade off between element size and numerical instability of the stress-wave is also a concern. On the one hand, larger elements will result in lower computational times and on the other, the stress-wave recording may show effects of numerical instability due to greater distance between integration points (i.e. *gauss points*).

The influencing factors of element size to model the bulk of the wear material and numerical instability of the stress-wave recording culminated in a final configuration of the FEA model as shown in figures 4.4. As shown, the Johnson-Cook model was used in the impact zone for a distance 0.375mm in the x and y directions. In the extremities of the impact zone region (modelled by the Johnson-Cook model), it was shown that the maximum stress level was well below 100MPa (for an impact to steel at 104m/s, the highest impact velocity considered in this study). The 100MPa stress value is well below the yield stress of AISI 1020 steel (350 MPa), therefore allowing an elastic material model to be used beyond the region defined by the Johnson-Cook model. As illustrated in figure 4.4, from the distance of 0.375 to 1.5mm in the x and y directions, the mesh was progressively coarsened from $6\mu\text{m}$ to $50\mu\text{m}$, where from then on, the $50\mu\text{m}$ element size was maintained throughout the rest of the model.

[‡] FEMB and POST GL produced by Engineering Technology Associates, Troy, MI, USA

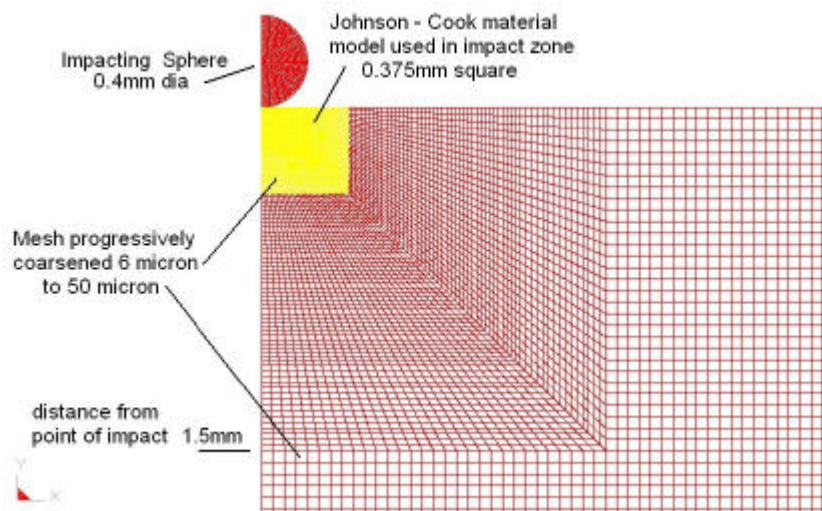


Figure 4.4 Axisymmetric model of impacting sphere and wear plate

Figure 4.5 shows the FEA model in its entirety. The use of axisymmetric elements allowed the model to be built using less than 100,000 elements. The FEA model was designed to model the experimental system of the sphere, impacted plate and piezo-electric transducer and model dimensions shown in figure 4.5 are exact to the experimental system.

The model constraints were designed to simulate experimental conditions with the main support of the impacted plate being provided by the base of the piezo-electric backing (i.e. transducer base). To simulate the clamping of the wear material to the piezo-electric transducer in the experiment (see for instance section 3.3.3), the boundary conditions were to constrain the upper right edge of the model (as shown in figure 4.5). No other boundary conditions were required as the axisymmetric boundary constraints are automatically assumed when axisymmetric shell elements are used in the model. As detailed in the next section, a contact algorithm was used to model the impact of the sphere with the wear surface and to model the contact between the wear material and the piezo-electric active element.

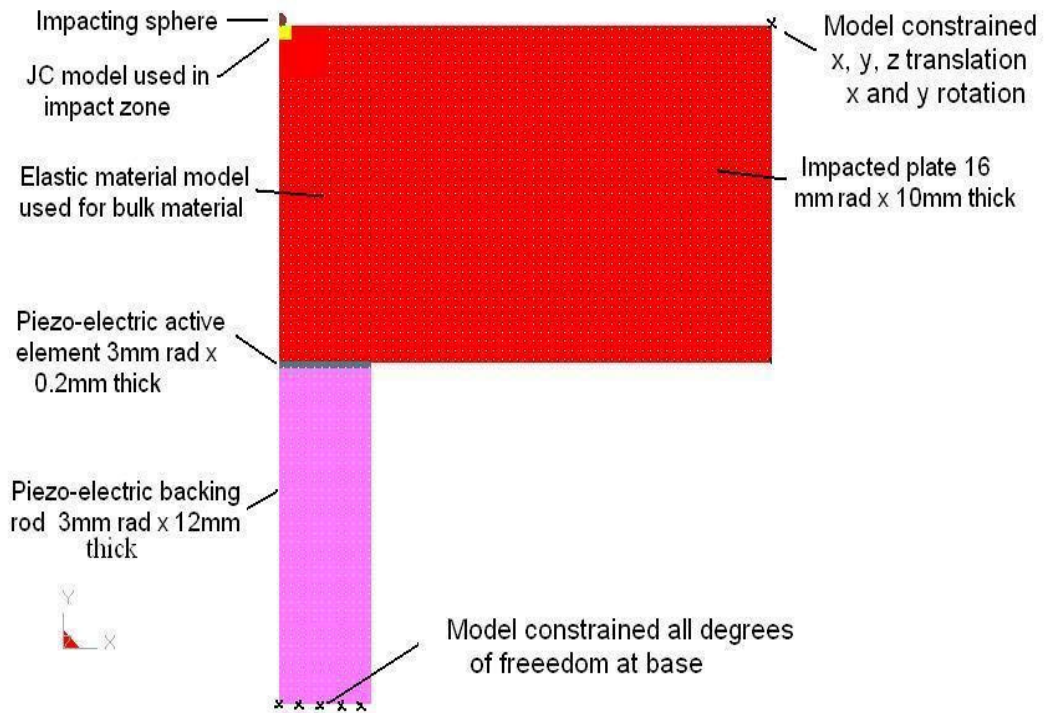


Figure 4.5 Axisymmetric FEA model of experimental system

4.2.6 FEA modelling of contact

To model contacting parts in the FEA model, a contact algorithm is required. In the FEA model, there were essentially two contacts to be modelled; the first is the contact of the impacting sphere and wear surface and the second is the contact between the rear of the impacted wear material and the piezo-electric transducer. The second contact algorithm is required, as it cannot be assumed that the wear material and the piezo-electric transducer are a continuum. At the interface, wave reflections will occur due to the acoustic mismatch of the wear material and the piezo-electric sensing element and the stress-wave transmitted to the piezo-electric material may actually change phase and amplitude. The effects of wave reflections at the contact interface can also cause separation of the wear material and the piezo-electric transducer to occur as a result of dynamic forces. Modelling the contact interface will be an important aspect of the stress-wave monitoring study.

The LS DYNA code uses contact algorithms to check for penetration of bodies coming into contact with each other and there are a number of different contact algorithms for specific applications. In the LS DYNA code, the *2-Dimensional Automatic Surface-to-*

This page left intentionally blank

Surface contact algorithm uses automatic searching imbedded in the code to check for part penetration. The two-dimensional contact is suitable for axisymmetric models. The contact algorithm relies on the penalty stiffness method, which essentially applies normal resistive springs forces between the contacting bodies to prevent part penetration.

For the contact at the surface (the sphere and the impacted plate), the default parameters in the LS DYNA code of the *2-D Automatic Surface-to-Surface* contact algorithm were shown to be suitable. The default parameters could be confirmed by the mesh size study of section 4.2.3, which showed that surface deformation was in close agreement with Hertz elastic theory. However, when the default parameters of the contact algorithm were used for the wear material-piezo-electric transducer contact, the stress-wave signature again showed signs of numerical instability in the form of high frequency *noise*. The reason for the instability appeared to be related to the spring force constant in the contact algorithm, which is designed to model the contact interface stiffness. To understand and overcome the numerical instability problem for the implementation of the wear material / piezo-electric transducer contact, the physics of the experimental contact interface was studied by considering the following aspects. In the experimental system and on a microscopic level, contact between the wear material and piezo-electric transducer will occur on asperities, even though the face of each part was finely ground. Low viscosity oil was also used as a coupling medium to remove air from gaps between the contacting surfaces and to improve stress-wave transmission (see figure 4.6 below).

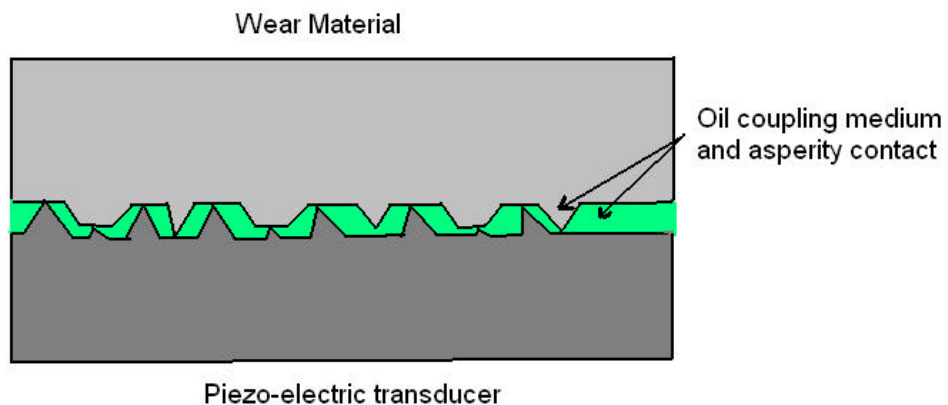


Figure 4.6 Illustration of contact (microscopic level) between wear material and piezo-electric transducer

This page left intentionally blank

The effect of the oil coupling medium and asperity contact may result in the lowering of the contact stiffness at the interface. Another possible scenario is that the low viscosity oil may in fact separate the wear material and the piezo-electric transducer, resulting in a hydrodynamic lubrication effect. In this case the contact stiffness at the interface would not depend on the wear / piezo-electric material contact stiffness but on the bulk modulus of the oil. The contact stiffness k , is defined in the contact algorithm as (see LS DYNA theory manual, 2003)

$$k = \frac{S_f B_m A^2}{V} \quad (4.6)$$

where S_f is a scaling factor, B_m is the bulk modulus usually taken as the bulk modulus of the master part (where the master part is defined as the part transmitting the force across the boundary and the slave part is the recipient of the transmitted force), A is the face area and V the volume of the contacting elements.

There are two possible variations of the contact algorithms that can be used to model the physical nature of the contact interface. If the scaling factor of equation 4.6 was set to unity then it is assumed that the contact stiffness at the interface would be modelled by the stiffness of the master part. This would be equivalent to a one-dimensional stress-wave model where the contact surface of each part would move in unison when subjected to an incident stress-wave, as shown in figure 4.7a. If the contacting parts were however modelled taking into account the physics of either the asperity contact or hydrodynamic lubrication effects, then the interface would contain a compliant spring between the wear material and the piezo-electric transducer, which is modelled in the contact algorithm of equation 4.6, using a scaling factor less than unity (figure 4.7b).

Later in Chapter 5, results of experimental stress-wave recordings are compared with the FEA model results. The comparison study will focus on the contact model issues presented in this section.

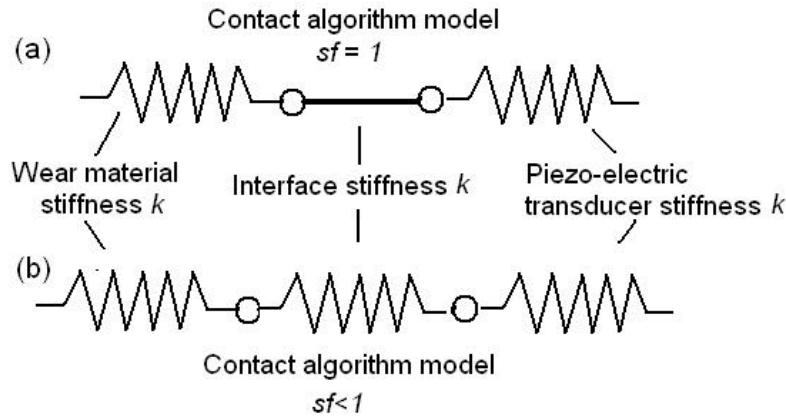


Figure 4.7 Model of contact between wear material and piezo-electric transducer (a) contact model assuming stiffness of master part (b) compliant contact model

4.2.7 Equation of State

An equation of state (EOS), which is used in the FEA model to define the thermodynamic state of the material, is required for the implementation of the Johnson-Cook material model. A linear polynomial equation of state, which has constants relating to higher powers of the compressive volumetric strain, was used for the FEA study. The volumetric pressure P is defined by the equation of state as

$$P = c_0 + c_1 \mathbf{m} + c_2 \mathbf{m}^2 + c_3 \mathbf{m}^3 + (c_4 + c_5 \mathbf{m} + c_6 \mathbf{m}^2) \mathbf{r}_0 E \quad (4.8)$$

where \mathbf{m} is defined as

$$\mathbf{m} = \frac{\mathbf{r}}{\mathbf{r}_0} - 1 \quad (4.9)$$

where $\mathbf{r} / \mathbf{r}_0$ is the ratio of the current density to initial density. The higher terms of equation 4.8 (c_2 - c_6) relate mainly to the modelling of ideal gas or solid to liquid phase changes. In this study, the impacts although causing significant plastic deformation of the surface and localised heating do not cause a phase change to occur. The normal practice in applying the linear polynomial EOS for impacts where phase changes are not encountered is to set c_1 equal to the elastic bulk modulus of the wear material and all other c terms set to zero (see for instance, LS DYNA theory manual, 2003).

4.2.8 Spatial averaging considerations of FEA model

As discussed in section 3.2.2, the design and location of the piezo-electric sensing element was optimised by considering the effects of spatial averaging as a result of a curved stress-wave passing through a flat piezo-electric sensing element. In this section, the same considerations need to be applied to the FEA model in order to compare experimental and FEA stress-wave profiles directly.

Figure 4.7 shows an FEA model simulation of the leading longitudinal stress-wave travelling on a spherical path and approaching the piezo-electric sensing element at 10mm below the point of impact[†]. The figure gives some insight as to the wave curvature in relation to the dimensions of the piezo-electric sensing element. Also shown in the figure is the stress variation along the wavefront, where higher stress levels are shown near the centre axis of the model and lower stress values moving away from the centre axis.

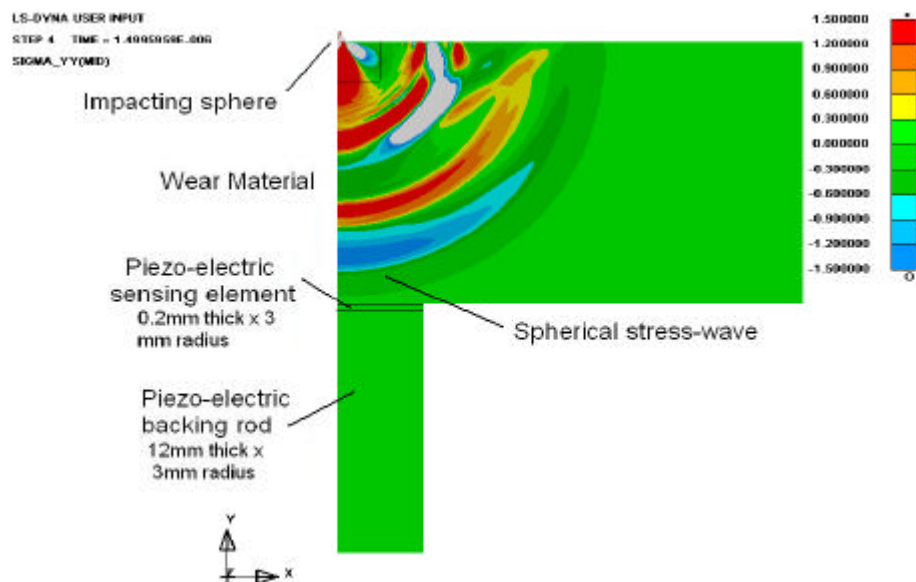


Figure 4.7 FEA simulation of stress-wave motion produced by impact to 10mm thick 1020 steel by a 0.4mm zirconia sphere at 104m/s

[†]FEA simulation of 0.4mm zirconia sphere impact to AISI 1020 steel at 104m/s, full details of FEA material properties obtained in table 5.1 and 5.2, in chapter 5

This page left intentionally blank

In the experimental study, the piezo-electric transducer will produce a spatially averaged recording of the stress-wave no matter how the stress-levels may change across the wave. This spatial averaging process must also be applied to the FEA stress-wave at the piezo-electric sensing location in order to compare the experimental stress-wave forms with the FEA model prediction. To obtain a spatially averaged response from the FEA model the stress-time profile of the y-stress component of the stress-wave was obtained at 10 equally spaced elements within the piezo-electric sensing element, as shown in figure 4.8.

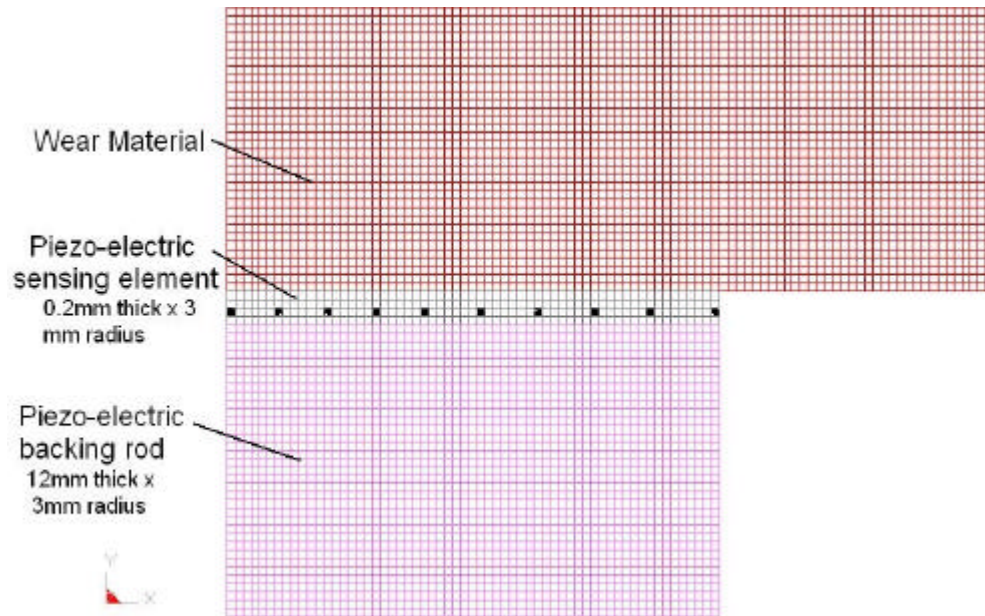


Figure 4.8 Showing location of 10 equally spaced elements used to obtain spatially averaged stress-time profile

The spatially averaged stress-time profile was then obtained by numerical integration as follows

$$\mathbf{s}(t) = \sum_{i=1,n} \mathbf{s}_y(t) A_i / A_p \quad (4.9)$$

where \mathbf{s} is the spatially averaged stress-wave profile after numerical integration and A_i is the area of the annulus at each location on the sensing element, making up the total area A_p of the piezo-electric sensing element. By transforming the FEA stress-wave

profile at the sensing location to a spatially averaged recording, direct comparison of the experimental and FEA recording could be made.

4.3 Chapter summary

In this Chapter, the FEA modelling process used for the study of small particle impacts and stress-wave motion was discussed in detail. In the first section of this Chapter, a general overview was presented on aspects of FEA modelling. For the study of normal impacts, it was shown that axisymmetric modelling techniques could be used to simplify the model and reduce computational time. The deformation of the wear surface in the impact zone was also an important consideration as surface deformation is the main driver of stress-wave motion. A comparison study was made with Hertz elastic theory to determine a suitable mesh size to model the impact zone effectively.

In the following section, the effects of numerical instability of the FEA stress-wave recording were discussed. It was found that the main cause of the instability was due to the Johnson-Cook material model, however the reason for this was not clearly understood. As the Johnson-Cook model was an integral part of the impact and stress-wave monitoring study, it was important to overcome the numerical instability effects. It was found that if the Johnson-Cook model was used for the impact zone only where plastic deformation takes place and an elastic model used to model the bulk of the wear material; the issues of numerical instability of the stress-wave could be overcome.

The FEA model required the use of contact algorithms to define the contact between the impacting sphere and the wear material and the contact between the wear material and piezo-electric sensing element. It was found that the default parameters of the contact algorithm were suitable to model the sphere / wear surface contact. However when the default parameters of the contact algorithm were applied for the wear material / piezo-electric contact, numerical instability was also detected in the FEA stress-wave recording. A discussion based on the physics of the experimental contact interface concluded that the contact of the wear material and piezo-electric transducer could occur on asperities of each surface or the inclusion of the oil coupling medium may in effect, separate the wear material from the piezo-electric transducer. Further discussions

surrounding the issues relating to the modelling of the contact interface by the FEA method will be discussed in Chapter 5.

In order to compare the experimental stress-wave recording with the stress-waves produced by the FEA study, the effects of spatial averaging to the stress-wave must be considered. In the last section of this Chapter, the process of obtaining the FEA stress-wave recording at the piezo-electric sensing location was described. The method involved a numerical integration process of ten equally spaced elements across the face of the piezo-electric sensing element. By completing the numerical integration process, it is possible to compare the experimental and FEA stress-wave profiles directly.

This page left intentionally blank

CHAPTER 5

STRESS-WAVE MONITORING RESULTS

5.1 Introduction

In this Chapter, results of the combined experimental and FEA impact and stress-wave motion study of AISI 1020 steel, UHMWPE (ultra high molecular weight polyethylene) and VER (vinyl ester resin) are presented. The Chapter is divided into two main sections. The first part is devoted to the impact and stress-wave monitoring study of AISI 1020 steel and the second part to the polymer materials. AISI 1020 steel was chosen as the initial test specimen because the material property characteristics of the steel are more readily available than the polymer materials. The impact and stress-wave monitoring experiments of the AISI 1020 steel specimen and modelling of the experimental system by the FEA method, provide a valuable learning tool for understanding the limitations of both the transducer response and the FEA code.

In the first section of this Chapter, the Johnson-Cook material model is discussed and implemented for the FEA analysis. As a starting point it was decided to use input values for the model obtained from published works involving Split Hopkinson's Pressure Bar (SHPB) experiments at strain rates up to 10^2s^{-1} . The strain-rates from the small particle impacts to the AISI 1020 steel wear surface will be considerably larger, in the order of 10^6s^{-1} . The impact and stress-wave monitoring study of AISI 1020 steel allows an excellent opportunity to validate parameters of the Johnson-Cook model at strain-rates up to three orders of magnitude higher than previously published results.

In the following section of this Chapter, the stress-waves produced from low velocity impacts to the AISI 1020 steel surface are compared to FEA model prediction. The low velocity impacts study was designed as a preliminary study to develop the stress-wave

monitoring technique for impacts at the surface, which could be considered as predominantly elastic. In this sense, the low velocity impact study provides a valuable case study for an experimental system, which can be easily adapted for modelling by the FEA method.

Following the low velocity impact study, the combined experimental / computational approach of the stress-wave monitoring method is extended for higher velocity impacts to the AISI 1020 steel wear surface. In this section of the study, insight will be gained in the area of the transducer response to the passage of the stress-wave and how the stress-wave recordings may be related to material properties at the surface.

For any new experimental procedure it is always advisable to validate the process by another method. In the following section of this Chapter, the extent of plastic deformation at the surface is evaluated by measurement of the impact craters left by the small particle impacts. This section is designed to validate the FEA model parameters relevant for plastic deformation of the surface.

The last section of this Chapter is devoted to impact and stress-wave monitoring of UHMWPE and VER. UHMWPE is a unique material exhibiting extraordinary impact and wear resistant properties. In contrast, VER shows relatively poor erosion resistance and could be classed as a brittle polymer material. This section allows the opportunity to assess the robustness of the stress-wave monitoring process, when applied for the impact and erosion study of polymer materials.

5.2 Experimental and FEA study of impacts and stress-wave motion of AISI 1020 steel

5.2.1 Implementing the Johnson-Cook FEA material model

As described in section 2.2.1, the Johnson-Cook model is a widely accepted strength model for the study of high strain-rate loading to FCC (face centred cubic) and BCC (body centred cubic) materials, in which AISI 1020 steel falls into the FCC category. The Johnson-Cook model is empirical in nature and simple to apply as it is based on

simple scalar expressions for yield and flow stress as a function of strain, strain-rate and temperature. The material model expresses the von-Mises stress as

$$\mathbf{s}_{vm} = [A + B\mathbf{e}^n][1 + C \ln \dot{\mathbf{e}}][1 - T^{*b}] \quad (\text{Equation 2.13 reproduced})$$

The parameters in the first bracket of the model are derived from experimental tensile test results under low strain-rate or quasistatic conditions, where A is the yield stress and B and the exponent n are strain-hardening terms. The quasistatic terms are derived from *curve fitting* of the stress-strain curve derived from tensile test results. These terms for AISI 1020 steel are usually readily available either from the manufacturer or published tensile test results. The second and third brackets essentially scale the stress-strain curve according to strain-rate and thermal softening effects. Strain-rate effects for AISI 1020 steel are expected to show an increase in yield and flow stress, whilst thermal effects cause softening, hence lower load carrying ability.

As the model has five parameters that must be derived, it was decided in the current study to use parameters from published experimental results as a starting point. With the parameters in the first bracket of the model being essentially quasistatic terms, these parameters could be held constant. This leaves the strain-rate parameter C and the temperature coefficient b to be determined. Values for C , B , n and b were obtained from published works by the original authors of the model, Johnson-Cook (1983), based on the study of AISI 1006 steel. The main difference between AISI 1006 and AISI 1020 steel is the carbon content in which AISI 1006 steel contains 0.08% and AISI 1020 steel has a higher content of between 0.17 to 0.23% by weight (see Appendix C for material specifications of both steels).

The strain-rate and thermal parameters from the Johnson-Cook study for AISI 1006 steel were obtained at the relatively low strain-rates of 100s^{-1} . The strain-rates of the impacts to the AISI 1020 steel surfaces in this study will be at least three orders of magnitude higher, in the order of 10^5 - 10^6s^{-1} .

Table 5.1 shows the elastic material properties and table 5.2 shows the Johnson-Cook model parameters required for the FEA model.

Table 5.1 Elastic material property parameters for the FEA model obtained from manufacturers material specification data sheets, see Appendix C for details.

Material	E GPa	G GPa	ρ kg/m ³	ν Poisson's ratio	Specific heat J/kg K	Thermal Conductivity W/mK
AISI 1020 steel Steel spheres	207	81	7830	0.29	480	42
PIC 151 piezo- electric	54		7800	0.28		
Zirconia spheres	134		3990	0.26	280	21

Table 5.2 Johnson-Cook material property parameters for the FEA model, non-referenced material properties available in Appendix C.

Material	A MPa	B MPa	n	C	T_{room} Deg C	T_{melt} Deg C	b	B_m GPa
AISI 1020 steel	350	270 ref Johnson- Cook (1983) for AISI 1006 steel	0.36 ref Johnson- Cook (1983) for AISI 1006 steel	0.022 ref Johnson-Cook (1983) for AISI 1006 steel	25	1400	1	140

5.2.2 Experimental and FEA stress-wave monitoring study of AISI 1020 steel under low velocity impact conditions

In this section, the newly designed piezo-electric transducer was used to monitor stress-waves produced from low velocity impacts to the AISI 1020 steel wear surface. In the study, the impacts at the wear surface could be assumed to be predominantly elastic. The low velocity impact study could be considered as a preliminary study for higher velocity impacts (section 5.2.4), which will cause significant plastic deformation of the wear surface.

The experimental procedure for the low velocity drop impact experiment is shown in figure 5.1. For the experiment, steel spheres of $0.5mm \pm 0.02mm$ diameter were dropped from a height of $320mm$ onto the AISI 1020 steel plate below. The impacts were to the centre of the plate and wave reflections from the vertical boundaries could be neglected. The plates were machine polished on both sides using silicon carbide abrasive paper, up to 2000 abrasive grit size, until a smooth *mirror* finish was achieved.

The resultant stress-wave recordings for six individual impacts to the steel plate are shown in figure 5.2.

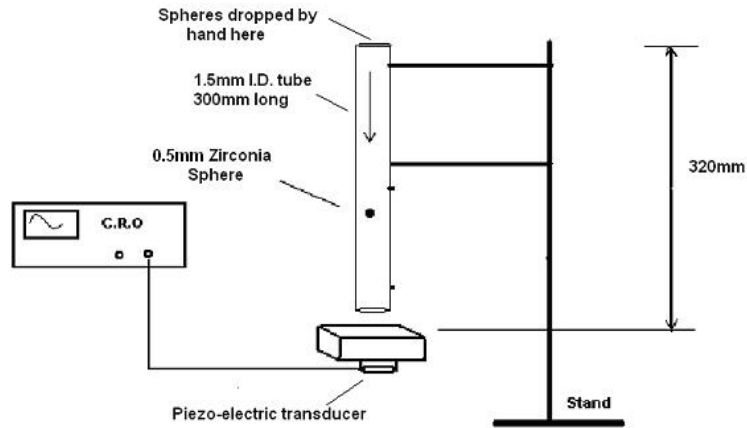


Figure 5.1 Experimental apparatus for low velocity drop impact experiment

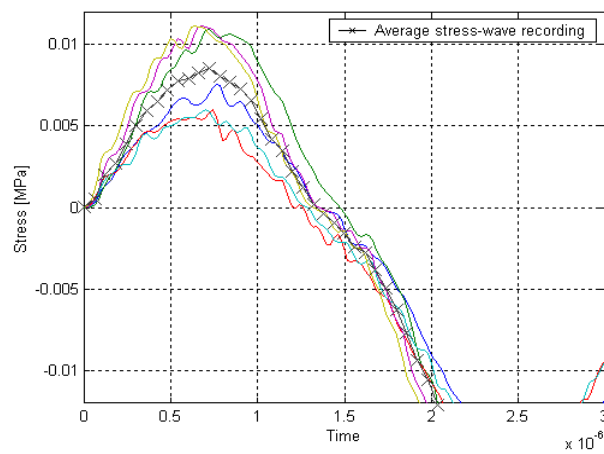


Figure 5.2 Stress-wave recordings from impacts to 10mm thick AISI 1020 steel impacted by 0.5mm steel spheres at 2.5m/s, the recordings were obtained at the rear face of the impacted plate

As shown in figure 5.2, an averaged stress-wave recording obtained from six individual impacts to the AISI 1020 steel wear surface was derived for comparison with the FEA model result.

Before the experimental stress-waves can be compared with the FEA model results, a correction factor needed to be applied to the experimental recordings. As described in

section 3.3.7 the amplitude of the experimental stress-waves needed to be scaled by the factor of 6.1 to account for the voltage amplitude reduction as a result of the electrical impedance mismatch of the piezo-electric transducer (5.1M Ohms impedance) and the recording device, the cathode ray oscilloscope (1M Ohms impedance). As discussed in section 3.3.7, a simple voltage divider electrical model was used to obtain the scaling factor defined below

$$V_{out} = \frac{1M\Omega}{(5.1M\Omega + iZ) + 1M\Omega} V_s \approx \frac{1}{6.1} V_s \quad (\text{Equation 3.7 reproduced})$$

where the frequency dependant component iZ , was shown to be negligibly small at the frequency at which the piezo-electric transducer will be used for the stress-wave monitoring experiments. Subsequently, the amplitude of all experimental stress-waves shown in coming sections were scaled by the factor of 6.1 as described in equation 3.7.

Other issues, which can affect the quality of the stress-wave recordings, are the issues relating to the curvature of the stress-wave (i.e. spatial averaging effects, see sections 3.3.1 and 4.2.8) and the coupling of the piezo-electric transducer to the wear material (see section 4.2.6 for coupling considerations). As discussed in section 4.2.8, a numerical integration process was conducted to convert the FEA waveform to a spatially averaged representation of the waveform at the piezo-electric transducer location. The conversion allows the experimental and FEA waveforms to be compared directly.

As discussed in section 4.2.6, it was not clear how the contact interface of the experimental system would affect the phase and amplitude of the recorded stress-wave. As mentioned, even though the wear material and piezo-electric transducer were finely polished and firmly clamped together, contact between the two parts may occur on asperities of each face or the parts may in fact be separated by the inclusion of the oil-coupling medium (i.e. causing an hydrodynamic lubrication effect). Another possible scenario is the transmission of tensile stresses across the contact interface may be restricted due to the fact that the wear material and piezo-electric transducer are

clamped and not bonded together. As shown in Chapter 1 (section 1.3, figure 1.8), the stress-waves from the impact event showed compressive and tensile stress components in the waveform. A waveform of high frequency having compressive and tensile stress may actually change phase when transmitted to the piezo-electric transducer, as the only possible mechanism for the tensile stress to propagate across the contact interface is a suction effect from the oil-coupling medium. The experimental and FEA study presented in this section and the high velocity impacts study (section 5.2.4) will address the contact interface issues and the subsequent effects to the waveform.

The discussion of section 4.2.6 showed that two possible contact models were possible depending on the stress-wave transmission mechanism across the contact interface between the wear material and the piezo-electric transducer. The LS DYNA code can model contact between parts when a contact algorithm is specified. In the LS DYNA code, the penalty stiffness method is applied to essentially place resistive spring forces between contacting parts to prevent part interpenetration. In the contact algorithm of the LS DYNA code, the penalty stiffness spring constant k , is given by

$$k = \frac{S_f B_m A^2}{V} \quad \text{(Equation 4.6 reproduced)}$$

where S_f is a scaling factor, B_m the bulk modulus and A and V are the face area and volume of a contact element. As discussed in section 4.2.6, if S_f was set to unity then the contact interface would be assumed to be an ideally stiff contact model (ISC model) and the phase and amplitude of the stress-wave transmitted to the piezo-electric transducer would be unaltered. The ISC model represents the case of one-dimensional stress-wave theory across the contact interface (see for instance Goldsmith, 1960). However if a compliant contact model (CC model) was assumed based on the theory of asperity contact or separation of the contacting surfaces by the oil-coupling medium, then S_f will be less than unity and a phase and amplitude variation may occur to the transmitted stress-wave. The CC model also allows separation to occur at the contact interface in the event that dynamic forces cause separation to occur. The ISC model also uses the same contact algorithm, allowing separation to occur at the contact interface, however as will be explained, numerical instability problems were encountered.

When implementing the contact algorithm for the FEA study, it was noted that ambiguous stress-wave results were obtained from the FEA model when the scaling factor sf of equation 4.6 was set to unity i.e. simulating the ISC model. To overcome the problem, it was decided to remove the contact algorithm for the ISC model simulations and tie coincident nodes at the contact interface of the wear material and piezo-electric transducer together (see figure 4.5 for specific FEA model geometry). With the FEA model in this configuration, the boundary nodes of the wear material / piezo-electric transducer interface will move in unison. The ISC model will also transmit compressive and tensile stresses in an un-altered state across the interface as the ISC model now represents an experimental system of the wear material and piezo-electric transducer in a bonded state at the interface. As stated earlier in this section, the wear material and piezo-electric transducer were firmly clamped and not in fact bonded together. Nonetheless, the comparison study of the ISC model with experimental stress-wave recordings should give an understanding of tensile stress transmission characteristics and any dependence on wave frequency affecting the phase and amplitude of the transmitted stress-wave.

For the FEA model simulations in this section and section 5.2.4, a comparative study of stress-wave recordings was conducted using the ISC model, the CC model and experimental stress-wave recordings.

A preliminary study was conducted to obtain a value of sf ($= 0.0027$ from equation 4.6) for the CC model by conducting a calibration process of the FEA model and experimental stress-wave recordings, in which the stress-wave amplitudes were calibrated. The basis of the approach was that it was theorised that the penalty stiffness force to prevent part penetration in the FEA model would be the same as the resistive force of the experimental contact interface. In the calibration process, the entire range of impact velocities was considered (i.e. 2.5, 21, 52 and 104m/s, results of impacts above 21m/s are presented in section 5.2.4). It was considered that if a CC model was suitable to model the experimental contact interface, then the penalty stiffness spring constant k of the FEA contact algorithm (equation 4.6) should be relatively constant over the range of impact velocities considered. After several iterations of the FEA model for each impact velocity, the value obtained for sf was shown to be approximately constant across the range of impact velocities.

The low value for sf ($= 0.0027$) was a surprising result as the value suggests a very flexible contact interface is required to model the experimental system. As will be shown in coming sections, the stress levels at the contact interface are low ($<0.4\text{MPa}$) in comparison to the contact stress levels at the wear surface (approximately 1200MPa). The low value for sf suggests that the penalty stiffness approach to prevent part interpenetration may be dependant on the applied stress field rather than the stiffness of the contact interface as detailed in equation 4.6.

The results of the experimental and FEA impact and stress-wave study are shown in figure 5.3. Close agreement was shown between the experimental stress-wave recording and the FEA model when the ISC model was used (i.e. representing $sf = 1$). The CC model (i.e. $sf = 0.0027$) showed much faster rise time from zero stress to maximum amplitude and the wave period (i.e. when the first zero crossing is considered) was shown to be well below the experimental result.

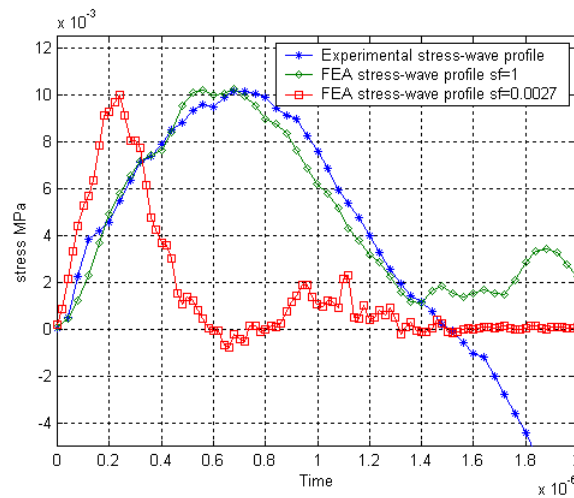


Figure 5.3 Experimental and FEA stress-wave profile recorded at the piezo-electric transducer location located at the rear face of the impacted plate, 10mm from the impact site. Stress-wave produced by impact of 0.5mm steel sphere to AISI 1020 steel at 2.5m/s

The results showed that the CC model might have given ambiguous results, as the waveform characteristics are vastly different to the experimental recording. A possible cause of the ambiguity is that the stress levels at the contact interface may be too low to model the contact interface using the penalty stiffness method invoked by the contact

algorithm. In contrast, the close agreement of the ISC model with experimental results indicates that for low velocity impacts and stress-wave frequencies of approximately 0.35MHz (based on calculations of wave frequency = $1 / 2 \times$ the wave period), the contact interface can be modelled by the FEA method using the ISC model assumptions.

The main conclusions from the low velocity impact study are

1. The close agreement between FEA model and experimental stress-wave amplitudes indicates that the electrical coupling model and the scaling factor derived from the model was accurate
2. The ISC model showed good agreement between the experimental result in regards to amplitude and phase of the recorded stress-waves for the impact velocity and wave frequency of the stress-wave considered
3. The CC model showed ambiguous results which could be caused by some form of numerical instability in the implementation of the contact algorithm in the LS DYNA code

5.2.3 Experimental impacts to AISI 1020 steel at higher impact velocities

The higher velocity impact experiments were conducted using the gas-blast erosion test rig described in detail in section 3.3.1. In the experimental study, zirconia spheres of approximately 0.4mm diameter were used as the impacting medium. As with the low velocity drop impact experiment (described in the previous section), six individual stress-waves were recorded for impact velocities at 21.5, 52.5 and 104m/s. The average of six stress-wave recordings was later used for comparison with the FEA computational model (section 5.2.4).

Figures 5.4 to 5.6 show the stress-wave recordings for each impact velocity. As shown the stress-wave recordings were re-producible as indicated by the consistent stress-wave profiles in regards to amplitude and phase for each impact velocity considered.

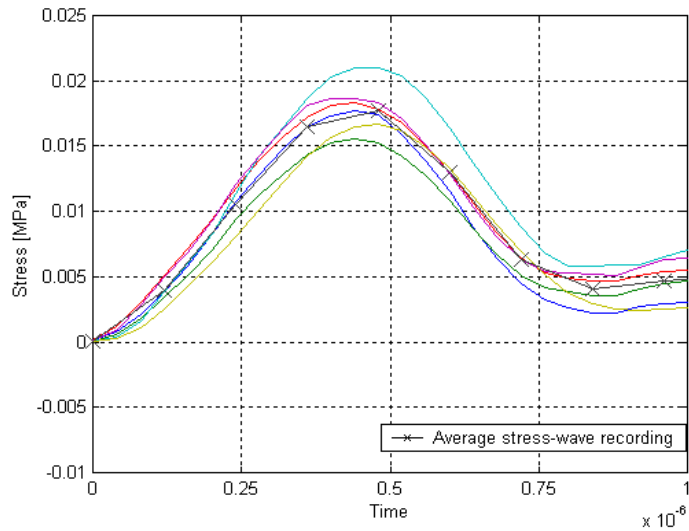


Figure 5.4 Experimental stress-wave recording of impacts by 0.4mm zirconia spheres to 10mm thick AISI 1020 steel at 21.5 m/s

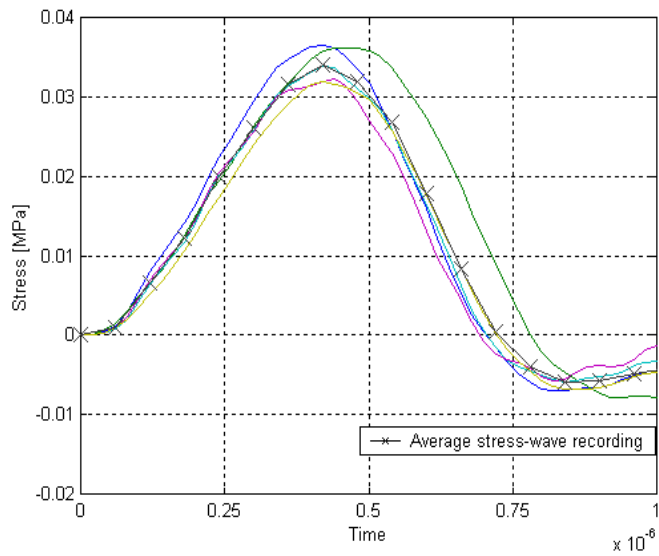


Figure 5.5 Experimental stress-wave recording of impacts by 0.4mm zirconia spheres to 10mm thick AISI 1020 steel at 52.5 m/s

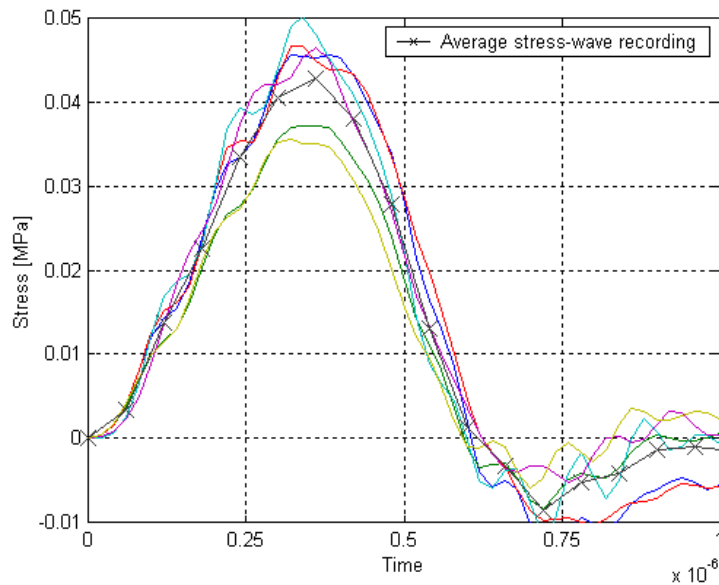


Figure 5.6 Experimental stress-wave recording of impacts by 0.4mm zirconia spheres to AISI 1020 steel at 104m/s

5.2.4 Comparison of experimental and FEA stress-wave recordings of AISI 1020 steel under higher velocity impact conditions

In this section, the results of the FEA and experimental stress-wave recordings are compared. The main aim of studying the higher velocity impacts is to

1. Gain an understanding on the transducer response as the impact velocity is increased
2. Validate key material property parameters of the Johnson-Cook material model by the stress-wave monitoring method under conditions equivalent to erosive impact conditions

As discussed in the low velocity impact study (section 5.2.2), two FEA models having an ideally stiff contact (ISC model) or compliant contact (CC model) at the contact interface between the wear material and the piezo-electric transducer were developed. The results of the higher velocity experimental and FEA stress-wave comparison study are shown in figures 5.7 to 5.9. It was noted in figure 5.7 (21m/s impact), that the stress-wave profile for the CC model was completely out of phase with the experimental

recording. A similar result was shown for the CC model in the low velocity impact experiment, as detailed in section 5.2.2. It is also noted in figure 5.7, that the ISC model is in close agreement with the experimental result in regards to amplitude and phase of the stress-waves. The close agreement of the ISC model and experimental waveform is also consistent with the low velocity impact study of section 5.2.2.

A trend is now apparent, which indicates that the ISC model works effectively for low velocity impacts as evident by the agreement between experimental and FEA waveforms at 2.5m/s and 21.5m/s (figures 5.3 and 5.7). However, as shown in figures 5.8 and 5.9 (impacts at 52 and 104m/s), the CC model is in closer agreement with the experimental results in regards to amplitude and phase of the experimental stress-waves. In the same figures, the ISC model was shown to have a higher wave amplitude and shorter duration for the wave period (i.e. when comparison of the first zero crossing is considered) than the experimental result. The higher velocity impacts also show a trend of a much faster transition from compressive stress to tensile stress as shown in the ISC model results of figures 5.8 and 5.9. As stated earlier in section 5.2.2, the ISC model will transmit compressive and tensile stress across the contact interface in an un-altered state as interface nodes between the wear material and piezo-electric transducer have been tied together. The comparison study of the ISC model and experimental results indicates that a limitation has been reached as to the maximum frequency of a stress-wave, which can be transmitted across the contact interface without a phase transition occurring. From the 21m/s impact where the ISC and experimental stress-waves were relatively in phase, the frequency limitations of the experimental system could be estimated at approximately 0.9MHz (based on the frequency calculations of $1 / 2 \times 0.55\text{ms}$, where 0.55ms is the time of the first zero crossing of the experimental stress-wave at the impact velocity of 21m/s).

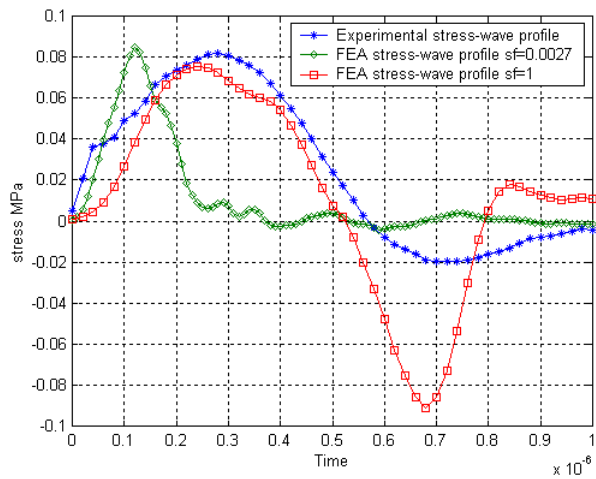


Figure 5.7 Experimental and FEA stress-wave profiles produced by impact of 0.4mm zirconia sphere to AISI 1020 steel at 21.5m/s

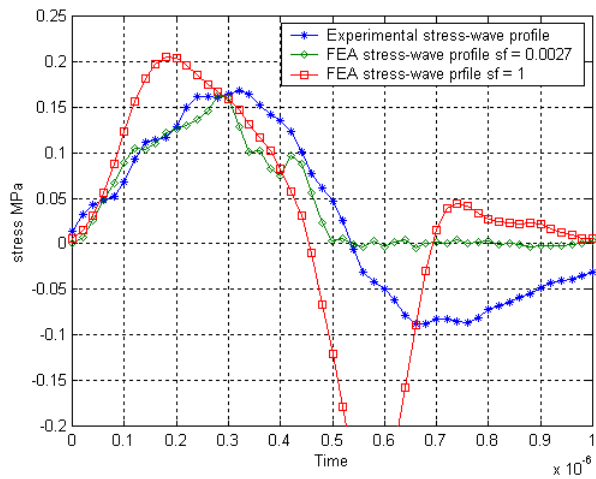


Figure 5.8 Experimental and FEA stress-wave profiles produced by impact of 0.4mm zirconia sphere to AISI 1020 steel at 52.5 m/s

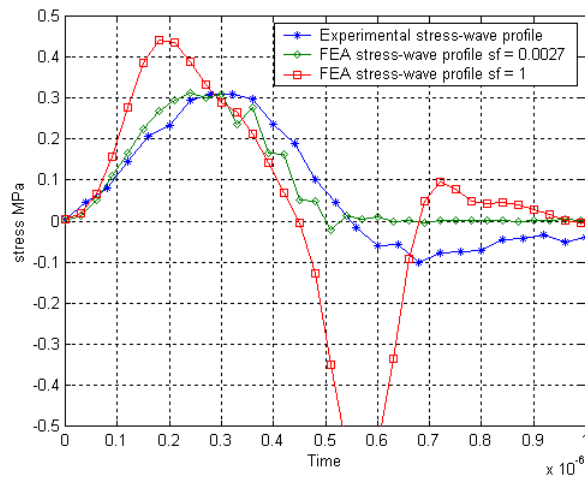


Figure 5.9 Experimental and FEA stress-wave profiles produced by impact of 0.4mm zirconia sphere to 1020 steel at 102 m/s

The main findings from the high velocity impact study are:

- The ISC model was shown to closely match the experimental stress-wave recordings in regards to phase and amplitude at the impact velocity of 21m/s
- A phase shift and amplitude reduction was evident for the experimental stress-wave recordings in comparison to the ISC model for the impact velocities of 52 and 104m/s. The result indicates a frequency dependant nature of the contact interface system, which has caused a phase shift and amplitude reduction to occur to the experimental stress-wave recordings. The phase shift may be related to a restriction of the transmission of tensile stresses across the contact interface under conditions of stress-wave frequencies above 0.9MHz.
- The CC model was in close agreement with experimental stress-wave recordings in regards to phase and amplitude for the impact velocities of 52 and 104m/s. The result indicates that the CC model worked effectively when the stress at the interface was above 0.15 MPa. The result indicates that the numerical instability problem of the LS DYNA contact algorithm, which was apparent in the CC model for the 2.5 and 21m/s impacts may be stress dependant.

Later in section 5.3, the impact and stress-wave monitoring study of two polymer materials is presented. As will be shown later, wave periods hence frequency of the experimental stress-wave recordings for the polymers are well above the wave

frequencies encountered in the AISI 1020 steel study. From the findings in this section, the much simpler ISC model could be justifiably implemented for the stress-wave study of the polymer materials.

The other important aspect of the high velocity impact and stress-wave study is the validation of key material property parameters of the Johnson-Cook material model. As shown in the higher velocity impact stress-wave recordings (at impact velocities 52 and 104m/s, figures 5.8 and 5.9) the close agreement between experimental and FEA results in regards to amplitude and phase indicated that input parameters of the FEA material model were consistent with the experimental results. As mentioned in section 5.2.1, material property parameters were derived from SHPB experiments of AISI 1006 steel conducted by the originators of the model, Johnson-Cook (1983). The next step in using the stress-wave monitoring technique for material model validation is to understand how the stress-wave characteristics may change when key material property parameters are changed.

5.2.5 Sensitivity study of FEA model parameters due to strain-rate effects

As discussed in section 3.2.2, when the FEA simulation for an elasto-plastic model at the surface was compared with a fully elastic model, the stress-wave profile for the elasto-plastic model, recorded at the piezo-electric transducer location showed evidence of wave dispersion. The result of the study showed that for the elasto-plastic model, as the stress-wave progressed through the plate, the wave characteristics changed, with the most noticeable effect being a broadening of wave profile and the shallowing of the wave rise-time, from zero stress to maximum amplitude. It was also considered that as a result of wave dispersion, the stress-waves initiated by elastic deformation at the surface would disperse (separate) from slower moving stress-waves initiated by plastic deformation of the surface. Following this assumption, the amplitude of the longitudinal stress-wave recorded at the piezo-electric transducer location should in fact scale to yield stress rather than the maximum flow stress at the surface, when an impact causing elasto-plastic deformation is considered. The parameter of the Johnson-Cook model, which will scale yield stress, can be shown from equation 2.13 to be the strain-rate parameter C .

In this section, the sensitivity of the strain-rate parameter to the amplitude of the stress-wave recording is considered. The study was conducted using 3 arbitrarily chosen values for the strain-rate parameter of 0.022, (as defined in the Johnson-Cook, 1983 study for AISI 1006 steel), 0.044 and 0.066. Other FEA material model values for the Johnson-Cook model were derived from tables 5.1 and 5.2. The FEA simulations were conducted for the highest impact velocity of 104m/s using the compliant contact model as defined in section 5.2.4. By using the highest impact velocity of 104m/s, the sensitivity of the strain-rate parameter C , should be more pronounced as a high impact velocity will cause high strain rates to occur.

The results of the study are shown in figures 5.10 to 5.12. As shown in figure 5.10 the main effect of increasing the strain-rate parameter C was to increase the amplitude of the FEA stress-wave recording. Figure 5.11 shows the von-Mises stress (see sections 5.2.9 for description of von-Mises stress) as a function of plastic strain obtained at the surface. As shown in the figure, yield stress is clearly defined at the onset of plastic deformation (i.e. at zero plastic strain). In figure 5.12, stress-wave amplitude (recorded at the rear face of the impacted plate) is plotted as a function of yield stress at the surface. As shown, a linear relationship exists between values for yield stress at the surface and stress-wave amplitude for each value of the strain-rate parameter C .

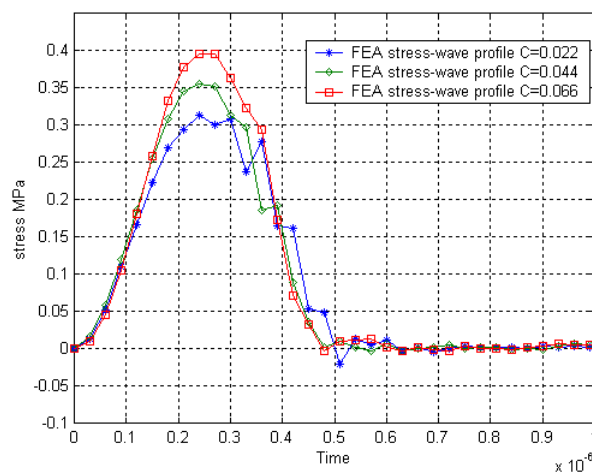


Figure 5.10 Stress-wave recordings from FEA simulations for different values of the strain-rate parameter C of the Johnson-Cook material model. FEA simulations based on impact to AISI 1020 steel at 104m/s by 0.4mm zirconia particle. Stress-wave recorded at the piezo-electric transducer location 10mm directly below the impact site

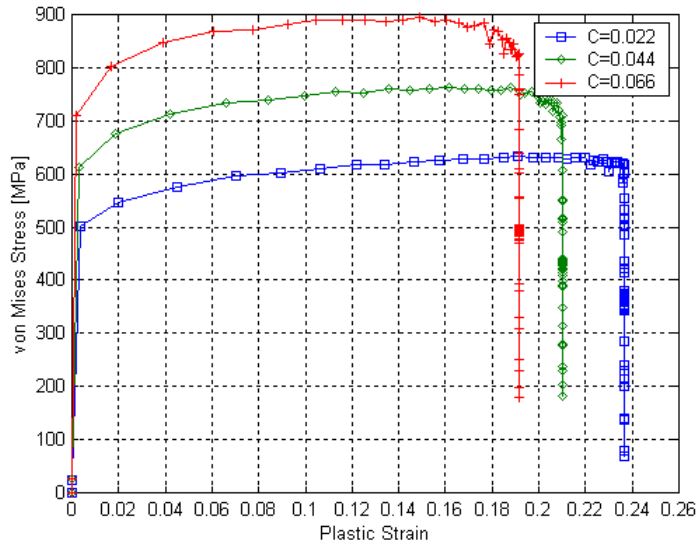


Figure 5.11 FEA model results of the deformed zone of the AISI 1020 steel wear surface showing von-Mises stress plotted as a function of plastic strain for varying values of the strain-rate parameter C of the Johnson-Cook material model. Impact produced by 0.4mm zirconia sphere at 104m/s

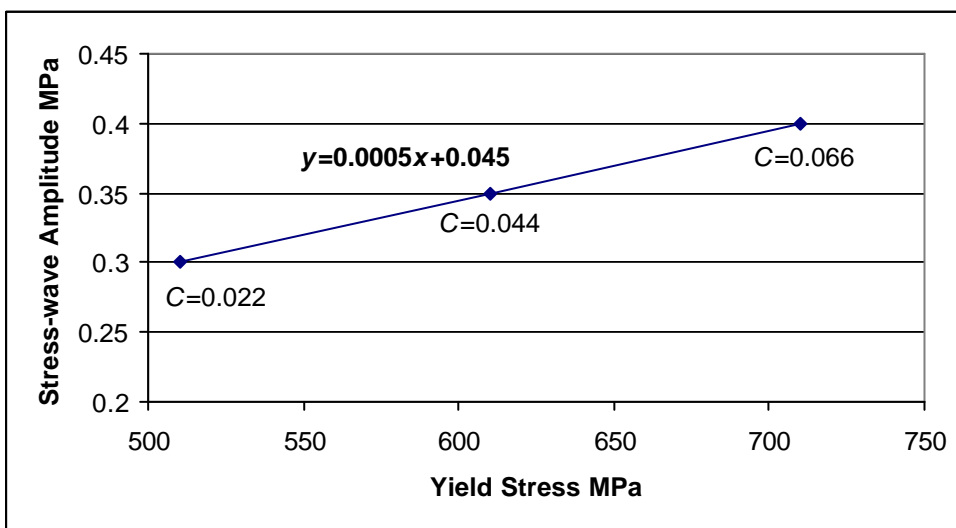


Figure 5.12 FEA model results showing stress-wave amplitude as a function of yield stress at the surface for various values of the strain rate parameter C of the Johnson-Cook material model. Impact to AISI 1020 steel at 104m/s by 0.4mm zirconia sphere

The main conclusions from the sensitivity study into the strain-rate parameter of the Johnson-Cook model are

1. The results confirm that for an elasto-plastic impact at the surface, the amplitude of the stress-wave recorded at the rear face scaled linearly to yield stress at the surface.
2. By comparing the amplitude of the experimental stress-wave recording with the FEA model prediction it is possible to validate the strain-rate parameter C of the Johnson-Cook material model.

5.2.6 Validation of Johnson-Cook model by impact crater study

As shown in the previous section, the stress-wave monitoring process was able to distinguish between different values for the strain-rate parameter C . As the stress-wave monitoring process developed in this study is a new process, it would be beneficial to validate the results by another method. One way to achieve this is to measure the extent of plastic deformation of the AISI 1020 steel wear surface, causing impact crater formation. Measurement of the experimental and the FEA model prediction of the impact crater depth will confirm if the flow stresses are similar. For the comparison study, the laser scanning confocal microscope was used to produce three-dimensional images of the impact craters of the AISI 1020 steel wear surface. Figure 5.13 shows a typical impact crater produced by an impact of a 0.4mm zirconia sphere to the AISI 1020 steel surface at 104m/s.

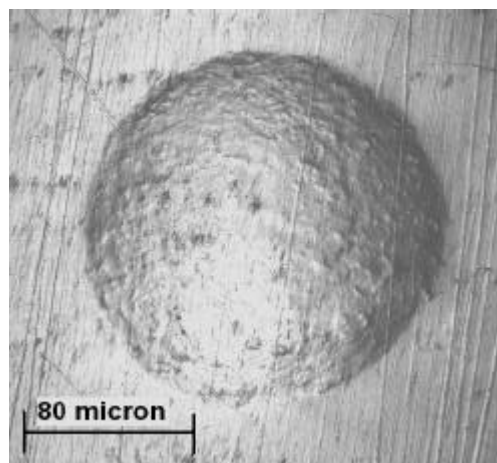


Figure 5.13 Impact crater produced by 0.4mm zirconia sphere impact at 104m/s, crater from experimental impact and stress-wave study of AISI 1020 steel

This page left intentionally blank

To obtain the crater depths for each impact velocity, the images of three individual impact craters were used and the average depth taken. Figure 5.14 shows typical 2-D crater profiles obtained from three individual impacts of the AISI 1020 steel wear surface for the impact velocity of 104m/s. As shown the impact craters were of similar dimensions, indicating that the experimental parameters were producing repeatable results.

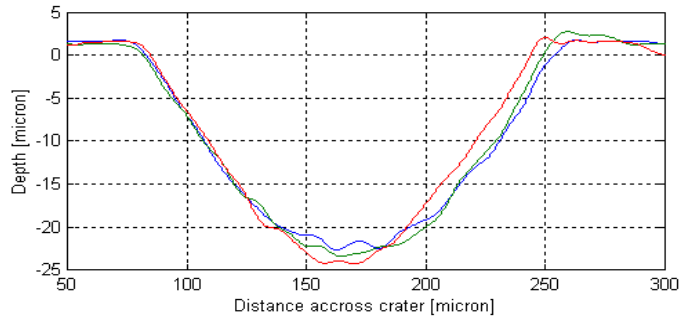


Figure 5.14 2-dimensional profile of impact craters produced by impacts of 0.4mm zirconia spheres to AISI 1020 steel at 104m/s derived from LSCM images

Figure 5.15 shows the comparison between the experimental impact crater depths and those obtained from the FEA model. As shown, good correlation was obtained for the value of 0.022 for the strain rate parameter C of the Johnson-Cook model. The impact crater study appears to confirm the results obtained from the stress-wave monitoring experiments (section 5.2.4) for the value of the strain-rate term of the Johnson-Cook model. The agreement of the stress-wave monitoring and the impact crater study also confirms that the parameters of the Johnson-Cook model relevant for plastic deformation, the strain-hardening terms B and n , and the thermal softening exponent b are in close agreement with the experiment.

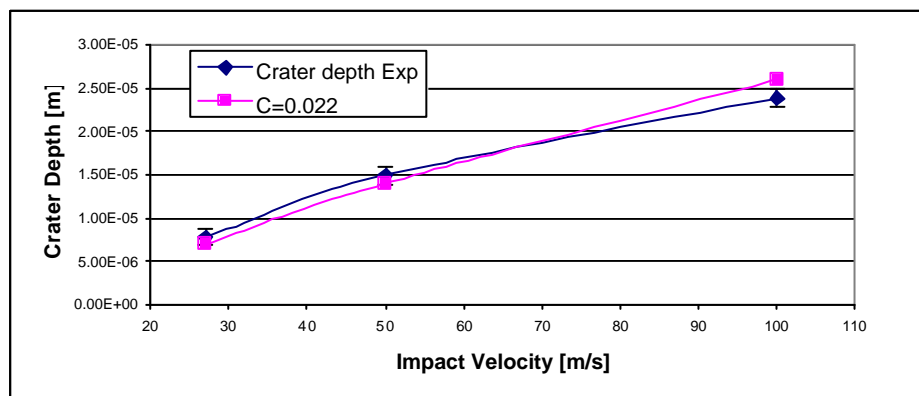


Figure 5.15 Experimental and FEA impact crater depths as a function of impact velocity

5.2.7 Sensitivity of strain-hardening terms under high strain impact conditions

As explained earlier in section 5.2.1, the strain-hardening terms of the Johnson-Cook model, B and n are generally obtained from low strain-rate experimental results. Often though, experimental results are not available to obtain these terms. In this section, a sensitivity study is described whose aim was to see how the stress-wave monitoring process could validate these terms. The sensitivity study was conducted by FEA method for impacts to the AISI 1020 steel surface for three different values of the strain-hardening parameter B , the exponent n was held constant for the study.

The value for B of 270MPa is the quasistatic value (as detailed in table 5.2) and the sensitivity study is carried out for double and half the quasistatic value (i.e. 540 and 135MPa respectively). As shown in figure 5.16, the sensitivity of the stress-wave amplitude to the three values of the strain-hardening parameter B was minor. The results confirm that it would be difficult to validate the strain-hardening parameter B by the stress-wave monitoring method. The result is not unexpected as it was confirmed in section 3.1.2 and section 5.2.5 that the amplitude of the longitudinal stress-wave recorded at the piezo-electric transducer location, scaled linearly with yield stress and not the flow stress at the surface.

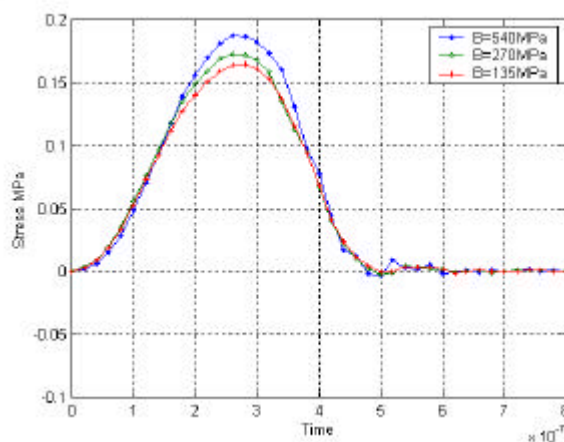


Figure 5.16 FEA sensitivity study of stress-wave produced by impact of 0.4mm zirconia sphere to AISI 1020 steel plate at 104m/s, using three different strain-hardening values for the Johnson-Cook model parameter, B .

5.2.8 Strain-rate of impacts extracted from FEA model

In this section, the plastic strain-rates from the impact and stress-wave monitoring study (section 5.2.4) of the AISI 1020 steel wear surface are determined from the FEA model. To accomplish this, an element from the FEA model was selected from an area of high plastic strain in the deformation zone. The plastic strain data for the element was then plotted as a function of time with an average slope being used to give the strain-rates as shown in figure 5.17. As shown the maximum strain-rate occurred for the impact at 104m/s.

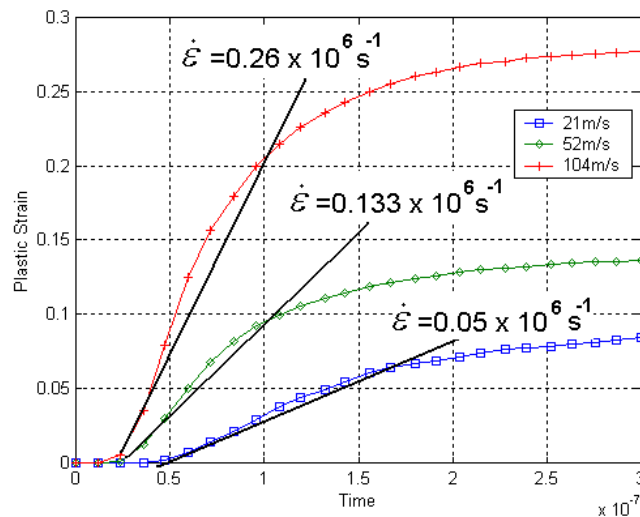


Figure 5.17 Calculated strain-rates for impact to AISI 1020 steel wear surface by 0.4mm zirconia spheres

5.2.9 Stress-strain curves related to stress-wave monitoring

In the study of erosion, it was shown in chapter 2, that yield and flow stress are major parameters in erosion models. However values for these parameters can change under high strain-rate impact conditions. In this section, yield and flow stress measurements of the AISI 1020 steel wear surface are extracted from the FEA method, which has been earlier validated by the stress-wave monitoring and impact crater study of sections 5.2.4 and 5.2.6.

Under impact conditions, the stress state at the surface can be complex due to plastic deformation, which in the case of AISI 1020 steel, is essentially caused by shear deformation. However, a stress analysis can be simplified by considering the von-Mises stress state, which encompasses the total stress state at the surface no matter how complex the stress state may be. The von-Mises criteria states that plastic flow will occur when the von-Mises stress surpasses the yield stress of the materials, where the von-Mises stress is defined as

$$s_{vm} = \left[\frac{(s_1 - s_2)^2 + (s_2 - s_3)^2 + (s_1 - s_3)^2}{2} \right]^{1/2} \quad (\text{Equation 2.11 reproduced})$$

where $s_{1,2,3}$ are the principal stresses. Therefore by plotting the von-Mises stress (also known as effective stress) as a function of plastic strain, the yield point, hence the yield stress of the material should be clearly defined on the stress-strain curve.

Figure 5.18 shows the von-Mises stress extracted from the impact zone of the FEA model. The figure shows the yield stress at 480 MPa for the impact velocities of 21 and 52m/s and 540 MPa at the impact velocity of 104m/s.

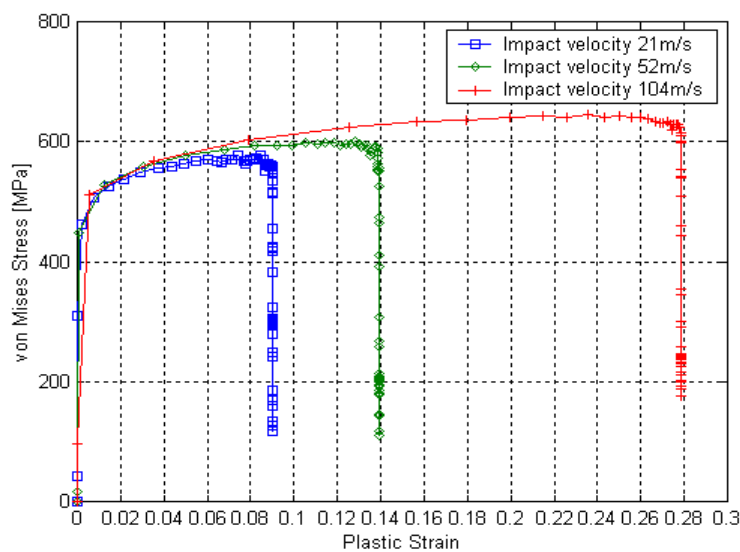


Figure 5.18 von-Mises stress as a function of plastic strain obtained from the FEA model validated by stress-wave monitoring process

In contrast, the quasistatic yield stress for AISI 1020 steel is 350 MPa. Flow stress (hardness) can be approximated as approximately 2.8 times the yield stress (see for instance Tabor, 1951). Using the Tabor approximation, gives the flow stress as approximately 1500MPa for the AISI 1020 steel wear surface at the highest impact velocity of 104m/s. By comparison, the quasistatic flow stress is approximately 1000MPa. The results show that an erosion model based on the quasistatic flow stress would be in error by a factor of at least 50%. This again confirms the relevance of obtaining material property parameters under conditions comparable to the erosive impact conditions.

5.3 Experimental and FEA study of impacts and stress-wave motion to polymer wear surfaces

5.3.1 Introduction

In this section, the stress-wave monitoring technique developed using AISI 1020 steel is applied for the study of ultra high molecular weight polyethylene (UHMWPE) and vinyl ester resin (VER). Over the years, polymer chemistry science has been used to develop the molecular structure of polymers to suit a wide variety of engineering applications. However the high strain-rate characteristics of polymers remains a relatively unexplored field of study.

UHMWPE is an extremely ductile thermoplastic polymer, which is widely used in abrasive wear applications. The polymer also possesses exceptional impact energy absorption qualities. In fact a 25mm thick slab can stop a 0.38 caliber bullet at a distance of 150mm (Stein in Engineering Plastics, 1988). Due to UHMWPE's inert nature and low wear, the polymer is also used extensively in the medical profession for components of knee and hip replacement (Bergstrom *et al* 2003). Wear behavior of UHMWPE for medical applications is however at relatively low strain-rates in comparison with erosive particle impact applications.

VER is a thermosetting polymer, which is widely used as a matrix binder for glass fibre reinforced composites. The polymer has excellent chemical resistance and is widely used when reinforced with glass fibres, as a structural composite material for chemical holding tanks. Other typical uses are for aircraft, automotive and marine applications. In contrast to the energy absorption qualities of UHMWPE, VER in comparison has low ultimate tensile strain to failure of 8% compared to UHMWPE's, 400%. Erosion and abrasive wear resistance of VER is relatively poor and for structural applications subjected to erosive conditions, the material would require a wear resistant lining to prolong the life of the structure. The impact and erosion study of VER will broaden the scope of the polymer study and show the contrasting trends when an impact resistant material such as UHMWPE is compared to the performance of VER.

The main aim of this section is to focus the stress-wave monitoring study to validating key material property parameters of the Johnson-Cook material model. Once validated, these material property parameters will be used to develop an erosion model, as will be detailed later in Chapter 6.

5.3.2 Implementation of the FEA material model

As with the AISI 1020 steel stress-wave study of section 5.2, a suitable yield criterion is needed to model the plastic deformation of polymers by the FEA method. Previous FEA studies of UHMWPE in the area of medical science (i.e. knee and hip applications) have shown the von-Mises yield criterion to be suitable (see for instance Bergstrom, 2003). The von-Mises criterion is also the yield criterion for the Johnson-Cook material model. However a literature search has failed to find any evidence of the Johnson-Cook model being applied to the study of polymers under high strain-rate impact conditions. Another factor, which may influence the yield criterion for polymers, is the effect of hydrostatic stress. Experiments have shown that ductile polymers do show some degree of sensitivity to hydrostatic stresses, causing increased hardness as strain-rates increased (Stein, 1988 and Dean *et al*, 2001). The yield criterion, which will effect plastic deformation of the polymer surface, remains an issue for investigation.

As shown in Chapter 2 (sections 2.2.2 and 2.2.4), similarities do exist between the high strain-rate loading of steel and ductile polymers, where the main effects are an increase in yield and flow stress as strain-rate is increased. Also, as explained in Chapter 2, the purpose of a material model is to model the perceived deformation characteristics of the material in question. The simplicity of the Johnson-Cook model (equation 2.13) in using scalar terms to model strain-rate and thermal softening effects makes the model appealing for polymer as well as metal impact studies. The application of the model for polymers may be justified considering the strain-rate and thermal softening similarities of steel and polymer materials as described in Chapter 2.

The first step for implementing the Johnson-Cook model for the FEA study of impacts to the polymer specimens is to obtain the strain-rate parameter C . However, little published information is currently available to accurately define a value for UHMWPE and VER. An initial estimate would therefore have to be made from previous studies of polymers subjected to high strain-rate conditions.

In Chapter 2 (section 2.2.4), split Hopkinson's pressure bar (SPHB) results were shown for studies by Buckley *et al* (2001) who tested thermosetting Bisphenol A epoxy resin at strain-rates up to $4.5 \times 10^3 \text{ s}^{-1}$ and results by Dean *et al* (2001) who tested thermoplastic propylene-ethylene copolymer (PEC) at strain-rates up to 93 s^{-1} . To obtain an initial estimate of the strain rate parameter C , a numerical study was conducted based on the stress relationship with strain-rate as shown in the studies by Buckley and by Dean *et al*. Figure 5.22 shows the linear relationship when the ratio of the dynamic flow stress to quasistatic flow stress ($\mathbf{s}_{df} / \mathbf{s}_f$) is plotted as a function of the natural log of strain-rate. The slope of the curves defines the strain-rate parameter C in the Johnson-Cook model. The values obtained were 0.06 (Buckley) and 0.08 (Dean *et al*). Since such a close agreement existed it was decided to use an average value of 0.07 for the polymers, as a starting point for the FEA stress-wave study.

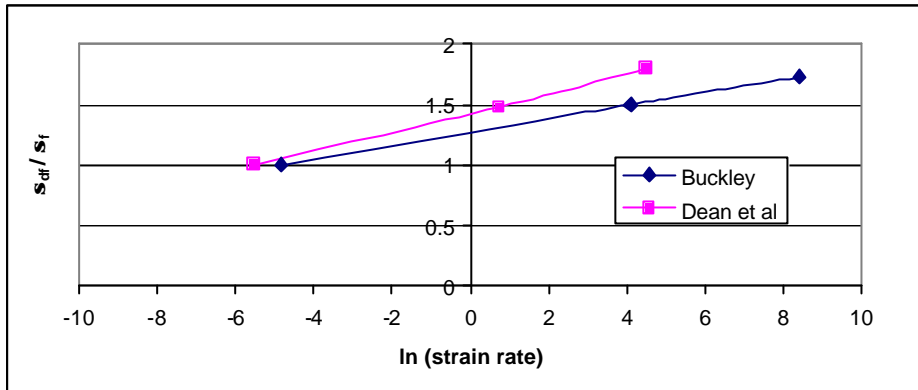


Figure 5.22 Estimate of the strain-rate parameter to be used for the polymer FEA study. Values of the ratio of dynamic flow stress to quasistatic flow stress (s_{df} / s_f) and strain-rates obtained from figures 2.9 and 2.10 in Chapter 2

An initial estimate would also have to be made for the strain-hardening parameters, B and n . Strain-hardening values were derived by *curve fitting* of the quasistatic stress-strain curves obtained from the study by Dean *et al*, for PEC as defined in figure 2.9 (section 2.2.4). The equation used to plot stress as a function of plastic strain, to derive values for B and n , were taken from the first bracket set of the Johnson-Cook model (equation 2.13) i.e.

$$\mathbf{s}(\mathbf{e}_p) = [A + B\mathbf{e}_p^n] \quad (5.1)$$

Figure 5.23 shows the results of the curve fitting exercise to obtain values for B and n . As shown close agreement was obtained for values of B and n of 30MPa and 0.36 respectively.

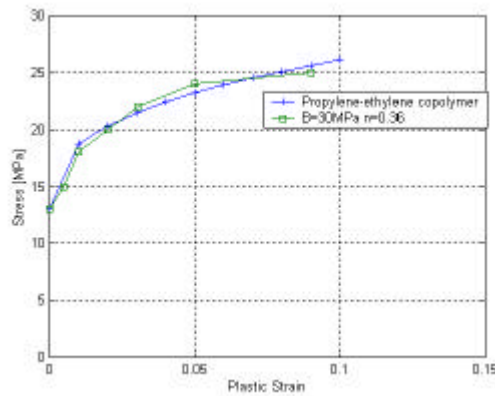


Figure 5.23 Estimate of Johnson-Cook model strain-hardening parameters B and n obtained from curve fitting of quasistatic stress-strain curve of propylene-ethylene copolymer as defined in the study by Dean *et al* (2001)

The shear modulus and bulk modulus needed for the FEA model were obtained using the following expressions commonly used for the mechanics of elastic materials (see for instance Beer and Johnston, 1992)

$$G = \frac{E}{2(1+\nu)} \quad (5.2)$$

$$B_m = \frac{E}{3(1-2\nu)} \quad (5.3)$$

Table 5.3 and 5.4 summarizes the material properties used for the FEA simulations.

Table 5.3 Elastic and thermal material property parameters used for the FEA model. Appendix C contains manufacturers material specifications

Material	E GPa	G GPa	ρ kg/m ³	ν Poisson's ratio	Specific heat J/kg K	Thermal Conductivity W/mK
UHMWPE	0.82	0.26	930	0.43	1800	0.12
VER	4.46	1.63	1070	0.36	1800	0.12
PIC 151 piezo- electric	54		7800	0.28		
Zirconia spheres	134		3990	0.26	280	21

Table 5.4 Johnson-Cook material model parameters for the FEA model. Appendix C contains manufacturers material specifications

Material	A MPa	B MPa	n	C	T_{room} Deg C	T_{melt} Deg C	b	B_m GPa
UHMWPE	21	30	0.36	0.07	25	140	1	1.9
VER	90	30	0.36	0.07	25	140	1	5.3

5.3.3 Specimen manufacture

UHMWPE was available from the manufacturer in standard sheet form of 10mm thickness [†]. VER was available from the manufacturer in liquid resin form^{††}. The VER specimens were manufactured by mixing the liquid resin with the manufacturers recommended amount of catalyst agents and then pouring the mixture into an open mould, which was then allowed to cure at ambient temperature. The specimens were then post cured at 80⁰C for 2 hours in a convection oven. All specimens were cut to rectangular blocks of 30 x 35mm. The specimens were then polished using silicon carbide abrasive paper (up to 2000 grit size) until a smooth flat finish was obtained.

5.3.4 High velocity impact and FEA modelling of polymer materials

In this section, stress-wave recordings obtained from the high velocity impact experiments are compared with the FEA model predictions for the polymer wear materials. The amplitudes of the experimental stress-wave have been scaled by the scaling factor of 6.1 as described in sections 3.3.7 and confirmed in the low velocity impact study of section 5.2.2. The FEA simulations were conducted on the basis of the ideally stiff contact model (ISC model), which is designed to model the contact between the piezo-electric transducer and the wear material. The ISC model type was confirmed as the correct contact model to be used when the stress-wave frequency was below 0.9MHz, as confirmed in the stress-wave monitoring study of the AISI 1020 steel, section 5.2.4. As will be shown for the polymer impacts, the stress-wave frequencies are well below 0.9MHz frequency.

The experimental stress-waves shown represent the average of six individual stress-wave recordings. As shown in the AISI 1020 steel stress-wave study, the highest impact velocity of 104m/s showed the highest sensitivity for the strain-rate parameter *C* of the Johnson-Cook material model.

[†] UHMWPE brand name Tivar 1000, manufactured by Poly Hi-Solidur, see Appendix C

^{††} VER brand name Derakane 441-400, manufactured by Dow plastics, see Appendix C

In this section, stress-wave comparisons between experiment and FEA model predictions are conducted for the impact velocity of 104m/s only. This approach was adopted to reduce computational time, as the 104m/s impact velocity will show greatest sensitivity to the strain-rate parameter than lower impact velocities.

Figure 5.24 shows the waveform comparison for the UHMWPE specimen. The closest match between experimental and FEA stress-wave amplitude was obtained when the strain-rate parameter was 0.07. It was however noted, that the amplitudes of the stress-waves derived from the FEA simulations showed low sensitivity to changing values of the strain-rate parameter C as shown in figure 5.25, which shows the results of a sensitivity study for strain-rate parameter values of 0.04, 0.08 and 0.120. The result is not unexpected as the yield stress of UHMWPE is relatively low at 21MPa. The stress-wave amplitude would be more sensitive to the strain-rate parameter for materials with higher values of yield stress, as shown in the AISI 1020 steel study of section 5.2.4.

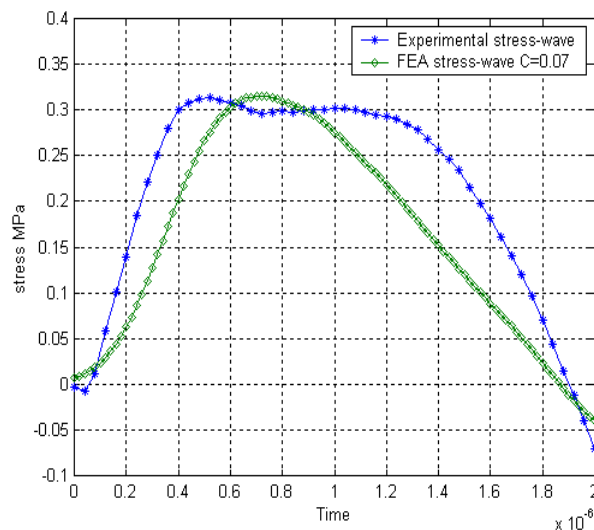


Figure 5.24 FEA model and experimental stress-waves produced by impact of 0.4mm zirconia sphere to UHMWPE at 104m/s, stress-waves recorded at piezo-electric transducer location at rear face of 10mm specimen

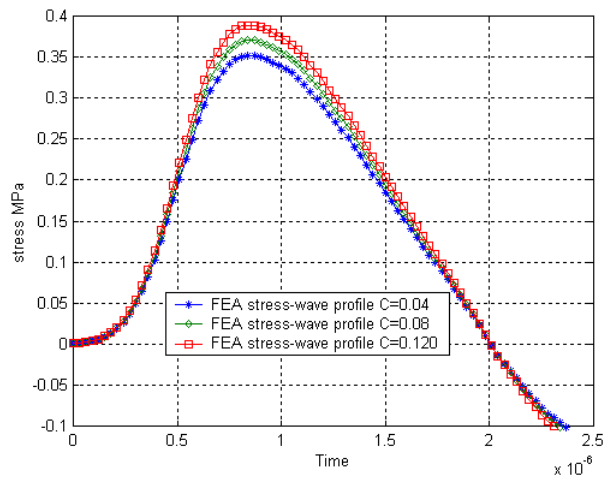


Figure 5.25 FEA model sensitivity study for various values of the strain-rate parameter C of the Johnson-Cook material model, stress-waves recorded at piezo-electric transducer location at rear face of 10mm thick wear material model, impacted by 0.4mm zirconia sphere impacting UHMWPE at 104m/s

Figure 5.26 shows the FEA model and stress-wave recording for the VER impact and stress-wave study. As shown, the closest agreement between the FEA model and experimental result was for the strain-rate parameter value of 0.140. This value is twice the original estimated value of 0.07 and indicates that the yield stress of VER must have increased substantially due to strain rate effects. In the next section, microscope images of the wear surface are shown for each polymer specimen. The images will be used to gauge the amount of plastic deformation, which has occurred to the wear surfaces.

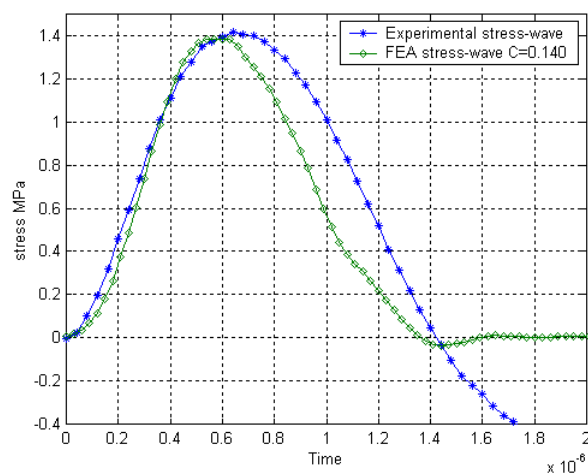


Figure 5.26 FEA model and experimental stress-waves produced by impact of 0.4mm zirconia sphere to VER at 104m/s, stress-waves recorded at piezo-electric transducer location at rear face of the 7mm thick specimen

5.3.5 Impact crater study

In the previous section, close agreement was obtained between the experimental and FEA stress-wave amplitudes for the strain-rate parameter values of 0.07 for UHMWPE and 0.140 for VER. As shown in the AISI 1020 steel stress-wave study the stress-wave amplitude can be related to the elastic stress component of the impact at the surface, which defines the yield stress of the wear surface. As shown in the AISI 1020 steel study, the other parameters of the Johnson-Cook material model relating to plastic deformation can be validated by microscope inspection of the impact craters left on the wear surface.

Figure 5.27 shows an LSCM image of a typical impact crater of the UHMWPE wear surface for the impact velocity of 104m/s. The average depths of three impact craters were measured by taking cross section profiles and were shown to be 33 μm . By comparison, the impact crater depth obtained from the FEA model was 120 μm , which is almost four times the experimental crater depth. The result indicates that the UHMWPE wear surface was considerably harder than the FEA model prediction.

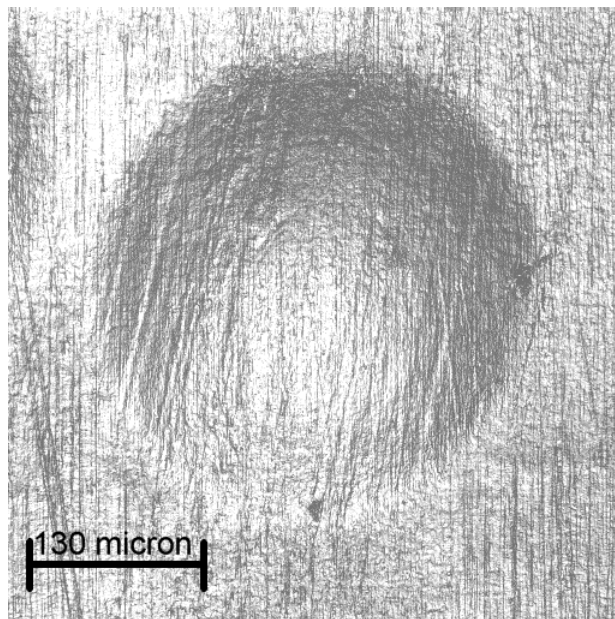


Figure 5.27 Impact crater of UHMWPE produced by impact of 0.4mm zirconia sphere at 104m/s

This page left intentionally blank

Remarkably, there was little evidence of plastic deformation of the VER wear surface as shown in the LSCM image of figure 5.28. The image clearly shows the imprints left by the impacting particle on the wear surface, however the wear surface showed little if any signs of crater formation indicating that the impacts were predominantly elastic. The main conclusion to be drawn from the VER wear surface study is the yield strength of the material must have increased significantly and this was also evident by the stress-wave study, which showed the strain-rate parameter C , which essentially scales the dynamic yield stress, was double that of the original estimated value of 0.07.

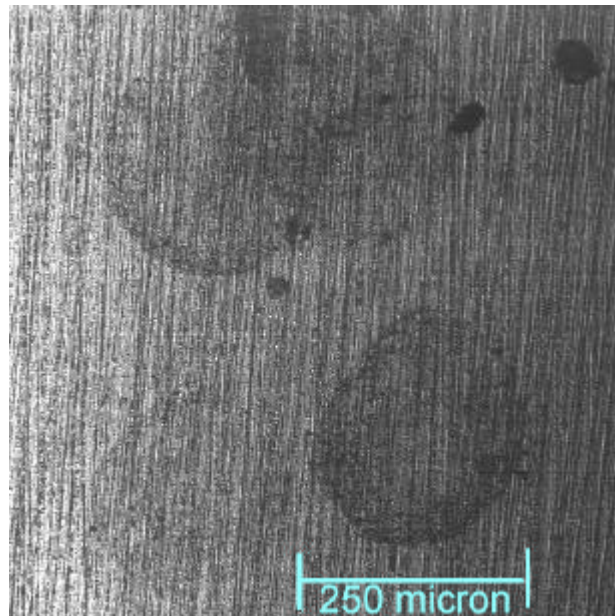


Figure 5.28 Imprints left on VER wear surface produced by impacts of 0.4mm zirconia sphere at 104m/s

A possible explanation for the large increase in hardness of both polymers is the effect of the hydrostatic stress. As described in Chapter 2 (section 2.2.3) the yield criterion for polymers is the von-Mises stress with the additive term of the hydrostatic stress component, as defined in equation 2.16

$$\mathbf{s} = \mathbf{s}_{vm} + h\mathbf{s}_m \quad (\text{Equation 2.16 reproduced})$$

This page left intentionally blank

where n describes the sensitivity of the polymer to hydrostatic stress. The effect of the hydrostatic stress component is to increase hardness and to also enhance the transition from ductile to brittle nature. The effects of hydrostatic stress can be explained in simple physical terms as follows: The plastic flow, which would normally occur by shear deformation at low strain-rates, is constrained as a result of high strain-rate loading. The deformation process can be likened to a granular material where individual particles must climb over one another to sustain relative shear, this causes volumetric dilatation (expansion) to occur, further constraining the material. In the case of polymers, it is the molecular chain structure in which shear deformation can only occur if the molecules can slip past one another. The impact study of UHMWPE and VER showed that each material exhibited a significant increase in yield stress under high strain-rate conditions. Although no surface cracking was evident in each polymer, the results indicate strain-rate effects were causing an increase to hardness (I.e. strain-hardening). With the increased hardness, ductility will naturally become lower and a trend towards brittle wear mechanisms becoming more evident. The strain-rate effects of the polymers is a significant discovery, particularly for the study of erosion, as a trend towards ductile to brittle transition will cause wear mechanisms to shift from plastic deformation to fracture and crack propagation.

The next step is to be able to model the hardening effects caused by the hydrostatic stress component. The hydrostatic stress component causing an increase in hardness could be accounted for by simply increasing the strain-hardening terms of the Johnson-Cook model. This approach could be justified as described earlier in section 2.2.1; an FEA model is designed to model the perceived deformation characteristics of the material in question. In this case the perceived effect of the hydrostatic stress term is to increase hardness as a result of strain and strain-rate effects. In the next section, the issues relating to strain-hardening of the polymer wear surfaces are discussed.

5.3.6 Stress-strain curve obtained from FEA model

To model the hardening effect of the polymers, it would be required to increase the value of the strain-hardening term, B of the Johnson-Cook model until the plastic deformation of the FEA model showed similar values as the experimental result. A sensitivity study was carried out on a number of FEA simulations until the impact crater depth of the FEA model closely matched the experimental impact crater depths. After several iterations, the final value for B for UHMWPE and VER was shown to be 120MPa and 150MPa respectively. In comparison, the initial estimated value for B , obtained under quasistatic conditions was 30MPa.

Figure 5.29 shows the von-Mises stress as a function of plastic strain for UHMWPE obtained from the FEA simulations. As shown, the yield point is clearly defined at the yield stress of 60MPa. The yield stress value corresponds to more than double the quasistatic yield stress of 21MPa, which is the value for A in the Johnson-Cook model. The effect of strain-hardening (using the revised value for B of 120MPa) is clearly evident by the steeper rise in flow stress in comparison with the original stress-strain curve using the original estimated value for the strain-hardening parameter B (i.e. 30MPa). The transition from ductile to brittle nature is clearly evident by lower plastic strain and increased flow stress.

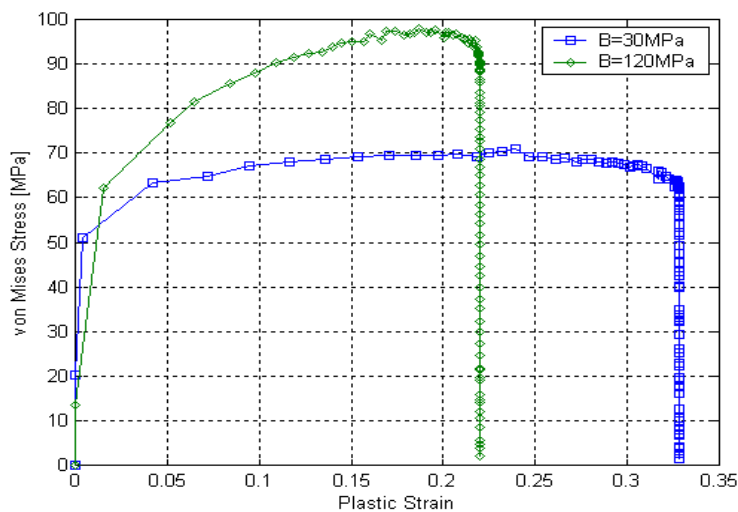


Figure 5.29 Stress-strain curves showing strain-hardening effects of UHMWPE for the impact velocity of 104m/s, the blue line (square markers) represents the initial estimate for the strain rate parameter B , the green line (diamond markers) represents the revised value

Figure 5.30 shows the stress-strain curves for the VER wear surface. The initial estimate values of C and B of the Johnson-Cook model were 0.07 and 30MPa respectively and are shown along with the revised values for C and B of 0.140 and 150MPa. As shown the yield stress is nearly 2.5 times higher (250MPa) than the quasistatic value of 90MPa, which is the value of A in the Johnson-Cook model. The maximum strain is a fraction under 10% for the revised model values, which is slightly higher than the ultimate tensile strain of VER of 8%, obtained under quasistatic tensile loading conditions. The impacts would therefore be close to the fracture limit of the material. The strain-rates of the impact were estimated by the procedure applied in section 5.2.7 and were found to be approximately $0.18 \times 10^6 \text{s}^{-1}$ for the both polymer specimens.

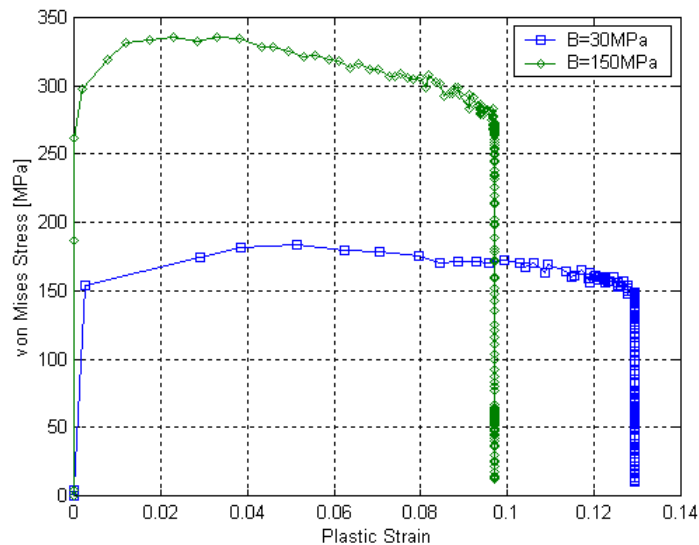


Figure 5.30 Stress-strain curves of VER for the impact velocity of 104m/s, the blue line (square markers) represents the initial estimate with Johnson-Cook material model parameters $C = 0.07$ and $B = 30\text{MPa}$ and the red line (diamond markers) $C = 0.140$, $B = 150\text{MPa}$

5.4 Chapter summary

In the first section of this Chapter, the stress-wave monitoring process was developed using the well-recognized deformation characteristics of AISI 1020 steel as the model material. The low velocity impact experiment was designed to study the stress-wave signature and compare the transducer response with FEA results.

Stress-wave recordings were obtained from the FEA model for two contact models; an ideally stiff contact model (ISC model) and a compliant contact model (CC model). The contact models were implemented as it was unclear how the contact interface may effects the transmitted stress-wave. The ISC model assumes the contact interface is ideally stiff. The CC model assumes some compliance at the interface and the basis for implementing the CC model was to model either asperity contact or hydrodynamic lubrication effects from the oil-coupling medium. The results of the low velocity impact study showed the ISC model could be used to model the experimental system.

Higher velocity impacts at 21, 52 and 104m/s were then conducted with the AISI 1020 steel specimen and modelled by FEA using the ISC and CC models. The results showed that at the impact velocity of 21m/s, the ISC model was in phase with the experimental stress-wave, however at the higher impact velocities of 52 and 104m/s the ISC model was no longer in phase with experimental results. The study showed a frequency dependant limit might have been reached for the experimental stress-waves to be in phase with the ISC model. It is more likely that the phase transition for the impact velocities at 52 and 104m/s is related to the high frequency of the stress-wave and the inability of the oil-coupling medium to transmit tensile stresses at such a frequency. It was noted that the ISC model was in phase with experimental recordings when the stress-wave frequency was below approximately 0.9MHz. It was shown that the scaling factor for the penalty stiffness parameter of the CC model was unusually low. It was concluded that the poor agreement with experimental results for the CC model at the impact velocities of 2.5 and 21m/s might have been related to low stress levels at the contact interface. The ambiguous results of the CC model for the low velocity impacts indicated that some form of numerical instability was evident when stress levels are low at the contact interface.

The FEA analysis was conducted using the Johnson-Cook material model. As the numbers of parameters in the model are numerous, it was decided to concentrate on the parameters of the model that relate to strain-rate effects. These were the strain-rate term C and the thermal exponent b . These parameters were obtained from published experimental results at strain-rates up to 10^2s^{-1} . When the experimental stress-waves were compared with the FEA model result, it was shown that a close agreement in stress-wave amplitude and period existed when the strain-rate parameter C was 0.022, which coincided with the result for AISI 1006 steel obtained from the original authors of the model, Johnson and Cook (1983).

An FEA sensitivity study was conducted on the strain rate parameter C of the Johnson-Cook model to see the effect this would have on the stress-wave amplitude. As theorised in section 3.2.2, it was proposed that the yield stress at the surface would scale with the amplitude of the recorded stress-wave. The reasoning was that wave dispersion would cause elastic waves to separate from slower moving plastic waves. The result of the study showed that in fact a linear relationship existed between the stress-wave amplitude and the yield stress at the surface. The result was a significant find as it was possible to validate the strain-rate parameter C of the Johnson-Cook model by the stress-wave monitoring method.

Validation of the stress-wave monitoring process was accomplished by measurement of the impact craters of the AISI 1020 steel wear surface. The impact crater comparison study showed that the best fit with the experimental crater depths was obtained when the strain-rate parameter C was 0.022 and the thermal softening term b equal to unity. The results were in agreement with the stress-wave monitoring results and appeared to strengthen the stress-wave monitoring process as a valuable tool for validating key material property parameters.

An FEA sensitivity study was then conducted to view the effects of the terms of the Johnson-Cook model relevant for plastic deformation of the surface. The strain-hardening parameter B was the subject of the study. It was shown that there was little effect to the stress-wave amplitude when the value of B was double or half the original value of 270MPa. The results of the sensitivity study were not unexpected as the stress-wave amplitude was shown to be representative of the elastic stress component of the

impact event at the surface. The plastic component of the impact, defining the flow stress at the surface, is transmitted at a lower wave speed velocity than elastic waves and thus would be dispersed or even dissipated within the material.

It was shown in the following section that the maximum strain-rate of the impacts to the AISI 1020 steel wear surface was in the order of $0.22 \times 10^6 \text{ s}^{-1}$. The strain-rate value was at least two orders of magnitude above conventional SHPB method, again realizing the potential for the development of the stress-wave monitoring process for the study of materials under high strain-rate, erosive impact conditions.

In the following section, the emphasis was centred on gaining surface information for the study of erosion. The von-Mises stress was obtained from the FEA model at the highly stressed impact zone. The stress analysis enabled an accurate indication of the yield stress to be obtained. As shown the yield stress for AISI 1020 steel was 550MPa at the highest impact velocity, which was approximately 1.5 times higher than the quasistatic value of 350MPa. The maximum flow stress at the surface could be approximated as 2.8 times the yield stress, giving a value of 1500Mpa for AISI 1020 steel at the highest strain-rate. As described in chapter 2, yield stress and flow stress are major parameters of the erosion models presented. The increase of flow stress as shown in this section would leave some doubt as to the relevance of an erosion model which relied solely on quasistatic yield or flow stress measurement.

The last section of this Chapter was devoted to the impact study of ultra high molecular weight polyethylene (UHMWPE) and vinyl ester resin (VER). The stress-wave monitoring procedure developed using AISI 1020 steel was adopted for the study of the polymer specimens. The Johnson-Cook model was again implemented for the FEA analysis. However, with little published literature of UHMWPE and VER available for high strain-rate loading conditions, it was required to estimate values for model parameters from published experimental results of similar polymers. The stress-wave monitoring experiments showed the strain-rate parameter C to be 0.07 for UHMWPE and the value for VER to be 0.140. The study of the impact craters showed the experimental crater depths to be much less than the FEA model prediction for the UHMWPE specimen. Remarkably, the VER wear surface showed very little signs of plastic deformation, however imprints were left on the surface showing the area of

particle / wear surface contact. The conclusion from the analysis indicated that the hydrostatic stress component appeared to be increasing the hardness of both polymer wear surface. The Johnson-Cook material model contains parameters relevant for strain-hardening and a FEA sensitivity study was conducted by increasing the strain-hardening parameter B , until the FEA model gave similar impact crater depths as the experimental result. The strain-hardening term was shown to increase by at least a factor of four for both polymers, to 120MPa for UHMWPE and 150MPa for VER, compared to initial estimates obtained from high strain-rate SHPB experiments. The main conclusion to be drawn from the polymer study is the sensitivity of the materials to strain-hardening effects causing ductile to brittle transition.

This page left intentionally blank

CHAPTER 6

EROSION MODELLING

6.1 Introduction

The results obtained from the stress-wave monitoring sections have shown that it is possible to characterize steel and polymer material properties at strain-rates typical of erosive impact conditions. It was shown that material response, especially for the polymer materials, changed dramatically as strain-rate increased. As noted, the polymers became much harder, as strain-rates increased. In the stress-wave monitoring sections, normal impacts by spherical particles were considered. The purpose of using spherical particles was to develop the stress-wave monitoring process for an impact situation, which could be readily modelled by the FEA method.

As detailed in Chapter 1, erosion of ductile metals and polymers occurs more predominantly for oblique impacts by angular particles. As explained, an oblique angled impact can result in very higher surface strains as the particle digs into the ductile wear surface. Erosion of ductile wear materials as a result of oblique angled impacts occurs more predominantly by micro ploughing and micro cutting mechanisms. To develop a thorough understanding of the erosion process, oblique angled impacts would have to be considered. Again FEA is a valuable tool to obtain detailed surface information, which would otherwise be difficult or impossible to obtain experimentally. The stress-wave study of Chapter 5 paved the way for obtaining FEA material property parameters at strain-rates typical of an erosive particle impact event. After the FEA material model is validated, a range of impact angles and particle geometry could be studied by the FEA method.

In this Chapter, results from the stress-wave monitoring sections are used for the FEA study of erosive particle impact events. The study involved the use of a solid FEA model with angular particle geometry and particle impact trajectory of 45-degrees to the

wear surface. The FEA simulations represent experimental conditions used for erosion testing of the AISI 1020 steel and polymer specimens. The results from the FEA simulations are used to develop an improved version of the Ratner-Lancaster model, which will take into account strain, strain-rate and thermal effects.

6.2 Stress-wave monitoring results applied for the study of erosion

6.2.1 Energy based approach to erosion

As presented in Chapter 2, the Ratner-Lancaster model is widely accepted as a suitable wear model for polymeric materials (Ratner *et al* 1967 and Lancaster 1969). It has also been applied with good success for the erosion study of heat-treated steels (O'Flynn *et al*, 2001). The Ratner-Lancaster model is simple in form and predicts erosion to be proportional to the inverse of the area under the stress-strain curve, which is estimated by the inverse product of the ultimate stress and ultimate strain

$$W \propto \frac{1}{\mathbf{s}_u \mathbf{e}_u} \quad (\text{Equation 2.6 reproduced})$$

where the product of the ultimate stress and ultimate strain is the approximation of the deformation energy capacity of the material. When the kinetic energy of the impacting particle is considered, the Ratner-Lancaster model can be written in the form

$$W = \frac{kmV^2}{2} \frac{1}{\mathbf{s}_u \mathbf{e}_u} \quad (6.1)$$

where k is a constant, describing the extent of material removal by a number of impacting particles, m is the mass and V the velocity of the impacting particles. The energy based approach for erosion modelling appears simple in form and easy to apply.

However, as explained in the introduction of this thesis (Chapter 1), past erosion studies have essentially based deformation energy capacity on quasistatic (or low strain-rate) values of ultimate stress and ultimate strain. In the previous Chapter, evidence was presented to show that the materials of interest in this study have deformation characteristics that are very strain-rate dependent.

Typically, impacts causing erosion of a ductile wear surface occur at oblique angles and by angular particles. The stress-wave monitoring approach was shown to be able to validate material property parameters, typical of the strain-rates occurring for erosive particle impact events. However, the plastic strain from the normal impact of a sphere with the wear surface, as used in the stress-wave monitoring experiments would be substantially less than for an angular particle impact. Increased plastic strain will also result in increased localised temperatures in the deformation zone. A more precise approach for the study of erosion would be to obtain deformation capacity in the highly strained deformation zone, which will be a function of strain, strain-rate and temperature. An improved version of the Ratner-Lancaster model could then be defined as

$$W = \frac{k m V^2}{2} \frac{1}{E_{def}} \quad (6.2)$$

where E_{def} is the deformation energy capacity of the wear material in the deformation zone. The deformation zone could be described as the region of material, which is undergoing significant plastic deformation at high strain-rates. In Chapter 1 (section 1.1.2), the deformation zone was described by a simplistic model (see for instance, Shewmon *et al* 1983). As described in Chapter 1, the plastic deformation of the wear surface as a result of an oblique particle impact could be modelled as two regions, where plastic deformation in each region is likely to be high or low (see figure 6.1, reproduced from Chapter 1, figure 1.5)

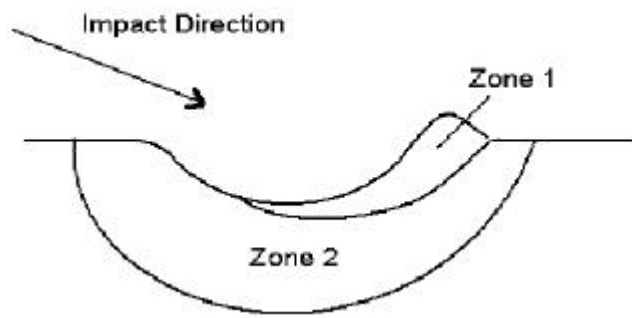


Figure 6.1 (reproduced from Chapter 1, figure 1.5) Schematic cross-section of oblique impact crater. Zone 1 is the region most likely to have a high level of dynamic shear deformation, zone 2 the region of lower strain-rate compression. After Shewmon *et al* (1983).

As described in Chapter 1, the region of zone 2 occurred deeper below the wear surface and as a consequence plastic deformation is more likely to be constrained by surrounding bulk material. The plastic deformation in the region of zone 2 is also more likely to occur at lower strain-rate than the region of zone 1. The region of zone 1 is the region of material close to the surface and is the region of interest for erosion studies. In zone 1, the material will be less constrained by surrounding bulk material and will therefore undergo much high shear deformation. The material in zone 1 will also be subjected to high-localised temperatures. Raised lip formations may also occur and as described in Chapter 1, lip formation is a precursor mechanism for the erosion process, as multiple particle impacts on or near the lip area can result in the lip volume being removed. It is evident that to model erosion more effectively, the material properties in the region of zone 1, close to the surface, should be accurately defined.

Again the Johnson-Cook model appears ideally suited to estimate the deformation energy capacity of the wear surface in the region of zone 1. Other FEA material models could also be applied if they have similar model characteristics. For the current study however, the Johnson-Cook model is used to obtain the deformation energy capacity for each material in the region (i.e. zone 1) close to the surface. Deformation energy capacity of the wear materials was obtained in the study by numerical integration of the stress-strain curve from the limits of zero plastic strain until the ultimate strain to failure of the wear material, as defined in equation 6.3 below

$$E_{def} = \int_0^{e_u} [A + B e^n][1 + C \ln \dot{e}][1 - T^{*b}] d\mathbf{e} \quad (6.3)$$

where e_u is the ultimate strain to failure of the material. The parameter values needed to define the deformation energy capacity of the wear material are; A , B , C and n which are derived from the stress-wave monitoring sections of Chapter 5. The remaining values needed are the strain-rate \dot{e} and the homologous temperature T^* (equation 2.15) in the region of zone 1 of the wear surface, and these values can be obtained directly from the FEA simulations of oblique particle impacts, which will be described in section 6.2.2.

When defining deformation energy capacity for the wear material (equation 6.3), deformation energy capacity should not be confused with the area under the stress strain curve in the deformation zone, for a particular impact event. Rather, the aim is determine the deformation energy capacity of the wear material at the limits of ultimate failure strain e_u using values for strain-rate and temperature obtained from the FEA model. The ultimate failure strain e_u will also be a function of strain-rate and thermal effects. As shown in the stress-wave monitoring study of Chapter 5, the polymer materials showed evidence of significant strain-hardening, as a result of strain-rate effects. In the next section, a discussion is presented to estimate the value of the ultimate failure strain required for the deformation energy calculations of equation 6.3.

6.2.2 Development of FEA solid model for the study of erosive impacts

Typically, the erosion rate of AISI 1020 steel occurs greatest between 20° and 30° (Finnie, 1960) and for UHMWPE $30-45^\circ$ (Wang *et al* 1998). To model erosive impact events by the FEA method, the axisymmetric model of the normal impact of a sphere with the wear surface, as used in the stress-wave monitoring sections 5.2 and 5.3, would not be suitable. A solid FEA model having angular particle contact geometry would therefore have to be developed. The important consideration for the FEA modelling process is that once the FEA material model is validated the need to model stress-wave activity would not be necessary. By not having to track stress-wave activity, it allows the solid FEA model to be scaled down in through thickness and lateral dimensions.

Figure 6.2 shows the FEA model developed for the erosion study. As shown, the particle geometry allows the leading edge of the impacting particle to penetrate deeply into the wear surface and provide strains typical of angular particle impact events. Oblique angled impacts were conducted at the 45-degree impact trajectory to model erosion testing conditions detailed later in section 6.2.3. During erosion testing, a range of contact angles of the particles leading edges with the wear surface is possible. The FEA model therefore represents an approximation of possible particle leading edge contact angles. The FEA model shown in figure 6.2 would represent severe impact and erosion conditions by angular particles and an upper boundary for wear surface deformation.

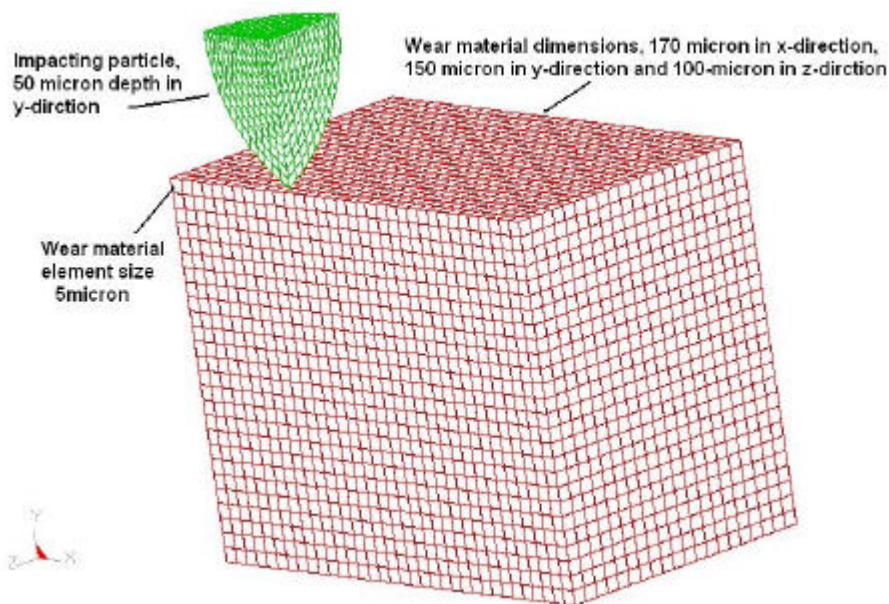


Figure 6.2 Solid FEA model developed for the erosion study

A description of the FEA model shown in figure 6.2 follows. The use of natural symmetry allowed a half model of the wear surface and impacting particle to be used. Boundary conditions were placed on the x - y symmetry plane to prevent motion in the z -direction. Non-reflecting boundary conditions were used on the vertical and base boundaries, to replicate a wear plate of infinite lateral and through thickness dimensions

and thus eliminate stress-wave, wave reflections from the boundaries. The use of symmetry also allowed the 100mm particle to be sliced in half i.e. through the x - z plane giving a particle of 50mm size in the y -direction. The mass of a 100mm particle was maintained by doubling the density of the impacting aluminium oxide particle.

As mentioned earlier, the impact of the angular particle with the wear surface will cause high strains to be encountered. When modelling impacts causing high strains of the wear surface, the FEA model will require a failure criterion so that element removal can be implemented if the failure strain is exceeded. The Johnson-Cook material model has a failure criterion to track plastic-strain, with element removal occurring when the ultimate strain of the element is reached, as defined in equation 6.4 below

$$D = \sum \frac{\Delta \mathbf{e}}{\mathbf{e}_u} \quad (6.4)$$

where $\Delta \mathbf{e}$ is the increment of plastic strain, which occurs during an integration cycle and \mathbf{e}_u is the ultimate strain of the material at failure. Failure and element removal is allowed to occur when $D=1.0$, which in effect, simulates erosion. The element removal method could conceivably be used to simulate erosion for single particle impact events. Erosion of ductile wear surfaces in most cases however occurs by multiple particle impacts. The development of a suitable erosion model would therefore be better suited by the technique of characterisation of material properties in the deformation zone rather than trying to model erosion by the FEA element removal method for a single particle impact event. In the current study, the element removal method is implemented into the model to insure stability of the FEA model rather than to model erosion for the single particle impact. In any case, if the element removal method was not applied, then program terminations may occur if an element in the deformation zone became too distorted (i.e. causing a negative volume element termination to occur for the simulation).

The expression for the ultimate strain to failure as shown in equation 6.4, is given by Johnson and Cook (1985) as

$$\mathbf{e}_u = (D_1 + D_2 \exp D_3 \mathbf{s}^*)(1 + D_4 \ln \dot{\mathbf{e}}^*)(1 + D_5 T^*) \quad (6.5)$$

where $D_1 \dots D_5$ are constants which are determined experimentally by tensile test experiments, \mathbf{s}^* is the ratio of mean pressure to the von-Mises stress, $\dot{\mathbf{e}}^*$ the strain rate and T^* the homologous temperature. Obtaining model constants for this study would involve extensive tensile testing of the materials at various strain-rates, until failure occurred.

For most ductile materials, the effects of strain-rate are to reduce the ultimate failure strain. A simple approximation on the effects of the ultimate strain to failure due to strain-rate effects could be observed from the stress-strain curves as shown in the stress-wave monitoring sections of Chapter 5. As shown, the polymer materials showed considerable effects of strain-hardening, which were modelled by increasing the value of the strain-hardening term B of the Johnson-Cook model, as shown in figures 5.29 and 5.30. An approximation of the ultimate strain of each material could be justifiably made by considering the ratio of the maximum strain at the revised values for B to the maximum strain observed using the initial estimated value for B , where the initial value for B was obtained at much lower strain rates. An estimate was therefore made for the ultimate failure strain of each polymer of 65% of the ultimate failure strain obtained under low strain-rate conditions, using the observation contained in figures 5.29 and 5.30.

The estimated values for ultimate strain of the polymers were subsequently used for deformation energy capacity calculations of equation 6.3 and for the first term D_1 of equation 6.5. Other terms (D_2-D_6) in equation 6.5 were set to zero to simplify the failure model. In the stress-wave monitoring study it was also shown that the strain-hardening parameter B , for AISI 1020 steel was shown to be less sensitive to strain-rate effects and as a result the quasistatic value of the ultimate strain to failure was maintained for the study.

6.2.3 Erosion testing procedure

Erosion testing was conducted to the AISI 1020 steel, UHMWPE and VER wear specimens at 45-degree impact angle, using 90-125 μ m angular aluminium oxide particles. The impact velocities of the abrasive particles were 54, 104 and 150 m/s. Particle velocity was measured with the double disc system prior to erosion testing as described in section 3.4.6. The piezo-electric transducer (as described in section 3.3.4) was used to monitor stress-waves for the counting of individual particle impacts. A frequency counter was used to count individual stress-waves recordings from the impact events. Recognisable erosion of the wear surfaces occurred after approximately 40,000 impacts or approximately 1 hour of erosion testing. Erosion rates are presented as the volume lost in mm³ per particle impact.

6.2.4 Specimen manufacture and material properties

The AISI 1020 steel and UHMWPE specimens were supplied from the manufacturer in sheet form. The VER specimens were manufactured by the process described in section 5.3.3. All specimens were cut to the nominal size of 35 x 30 x 10mm thick and polished on both sides using silicon carbide abrasive paper, up to 2000 grit size. Material property parameters for the Johnson-Cook material model were derived from the stress-wave monitoring sections, 5.2 and 5.3 and are shown for AISI 1020 steel, UHMWPE and VER in Tables 6.1 and 6.2.

Table 6.1 Elastic and thermal material property parameters required for the FEA model. Appendix C contains manufacturers material specifications

Material	E GPa	G GPa	ρ kg/m ³	ν Poisson's ratio	Specific heat J/kg K	Thermal Conductivity W/mK	Coefficient of friction
AISI 1020 steel	207	81	7830	0.29	480	42	0.4
UHMWPE	1.77	0.62	990	0.43	1800	0.21	0.4
VER	4.46	1.63	1070	0.36	1800	0.21	0.4
Aluminium Oxide particles	385		3990	0.26	280	21	

This page left intentionally blank

Table 6.2 Johnson-Cook material property parameters for FEA model. Values for B , n , C and b derived from the stress-wave monitoring sections in Chapter 5. Appendix C contains manufacturers material specifications for other parameter values

Material	A MPa	B MPa	n	C	T_{room} Deg C	T_{melt} Deg C	b	D_1 e_u	S_u MPa	B_m GPa
AISI 1020 Steel	350	270	0.36	0.022	25	1400	1	0.8	450	140
UHMWPE	21	120	0.36	0.07	25	140	1	2.75	48	1.9
VER	90	150	0.36	0.140	25	140	1	0.08	90	5.3

6.2.5 Temperature and strain-rate values obtained from FEA simulations

The temperature and strain-rates required to determine the deformation energy capacity of each material (equation 6.3) were obtained from the FEA model described in section 6.2.2. Figure 6.3 shows the temperature in the deformation zone for an impact to UHMWPE at 54m/s. An average temperature in the highly strained region, described earlier (section 6.2.1) as zone1, was estimated by colour matching with the temperature range bar on the right of the image. From the figure shown, the average temperature in the deformation zone of the UHMWPE material was taken as 66° C.

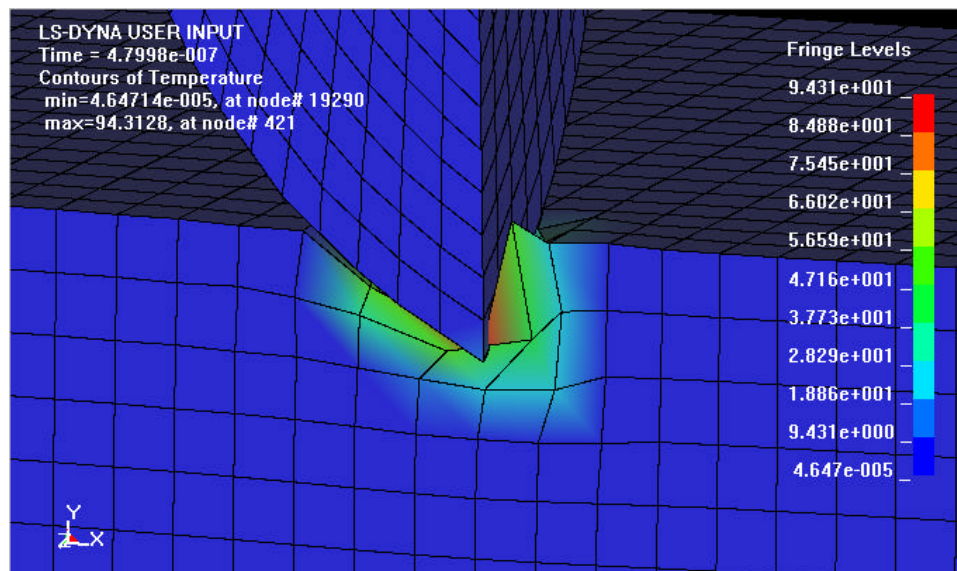


Figure 6.3 FEA model result showing temperature recorded in the impact zone for an angular particle impact to UHMWPE at 54m/s and impact angle of 45°

This page left intentionally blank

Figure 6.4 shows the average temperature in the deformation zone obtained from the FEA simulations for each material. As shown a linear relationship existed between impact velocity and temperature rise for each material. The results can also be used to predict safe limits for particle velocity to avoid melting of the wear surface and excessive erosion. UHMWPE and AISI 1020 steel would suffer severe erosion due to surface melting at impact velocities approaching 220m/s and 600m/s respectively, assuming the linear relationship can be extrapolated to higher impact velocities. VER showed only a modest rise in temperature, which is due to the materials relatively low plastic deformation capacity.

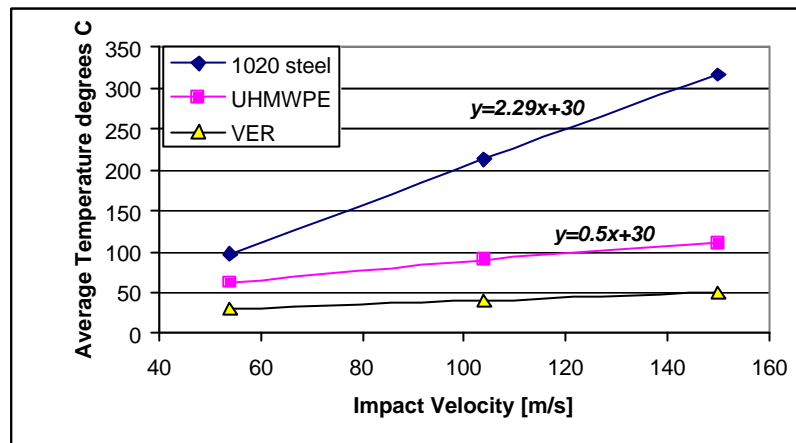


Figure 6.4 FEA model results of temperature rise in deformation zone as a function of impact velocity

The strain-rates were obtained from the FEA model using the method described in section 5.2.8. The results showed a linear relationship of strain-rate as a function of impact velocity, as shown in figure 6.5.

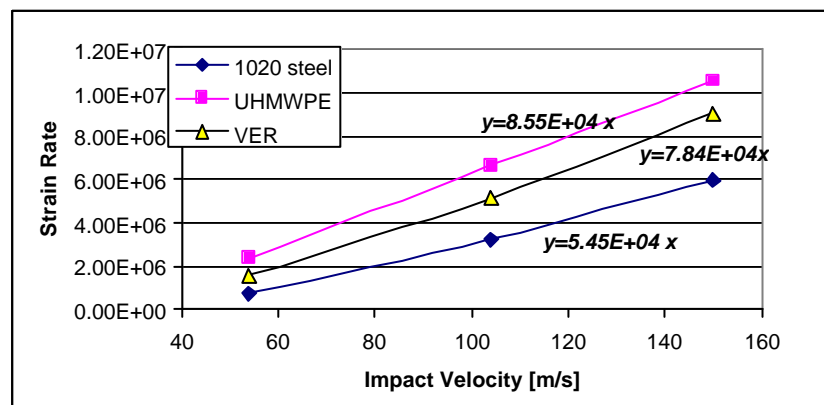


Figure 6.5 Strain-rates as a function of impact velocity derived from FEA simulations

6.2.6 Erosion results compared with erosion model prediction

In this section, erosion results are compared with erosion model predictions. As discussed in section 6.2.1, two different erosion models were presented based on the deformation energy capacity of the wear material. The Ratner-Lancaster model (equation 6.1) assumed deformation energy to be proportional the product of the ultimate stress and ultimate strain obtained under quasistatic conditions. A new computational model was then proposed which determined deformation energy capacity as a function of strain-rate and thermal effects. As explained, values for the computational model (equation 6.2) were derived from the stress-wave monitoring sections of Chapter 5 and FEA model results for strain-rates and surface temperatures shown in the preceding section.

To calculate predicted erosion rates for each erosion model, a value for the constant k of equation 6.2 was derived. In the comparison study, the constant k was calculated by taking the slope of the curve defining the experimental erosion rates as a function of the erosion rates of the models. As shown in figure 6.6, the constant k , for AISI 1020 steel was found to be 0.012.

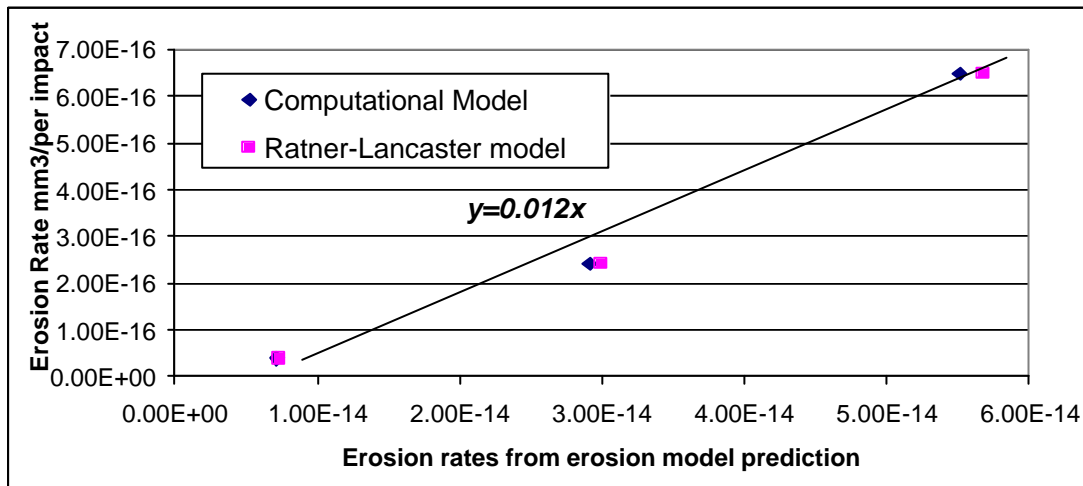


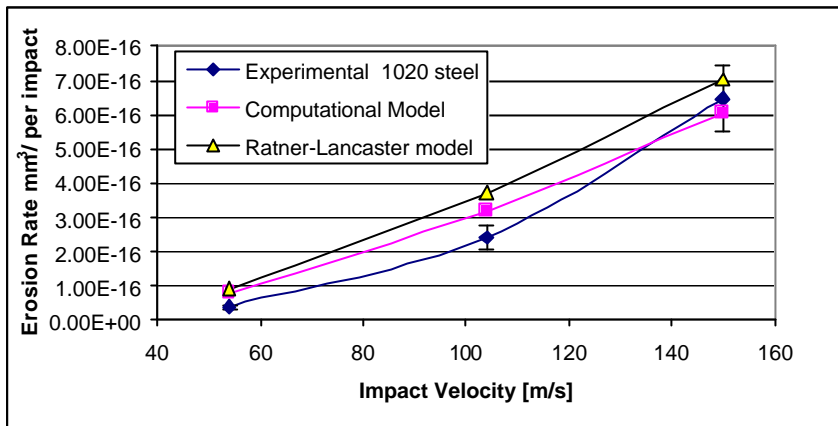
Figure 6.6 Erosion rate as a function of each erosion model prediction for AISI 1020 steel, where the erosion models are defined in equations 6.1 and 6.2

Experimental erosion results for AISI 1020 steel are compared in figure 6.7a with the Ratner-Lancaster model (equation 6.1) and the computational model (equation 6.2). As shown, close agreement was obtained between experimental erosion rates and both

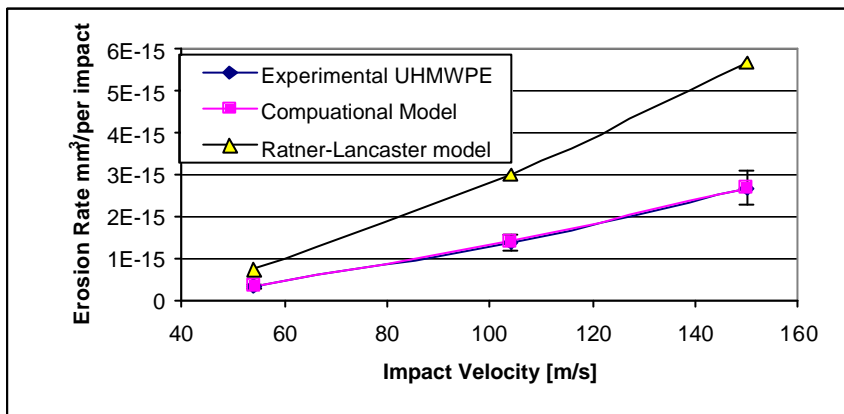
model predictions. The close agreement between the experimental results and each erosion model suggests that strain-rate effects are not a significant factor in regards to erosion resistance for AISI 1020 steel. In trying to understand the results shown in figure 6.7a, it is shown in the stress-wave monitoring section 5.2, that AISI 1020 steel showed no significant increase in strain-hardening as a function of strain-rate effects. In the stress-wave study, the value for the strain-hardening term B of the Johnson-Cook model was shown to be constant over the range of strain-rates from 100s^{-1} (i.e. the initial value obtained from Johnson and Cook, 1983) to the strain rate of $0.22 \times 10^6\text{s}^{-1}$ (i.e. the highest strain rate in stress-wave study). The close agreement between the two erosion model results, suggest that for a material which does not strain-harden significantly at high strain-rates, the deformation energy capacity hence erosion rate is predicted well by the Ratner-Lancaster model. The computational model although more soundly based on material property characterisation under high strain-rate conditions, showed no significant improvement in erosion rate predictions for AISI 1020 steel.

Experimental and erosion model predictions are shown for UHMWPE and VER in figures 6.7b and 6.7c. The results show the Ratner-Lancaster and computational erosion models are in close agreement with experimental results at the lowest impact velocity of 56m/s. However as the impact velocity is increased, the variance between the erosion models became more significant. The results are not unexpected, as discussed in the stress-wave monitoring study (section 5.3), the polymers showed significant sensitivity to strain-rate effects, resulting in strain-hardening. Under low velocity impact conditions, both erosion models are in close agreement, however as the impact velocity is increased to 100 and 150m/s, strain-rate effects become more apparent. The results of the polymer erosion study show the Ratner-Lancaster model is suitable for modelling of the erosion rate up to the impact velocity of 54m/s. At higher impact velocities, 104 and 150m/s, the computational model was shown to be in close agreement with experimental results. The results from the polymer study portray a similar trend as described by the Finnie (1967) study of the erosion characteristics of heat-treated steels. As described in the study by Finnie, erosion rates for metals with low strain-hardening capacity were shown to be higher than metals, which had high strain-hardening capacity.

(a)



(b)



(c)

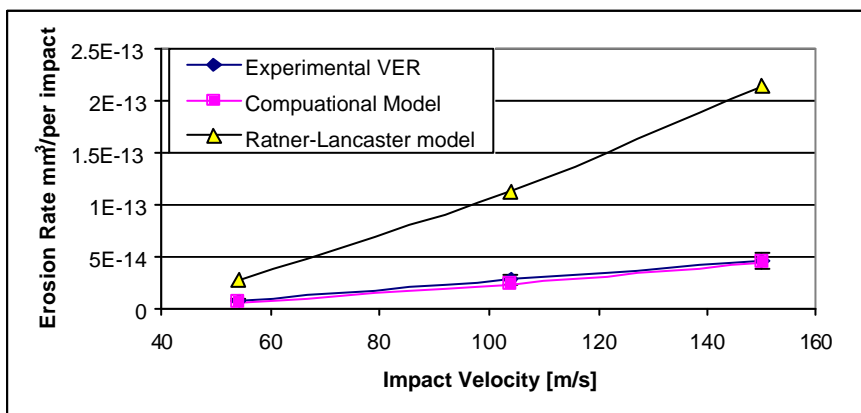


Figure 6.7 Erosion results using 90-125 μ m aluminium oxide particles impact at 45-degree impact angle compared to Ratner-Lancaster and computational model (a) AISI 1020 steel (b) UHMWPE (c) VER

6.3 Chapter Summary

The main conclusions to be drawn from the erosion study is the important link in identifying how material property parameters obtained under high strain-rate conditions, can be implemented into a computational erosion model. The Ratner-Lancaster model was used as the base model for the study. It was shown that the Ratner-Lancaster model's linear approximation for deformation energy capacity, obtained by the inverse product of the ultimate stress and ultimate strain was adequate in predicting erosion rates for AISI 1020 steel. The computational model also showed good agreement with experimental erosion rates. In drawing a conclusion from the erosion study, it was noted that AISI 1020 steel showed no significant strain-hardening effects as strain-rate increased, as shown in the stress-wave monitoring study of section 5.2. As a result, deformation energy capacity was not excessively strain-rate dependant for AISI 1020 steel.

The polymer materials did however show significant strain-hardening, which had the effect of increasing deformation energy capacity as strain-rates increased. It was shown that experimental erosion rates were in close agreement with computational erosion model predictions. The significance of accounting for strain-hardening as a result of strain-rate effects, was exemplified in the polymer erosion study.

This page left intentionally blank

CHAPTER 7

DISCUSSION AND CONCLUSION

7.1 Important findings

7.1.1 Introduction

In this thesis, a new stress-wave monitoring process was developed for the study of materials subjected to high velocity, erosive particle impacts. The need for the development of the stress-wave monitoring process became apparent early in the study when it was discovered that parameters of existing erosion models, such as flow stress, ultimate stress and ultimate strain were basically obtained from quasistatic experimental data. It was evident, particularly for polymer materials that material property parameters could change dramatically under high strain-rate impact conditions.

As shown in the literature review, only a few attempts have previously been made to design and implement a stress-wave monitoring process for the study of small particle impacts and erosion phenomena. This study has shown that stress-waves can be used successfully to characterise material properties at strain-rates at least two orders of magnitude above the strain-rates obtainable by the conventional SHPB method.

7.1.2 Piezo-electric transducer design

The main concerns for the transducer design were internal wave reflections and the trade-off between sensitivity on the one hand (suggesting large sensing elements) and effects of spatial averaging on the other hand (suggesting small sensing elements).

A numerical study was conducted to minimize the effects of spatial averaging. Spatial averaging occurred when the stress-wave, which is propagating on a spherical path away from the impact zone, passes through the flat piezo-electric sensing element, and the curvature of the wave distorts the recorded waveform. The numerical study showed the optimum design for the transducer was; the piezo-electric sensing element diameter of 6mm, the transducer placed 10mm from the impact site and particles of 0.4mm used for the impact of the wear surface. To minimize the effects of internal wave reflections, a backing rod of the same piezo-electric material was used behind the piezo-electric sensing element. The backing rod allowed the stress-wave to progress down the rod, which was long enough so that the wave reflection would not interfere with the initial stress-wave recording.

7.1.3 Stress-wave interpretation

The fundamentals of piezo-electric materials were studied in order to interpret the recorded stress-wave voltage signal as some measurable mechanical quantity. Some confusion arose from a previous study by Buttle and Scrubby (1990), who used a piezo-electric probe to monitor stress-wave profiles from small particle impact events. The interpretation in the Buttle and Scrubby study was that the recorded stress-wave signal was proportional to displacement. However displacement measurements could only occur if the backing material of the piezo-electric sensing element was infinitely stiff. By using a simple one-dimensional analysis of a stress-wave passing through the piezo-electric sensing element, it was shown that the transducer designed for this study would in fact measure strain, which is proportional to stress.

The stress state at the piezo-electric sensing element is more complex than the one-dimensional assumption. A three-dimensional stress state will exist particularly at the wear material / transducer interface. It was discussed that the sensitivity of the piezo-electric sensing element was such that the normal stress would be the more predominant stress component being recorded by the passage of the stress-wave through the piezo-electric sensing element.

7.1.4 Effects of stress-wave recording from piezo-electric transducer coupling

In the AISI 1020 steel impact and stress-wave monitoring study, it was shown that the amplitude and phase of the stress-wave transmitted to the piezo-electric transducer could change. The apparent phase shift of the stress-wave was most noticeable at higher impact velocities, suggesting a frequency dependant relationship existed. To model the contact interface of the wear material and piezo-electric transducer, two models were proposed; a compliant contact model (CC model) and an ideally stiff contact interface (ISC model). The stress-wave monitoring study of AISI 1020 steel showed that for low velocity impacts at 2.5 and 21m/s, the ISC model accurately described the experimental stress-wave profile in regards to phase and amplitude. However for the same velocity impacts (2.5 and 21m/s) the CC model showed some degree of numerical instability, causing unrealistic waveform characteristics. The cause of the numerical instability appeared to be a fault in the LS DYNA code when the model is implemented for situations where low stress levels ($< 0.1\text{MPa}$) at the contact interface occur. At higher impact velocities, the stress-waves from the CC model were shown to be in phase with experimental results. It was concluded from the study that the phase transformation of the stress-waves at the impact velocities of 52 and 104m/s were frequency dependent. The physical understanding as to the cause of the phase transformation was put down to the inclusion of the oil-coupling medium between the contact interfaces. It was concluded that the oil-coupling medium can only transmit tensile stresses by suction effect and as a result, stress-waves of high frequency having compressive and tensile stress components, may show a phase shift and amplitude reduction if a lowering of tensile stress transmission occurs.

The main findings from the contact interface study were that the ISC model worked effectively for stress-wave frequencies below 0.9MHz and the CC model for stress-wave frequencies above 0.9MHz. The significance of the findings was that the frequency dependant limitations when using oil as a coupling medium were recognised in the study. The significance of developing the CC model is that frequency dependant limitations of the contact interface can be overcome and valuable insight gained into material response under high velocity impact conditions.

7.1.5 Stress-wave monitoring of erosive particle impacts

In this study it was shown that for impacts causing elasto-plastic deformation of the wear surface, the stress-wave recorded at the rear face of the impacted plate, showed wave dispersion effects. To investigate dispersion effects in more detail, an FEA simulation was conducted for an elastic model and an elasto-plastic impact model. The main difference when the waveforms were compared at various depths below the surface was the stress-wave from the elasto-plastic model was broader and the rise time from zero stress to maximum amplitude was longer as compared to the elastic model. It was hypothesized that as a result of wave dispersion, faster moving elastic waves would separate from slower moving plastic waves and as a result, the amplitude of the stress-wave recorded at the piezo-electric transducer location, would scale to the elastic component of the stress at the surface, i.e. the dynamic yield stress at the surface. The result of the FEA comparison study was an important finding as it was then possible to identify key parameters of the Johnson-Cook model relating to elastic deformation of the surface. The significance of the finding was that by comparing the amplitude of the longitudinal stress-waves obtained experimentally with those obtained by the FEA method; it was possible to validate the strain-rate parameter C of the Johnson-Cook model for AISI 1020 steel.

The parameters of the Johnson-Cook model, which could not be validated by the stress-wave monitoring process, were the parameters relating to plastic deformation of the surface, and they were the strain-hardening terms. It was shown that the strain-hardening parameters could be validated by the study of the impact craters left on the steel wear surface. It was shown that all Johnson-Cook model parameters could be validated by the combined study of stress-wave motion and impact crater formation. The importance of this process is that material properties can be gained easily and inexpensively for a wide variety of isotropic materials at strain-rates at least two orders of magnitude above conventional SHPB methods.

The robustness of the stress-wave monitoring process was demonstrated in the study of ultra high molecular weight polyethylene (UHMWPE) and vinyl ester resin (VER). The Johnson-Cook material model was used successfully in the FEA modeling of the impact and stress-wave motion study of the polymers. The stress-wave study showed the strain-

rate parameter C was 0.07 for UHMWPE and 0.14 for VER. The higher value for VER indicated the material's sensitivity to strain-rate effects. With these parameters so chosen, the Johnson-Cook material model used in conjunction with FEA modeling gave good agreement with experimental observations of deformation characteristics of the polymers studied in this work.

The impact crater studies showed the polymer wear surfaces to strain-harden considerably in comparison with initial estimates obtained from the quasistatic stress-strain curve of a similar polymer. It was considered that the effects of strain-hardening of the polymer wear surfaces was a result of the hydrostatic stress component. The Johnson-Cook model contains strain-hardening terms, which are, strain-rate and temperature dependent. A sensitivity study showed that the strain-hardening term B of the Johnson-Cook model needed to be increased at least four fold to account for the strain-hardening of the polymers.

7.1.6 Implementation of stress-wave monitoring process for the study of erosion

The combined experimental / computational approach of stress-wave motion and FEA model validation paved the way for a better understanding of materials at high strain-rate. The next step was to link the process for the study of erosion and the development of an improved erosion model. The Ratner-Lancaster model and a revised computational version of the Ratner-Lancaster model were implemented for the study. Both models assume erosion to be inversely proportional to deformation energy capacity. The computational model was designed to calculate deformation energy capacity using terms, which were strain-rate and temperature dependant. The Ratner-Lancaster model uses terms for deformation energy capacity derived from quasistatic values of ultimate stress and ultimate strain. The input parameter values needed for the computational erosion model were derived from the stress-wave monitoring study. The remaining values required, were the strain-rate and temperature in the deformation zone and these were derived from FEA simulations of angular particles impacting the wear surface at 45-degrees impact angle. The results showed that the Ratner-Lancaster and

revised computational model showed similar erosion rate prediction for AISI 1020 steel and in accordance with experimental results. The close agreement of erosion results for each model was not unexpected, as it was evident in the stress-wave monitoring study that AISI 1020 steel showed no real significant effects of increased strain-hardening as strain-rate increased. The effects of strain-hardening are to increase deformation energy capacity, as more energy is required to plastically deform the material.

The stress-wave monitoring study of the polymers however, showed significant strain-hardening. The computational erosion model was shown to be in close agreement with experimental results for the polymers over the impact velocities range of 54 to 150m/s. The Ratner-Lancaster model, which as stated earlier is based on quasistatic parameter values, showed good agreement with experimental results at the lowest impact velocity of 54m/s, however at the higher impact velocities of 109 and 150m/s divergence from experimental erosion rates occurred, indicating that above 54m/s, strain-rate effects become more predominant for the polymers.

The significance of developing the computational erosion model is that erosion can be modelled for a wide variety of ductile materials. As shown in the study, once material model parameters are obtained from the stress-wave monitoring study, an erosion analysis can proceed by the FEA method. The significance of this approach is that time-consuming erosion experiments can be minimized or completely removed from an erosion study. The study showed that accurate erosion rate predictions could be obtained from the methods developed in this study. The computational model was shown to be accurate for predicting the erosion rates of steel and ductile polymer materials over a wide range of impact velocities. The computational erosion model is ideally suited for studying much higher impact velocities, where experimental limitations of impact velocity may occur. The computational erosion model allows for ambient temperature as an input model parameter and as a result could conceivably be used to model erosion for high temperature applications, which are commonly encountered in coal fired power stations and jet engine turbines.

Bibliography

- Allen S. P, Page N. W, Dastoor P, (2002) "Stress-wave monitoring of individual particle impacts during erosion tests." Proceedings of 6th International Tribology Conference. Published by Fineline, Perth WA. Volume 1 Pages 235-239
- Arnold J. C, Hutchings I. M, (1992) "A model for the erosive wear of rubber at oblique impact angles" Journal of Applied Physics Vol 25, pages A-222-A229
- Arnold J. C, Hutchings. I. M, (1993) "Erosive wear of rubber by solid particles at normal incidence" Wear Vol 161, pages 213-221
- Beer, F. P, Johnston J. R. (1992) "Mechanics of materials." McGraw Hill England
- Bergstrom J. S, Rimsnac C. M, Kurtz S. M. (2003) "Prediction of mechanical behavior for conventional and highly cross linked UHMWPE using hybrid constitutive model" Biomaterials Vol 24, pages 1365-1380
- Briscoe B. J, Pickles M. J, Julian K. S, Adams M. J, (1997) "Erosion of polymer-particle composite coatings by liquid water jets" Wear Vol 203-204, pages 88-97
- Buckly C. P, Harding J. P, Hou J. P, Ruiz A, Trojanowski A. (2001) "Deformation of thermosetting resins at impact rates of strain. Part 1: Experimental study." Journal of the Mechanics and Physics of Solids. Vol 49, pages 1517-1538
- Budinski K.G. (1997) "Resistance to particle abrasion of selected plastics." Wear. Vol: 203-204, pages 302-309
- Buttle D. J, Scruby C. B, (1990) "Characterisation of particle impact by quantitative acoustic emission" Wear Vol 137, pages 63-90
- Cook R. D, (1995) "Finite element modelling for stress analysis" John Wiley and Sons, Inc New York
- Dean G, Read B, (2001) "Modelling the behavior of plastics for design under impact" Polymer Testing. Vol 20, pages 677-683
- Eyring H (1936) Journal of Chem. Phys. Vol 4, page 283
- Ferrer F, Idrissi H, Mazille H, Fleischmann P, Labeeuw P, (1999) "On the potential of acoustic emission for the characterization and understanding of mechanical damaging during abrasion-corrosion processes" Wear, Vol 231, pages 108-115

Field J. E, Hutchings I. M, in Blazynski T.Z. (1987) "Materials at High Strain-rates." Elsevier Applied Science, London and New York

Finnie I (1960) "Erosion of surfaces by solid particles." Wear Vol 3, pages 87-103

Finnie I, Wolak J, Kabil Y (1967) "Erosion of metals by solid particles" ASTM Journal of Materials 2, pages 359-373

Finnie, I. (1995) "Some reflections on the past and future of erosion." Wear Vol 186-187, pages 1-10

Goldsmith W. (1960), "Impact" Richard Clay and Company, Suffolk England

Goodier J. N, Jahsman W. E, Ripperger E. A, (1959) "An Experimental Surface-Wave Method for Recording Force-Time Curves in Elastic Impacts" Journal of Applied Mechanics March 1959, pages 3-7

Gorham D. A., Wu X. J. (1996) "An empirical method for correcting dispersion in pressure bar measurements of impact stress." Meas. Sci. Technology Vol 7 Pages 1227-1232

Hamouda A. M. S, Hashmi M. S. J, (1996) "Modelling the impact and penetration events of modern engineering materials :Characterisation of modern computer codes" Journal of Materials Processing Technology Vol 56, pages 847-862

Harding J, in Blazynski T.Z. (1987) "Materials at High Strain-rates." Elsevier Applied Science, London and New York

Hibbitt, K and S, (1998), "ABAQUS Theory Manual", Version 5.8, Pawtucket, RI.

Hutchings I. M, Winter R. E, Field J. E (1975) "Solid particle erosion of metals: the removal of surface material by spherical projectiles." Proc. R. Soc. Lond. A. Vol 348, pages 379-392

Hutchings I. M, Deuchar D. W, Muhr A. H, (1987) "Erosion of unfilled elastomers by solid particle impact" Journal of Materials Science Vol 22, pages 4071-4076

Hutchings I. M, (1993) "Mechanisms of wear in powder technology a review" Powder Technology 76 Pages 3-13

Johnson G. R, Cook W. H. (1983) "A constitutive model and data for metals subjected to large strains, high strain-rates and high temperatures" Presented at the Seventh International Symposium on Ballistics, The Hague, The Netherlands

Johnson G. R, Cook. W. H, (1985) "Fracture characteristics of three metals subjected to various strain, strain rates, temperatures and pressures" Engineering Fracture Mechanics Vol 21 No. 1, pages 31-48

Johnston K. L. (1985) "Contact Mechanics" Cambridge University Press, Cambridge U.K.

Kaczmarek Z. (2001) "Waveform reconstruction of impact force using frequency domain technique and one-point strain measurement" Scientific proceedings of Riga Technical University 43rd thematic issue

Kolsky H, (1953) "Stress-waves in Solids." Dover Publications New York

Krautkramer J and H, (1969) "Ultrasonic Testing of Materials." Springer-Verlag, Berlin

Lancaster J.K. (1969) "Characteristics of impact friction and wear of polymeric materials" Wear, Vol 14, pages 223-239

Levy A. V, (1981) "The solid particle erosion behavior of steel as a function of microstructure" Wear Vol 68, pages 269-287

Levy A. V, (1986) "The platelet mechanism of erosion of ductile metals." Wear Vol 108, pages 1-21

Li J, Hutchings I. M, (1990) "Resistance of cast polyurethane elastomers to solid particle erosion" Wear Vol 135, pages 293-295

LS DYNA Theory manual (2003), Livermore Software Technology Corporation, Livermore California

O'Flynn D.J, Bingley M. S, Bradley M. S. A, Burnett A. J, (2001) "A model to predict the solid particle erosion rate of metals and its assessment using heat-treated steels" Wear Vol 248, pages 162-177

PI Ceramics handbook "Micro Positioning, Nano-Positioning, Nano-Automation Solutions for Cutting Edge Technologies" Physik Instruments (PI) Germany

Rabinowicz E, (1965) "Friction and wears of materials." Wiley, New York

Ratner S. B, Styller E. E, (1967) "Comparison of the abrasion of rubbers and plastics" In D. I. James (ed) Abrasion of Rubber, Maclaren, London

Ruff A. W, Ives L. K, (1975) "Measurement of solid particle velocity in erosive wear" Wear Vol 35, pages 195-199

Shewmon P, Sundararajan G (1983) "The erosion of metals." Ann. Rev. Materials Science Vol 13, pages 301-318

Stein H.L (1998) "Engineering Plastics" ASM International, Metals Park, OH USA, Vol 2

Sundararjan G. (1983) "The solid particle erosion of metals and alloys" Trans. Indian Inst. Metals, Vol 36 (6), pages 474-495

Szilard J. (1982) "Ultrasonic Testing" John Wiley and Sons New York

Tabor D, (1951) "The Hardness of Metals" Oxford Clarendon Press, London

Talia. M, Lankarani H, Talia J. E. (1999) "New experimental technique for the study and analysis of solid particle erosion mechanisms" Wear Vol 225-229 pages 1070-1077

Tilly G. P. (1969) "Erosion caused by airborne particles" Wear Vol 14, pages 63-79

Timoshenko S. P, Goodier J. N. (1970), "Theory of Elasticity" McGraw Hill New York

Wang Y. Q, Huang L. P, Liu W. L, Li J. (1998) "The blast behavior of ultrahigh molecular weight polyethylene" Wear Vol 218, pages 128-133

Waterman N.A, Ashby M.F (1997) "The Material Selector", Vol 1, pages 447-454. Published by Chapman and Hall New York

Winter R F, Hutchings I. M (1974) "Solid particle erosion studies using single angular particles." Wear Vol 29, pages 181-194

Zhao P. J, Lok T. S, (2002) "A new method for separating longitudinal waves in a large diameter Hopkinson bar" Journal of applied vibration Vol 257(1), pages 119-130

APPENDIX A

MATLAB PROGRAMS

A.1 Matlab programs

This appendix provides the source codes for Matlab programs used in this research. All programs were written for implementation in *Matlab* (version 5.3.1, The MathsWorks, Inc. 1999).

A.1.1 Matlab program for the design of the piezo-electric transducer

The following code was written to aid in the design of the piezo-electric transducer as described in section 3.3.2

```
clear all
%Disclaimer
%This program has been written for the purposes of postgraduate research
%at the University of Newcastle, in the period 2001-2004
%while every attempt has been made to ensure correct and accurate functionality
%any implied warranties or guarantees are specifically disclaimed

% This m file calculates the output response of the piezo material
% at any given x,y,z location

% Enter in the dimensions of the piezo-electric sensing element
% The radius of the sensing element is
Xcord=3.0e-3;

% The thickness of the sensing element is
Ycord=0.20e-3;

% Discretise the sensing element into the x,y coordinate plane
Xgrid=0:Xcord/49:Xcord;
Xgrid=Xgrid';
Ygrid=0:Ycord/24:Ycord;
Ygrid=Ygrid';

% Import the stress-wave profile f(t) fromLS DYNA simulation
```

```

fid1a=fopen('stress at 10mmJC140conMean.txt','r');
a1a1=fscanf(fid1a,'%g %g',[2 inf]);

a1a1=a1a1';
a1b=a1a1(:,2);
time=a1a1(:,1);
a1b=a1b.*-1;
[Ca1 Da]=find(a1b(1:end)>0.008);
f=a1b(Ca1(1)-1:end);
timea=time(Ca1(1)-1:end);
time=timea-time(Ca1(1)-1);
%f is the stress-wave function
f=f(1:1:end);
[B3 N]=size(f);

% Implement a timescale for the stress-wave (same as f(t) timescale)
timescale=0:1e-8:8.0e-6-1e-8;

% The thickness of the wear plate
Th=10.0e-3;

% Offset the piezo-electric sensing element to account for wear plate thickness
Ygrid=Ygrid+Th;

% Find the radial R distance values of each point in discretised sensing element from impact site
R=zeros(25,50);

for i=1:50;
    for j=1:25;

        R(j,i)=sqrt(Xgrid(i)^2+Ygrid(j)^2);
    end
end

% Find the angle of each discretised point of discretised point in sensing element relative to impact site
for i=1:50;
    for j=1:25;
        feta(j,i)=atan(Xgrid(i)/Ygrid(j));
    end
end

% Find the radial distance of each point of discretised piezo-sensing element from the face of the
% sensing element to the point discretised point within the sensing element
for i=1:50;
    for j=1:25;

Rpiezo(j,i)= (Ygrid(j)-Th)*cos(feta(j,i));

    end

end

% Rsteel is the radial distance of the face of the sensing element to the impact site
Rsteel=R-Rpiezo;

% The wave speed of steel and piezo is
C1=5800;
C2=2600;

% The time required for the stress-wave to reach a point in the discretised sensing element

```

```

Tp=zeros(25,50);
for i=1:50;
    for j=1:25;
        Tp(j,i)=(Rsteel(j,i)/C1)+(Rpiezo(j,i)/C2);
    end
end

% The face area of each annuli element making up the piezo-electric sensing element
for i=1:49;
    A1(i)=pi*((Xgrid(i+1)-Xgrid(i))/2+Xgrid(i))^2;
end
A1=A1';
A2(1)=A1(1);
for i=1:48;
    A2(i+1)=A1(i+1)-A1(i);

end
% The volume of each annuli element
A2(50)=A2(49);
A2=A2';
area=sum(A2)
V2=A2.*0.2e-3/25;
vol=pi*Xcord^2*Ycord
% V2=V2.

% The volume matrix of the piezo-electric sensing element
volume=zeros(25,50);
for i=1:50;
    for j=1:25;
        volume(j,i)=V2(i);
    end
end

% Clear some variables to save memory

clear R Xgrid Ygrid Rsteel

% The numerical integration process
Mag1=zeros(800,50,25);
for i=1:50;
    for j=1:25;
        [a,b]=find(timescale(:)>Tp(j,i));
        Mag1(a(1):a(1)+B3-1,i,j)=f(:).*(volume(j,i)/vol);
    end
end

% Now sum up the magnitudes across the surface of the piezo
for j=1:800;
    for k=1:25;
        M(j,k)=sum(Mag1(j,.,k));
    end
end
%Now sum through the thickness
for h=1:800;
    N(h)=sum(M(h,:));
end
clear Mag1 Tp

```

```

N=N';
[k j]=find(N>0);
[v c]=find(N(k(1):end)<0);

N1=N';
[P K]=find(N>0.000001);
t1=timescale(P(1):end);
t1=t1-timescale(P(1));

% N1 is the stress-wave after numerical integration process
N1=N1(P(1):end);

% Plot the output results, f is the initial stress-wave profile, N1 is the stress-wave
% profile after numerical integration
plot(timescale(1:2:200),f(1:2:200),'-+',t1(1:1:end),N1(1:1:end),'-d','MarkerSize',5)
grid on
Grid on
legend('Initial stress-wave','Stress-wave profile after numerical integration')
xlabel('Time')
ylabel('Stress MPa')

```

A.1.2 Matlab program to measure volume loss of wear specimens

The following code was written to measure the volume loss for each wear specimen after erosion testing. The program develops a 3-dimension map of the wear surface by using 2-dimension profiles of the wear surface as recorded by a profilometer as detailed in section 3.4.7.

```

%Disclaimer
%This program has been written for the purposes of postgraduate research
%at the University of Newcastle, in the period 2001-2004
%while every attempt has been made to ensure correct and accurate functionality
%any implied warranties or guarantees are specifically disclaimed

% This m file calculates the erosion volume loss from experimental results

% Input the individual profile up to 10
fid1a=fopen('u54_901.txt','r');
a1a1=fscanf(fid1a,'%g',[1 inf]);
fid1a=fopen('u54_902.txt','r');
a1a2=fscanf(fid1a,'%g',[1 inf]);
fid1a=fopen('u54_903.txt','r');
a1a3=fscanf(fid1a,'%g',[1 inf]);
fid1a=fopen('u54_904.txt','r');
a1a4=fscanf(fid1a,'%g',[1 inf]);
fid1a=fopen('u54_905.txt','r');
a1a5=fscanf(fid1a,'%g',[1 inf]);
fid1a=fopen('u54_906.txt','r');
a1a6=fscanf(fid1a,'%g',[1 inf]);
fid1a=fopen('u54_907.txt','r');
a1a7=fscanf(fid1a,'%g',[1 inf]);

```

```

%fid1a=fopen('u54_908.txt','r');
%a1a8=fscanf(fid1a,'%g',[1 inf]);
%fid1a=fopen('u54_909.txt','r');
%a1a9=fscanf(fid1a,'%g',[1 inf]);
%fid1a=fopen('u54_910.txt','r');
%a1a10=fscanf(fid1a,'%g',[1 inf]);

a1a1=a1a1';
a1a2=a1a2';
a1a3=a1a3';
a1a4=a1a4';
a1a5=a1a5';
a1a6=a1a6';
a1a7=a1a7';
%a1a8=a1a8';
%a1a9=a1a9';
%a1a10=a1a10';

% Give the distance between each profile traverse
ds=0.1e-3;

% The number of profiles
n=7;

% Depth data
a1b=a1a1(:,1);
a2b=a1a2(:,1);
a3b=a1a3(:,1);
a4b=a1a4(:,1);
a5b=a1a5(:,1);
a6b=a1a6(:,1);
a7b=a1a7(:,1);
%a8b=a1a8(:,1);
%a9b=a1a9(:,1);
%a10b=a1a10(:,1);

% Exclude unwanted data
a1a=0:(1.44e-3)/299:1.44e-3;
x=300

dmatrix(:,1)=a1b(100:x+100);
dmatrix(:,2)=a2b(100:x+100);
dmatrix(:,3)=a3b(100:x+100);
dmatrix(:,4)=a4b(100:x+100);
dmatrix(:,5)=a5b(100:x+100);
dmatrix(:,6)=a6b(100:x+100);
dmatrix(:,7)=a7b(100:x+100);
%dmatrix(:,8)=a8b(100:x+100);
%dmatrix(:,9)=a9b(100:x+100);
%dmatrix(:,10)=a10b(100:x+100);

% Build a two-dimensional grid matrix
Y=0:ds:(ds*n)-ds;

dmatrix=dmatrix.*(1e-6/0.0114);
Dy=0:(ds*n)/299:(ds*n);

Z1=zeros(x,x);

% Interpolate between each profile

```



```

a1s=a1a1(:,2:11);

% The time data
time=(a1a1(:,1));
% The areas

% The radial distance of the centre of each annulus is
R1=0.3e-3;
R2=0.6e-3;
R3=0.9e-3;
R4=1.2e-3;
R5=1.5e-3;
R6=1.8e-3;
R7=2.1e-3;
R8=2.4e-3;
R9=2.7e-3;
R10=3e-3;

% The area of each annulus is
A1=pi*(R1/2)^2;
A2=(pi*(((R2-R1)/2)+R1)^2)-A1;
A3=(pi*(((R3-R2)/2)+R2)^2)-(A1+A2);
A4=(pi*(((R4-R3)/2)+R3)^2)-(A1+A2+A3);
A5=(pi*(((R5-R4)/2)+R4)^2)-(A1+A2+A3+A4);
A6=(pi*(((R6-R5)/2)+R5)^2)-(A1+A2+A3+A4+A5);
A7=(pi*(((R7-R6)/2)+R6)^2)-(A1+A2+A3+A4+A5+A6);
A8=(pi*(((R8-R7)/2)+R7)^2)-(A1+A2+A3+A4+A5+A6+A7);
A9=(pi*(((R9-R8)/2)+R8)^2)-(A1+A2+A3+A4+A5+A6+A7+A8);
A10=(pi*(R10)^2)-(A1+A2+A3+A4+A5+A6+A7+A8+A9);

% The total area is
Area=A1+A2+A3+A4+A5+A6+A7+A8+A9+A10;

a1s(:,1)=a1s(:,1).*A1/Area;
a1s(:,2)=a1s(:,2).*A2/Area;
a1s(:,3)=a1s(:,3).*A3/Area;
a1s(:,4)=a1s(:,4).*A4/Area;
a1s(:,5)=a1s(:,5).*A5/Area;
a1s(:,6)=a1s(:,6).*A6/Area;
a1s(:,7)=a1s(:,7).*A7/Area;
a1s(:,8)=a1s(:,8).*A8/Area;
a1s(:,9)=a1s(:,9).*A9/Area;
a1s(:,10)=a1s(:,10).*A10/Area;

% The numerical integration process
[K L]=size(a1s);
% Now sum accross the areas
for i=1:K;

    a1b(i)=sum(a1s(i,:));
end

a1b=a1b.*-1;
a1b=a1b';

```

```

% Find the start of the stress-wave at time zero
[Ca1 Da]=find(a1b(1:end)>0.01);
a2b1=a1b(Ca1(1)-1:end);
timea=time(Ca1(1)-1:end);
time1=timea-time(Ca1(1)-1);

% Import the experimental data
load('D:\Impact exp 1020 steel 6-01-04\05mm impact 10mm 1020 steel 100ms\data.mat')

% Scale experimental data according to piezo-electric constant, a1ba and ave is obtained from data.mat
ave=ave./(22.8e-3*0.2e-3);
% Scale data to MPa
ave=ave./1e6;
% Scale the experimental data according to calibration value
ave=ave.*2.71;

% Plot the results
plot(a1ba(1:4:200),ave(1:4:200),'-*',time1(1:2:400),a2b1(1:2:400),'-d','MarkerSize',4)
grid on

Grid on
legend('Experimental stress at 10mm','FEA no contact defined','FEA contact defined')
xlabel('Time')
ylabel('stress MPa')
axis([0 1.5e-6 -0.3 0.3])

```

APPENDIX B

LS DYNA FEA PROGRAMS

B.1 LS DYNA programs

This appendix provides the source codes for the LS DYNA FEA models used in this research. The FEA models were solved using LS DYNA version 970 (Livermore Software Technology, Livermore CA, USA)

B.1.1 LS DYNA input code for stress-wave monitoring FEA model

The following LS DYNA input files were used for the stress-wave monitoring models used in section 5.2 and 5.3. Element and nodal information are not shown due to the large number of elements in the model. The input file shown is for AISI 1020 steel; other materials were modelled by changing the relevant material property cards of the input file.

```
$-----1-----2-----3-----4-----5-----6-----7-----8
$ LS-DYNA(970) DECK WRITTEN BY : eta/FEMB-PC version 28.0
$ ENGINEER :
$ PROJECT :
$ UNITS : MM, TON, SEC, N
$ TIME : 09:11:45 PM
$ DATE : Wednesday, September 24, 2003
$-----1-----2-----3-----4-----5-----6-----7-----8
*KEYWORD 180000000
$-----1-----2-----3-----4-----5-----6-----7-----8
*TITLE
LS-DYNA USER INPUT
$-----1-----2-----3-----4-----5-----6-----7-----8
$
$ CONTROL CARD
$
$-----1-----2-----3-----4-----5-----6-----7-----8
*CONTROL_TERMINATION
$ ENDTIM ENDCYC DTMIN ENDENG ENDMAS
0.000080 0 0.0 0.0 0.0
*CONTROL_ACCURACY
$ OSU INN PIDOSU
1 2 0
*CONTROL_BULK_VISCOSITY
$ Q1 Q2 TYPE
1.5 0.060 1
$-----1-----2-----3-----4-----5-----6-----7-----8
$
$ DATABASE CONTROL FOR ASCII
$
$-----1-----2-----3-----4-----5-----6-----7-----8
*DATABASE_ELOUT
$ DT BINARY
1.0000E-08 2
```

```

*DATABASE_GLSTAT
$ DT BINARY
1.0000E-08 2
*DATABASE_NODOUT
$ DT BINARY
1.0000E-08 2
*DATABASE_RCFORC
$ DT BINARY
1.0000E-08 2
*DATABASE_MATSUM
$ DT BINARY
1.0000E-08 2
$-----1-----2-----3-----4-----5-----6-----7-----8
$
$ DATABASE CONTROL FOR BINARY
$
$-----1-----2-----3-----4-----5-----6-----7-----8
*DATABASE_BINARY_D3PLOT
$ DT/CYCL LCDT BEAM NPLTC
0.00000050 0 0 0
$-----1-----2-----3-----4-----5-----6-----7-----8
$
$ DATABASE HISTORY CARDS
$
$-----1-----2-----3-----4-----5-----6-----7-----8
*DATABASE_HISTORY_SHELL
$^HISTORY_2
$ SID1 SID2 SID3 SID4 SID5 SID6 SID7 SID8
241340 241316 241288 241260 241232 241204 241176 241148
*DATABASE_HISTORY_SHELL
$^HISTORY_3
$ SID1 SID2 SID3 SID4 SID5 SID6 SID7 SID8
241124 241100 774685 730674 730827
*DATABASE_HISTORY_NODE
$^HISTORY_3
$ NID1 NID2 NID3 NID4 NID5 NID6 NID7 NID8
799143 258515 800074
*DATABASE_HISTORY_SHELL
$^HISTORY_4
$ SID1 SID2 SID3 SID4 SID5 SID6 SID7 SID8
776495 777111 40651 40681 40720 40760
$-----1-----2-----3-----4-----5-----6-----7-----8
$
$ PART CARDS
$
$-----1-----2-----3-----4-----5-----6-----7-----8
*PART SHEADING
steel
$ PID SECID MID EOSID HGID GRAV ADPOPT TMD
1 1 13 0 1 0 0 0
*PART SHEADING
PizeoAE
$ PID SECID MID EOSID HGID GRAV ADPOPT TMD
6 1 10 0 1 0 0 0
*PART SHEADING
PizeoB
$ PID SECID MID EOSID HGID GRAV ADPOPT TMD
7 1 10 0 1 0 0 0
*PART SHEADING
sphere
$ PID SECID MID EOSID HGID GRAV ADPOPT TMD
10 1 2 1 1 0 0 0
*PART SHEADING
steel 1
$ PID SECID MID EOSID HGID GRAV ADPOPT TMD
11 1 12 1 1 0 0 0
$-----1-----2-----3-----4-----5-----6-----7-----8
$
$ SECTION CARDS
$
$-----1-----2-----3-----4-----5-----6-----7-----8
*SECTION_SHELL
$^P-1
$ SECID ELFORM SHRF NIP PROPT QR/IRID ICOMP SETYP
1 15 1.0 80 0.0 0.0 0 1
$ T1 T2 T3 T4 NLOC MAREA
0.0 0.0 0.0 0.0 0 0.0
$-----1-----2-----3-----4-----5-----6-----7-----8
$
$ MATERIAL CARDS
$
$-----1-----2-----3-----4-----5-----6-----7-----8

```



```

$ ENDTIM ENDCYC DTMIN ENDENG ENDMAS
0.0000080 0 0.0 0.0 0.0
*CONTROL_SOLUTION
$ SOLN
2
*CONTROL_THERMAL_SOLVER
$ ATYPE PTYPE SOLVER CGTOL GPT EQHEAT FWORK SBC
1 0 1 0.00010 0 1.0 1.0 0.0
*CONTROL_THERMAL_TIMESTEP
$ TS TIP ITS TMN TMAX DTEMP TSCP
0 1.03.0000E-08 0.0 0.0 1.0 0.50
*CONTROL_TIMESTEP
$ DTINIT TSSFAC ISDO TSLIM DT2MS LCTM ERODE MS1ST
0.0 0.90 0 0.0 0.0 0 1 0
$ DT2MSF

*CONTROL_REMESHING
$ RMIN RMAX
0.0025 0.0050
*CONTROL_HOURLASS
$ IHQ QH
5 0.10
*CONTROL_CONTACT
$ SLSFAC RWPNAL ISLCHK SHLTHK PENOPT THKCHG ORIEN ENMASS
0.10 2 0 2 1 1 0
$ USRSTR USRFRCS NSBCS INTERM XPENE SSTHK ECDT TIEDPRJ
0 0 10 0 4.0 0 0 0
$ SFRIC DFRIC EDC VFC TH TH_SF PEN_SF
0.0 0.0 0.0 0.0 0.0 0.0 0.0
$ IGNORE FRCENG SKI PRWG OUTSEG SPOTSTP SPOTDEL
0 0 0 0 0 0
$-----1-----2-----3-----4-----5-----6-----7-----8
$
$ DATABASE CONTROL FOR ASCII
$-----1-----2-----3-----4-----5-----6-----7-----8
$
$ *DATABASE_TPRINT
$ DT BINARY
1.0000E-08 2
*DATABASE_MATSUM
$ DT BINARY
1.0000E-08 2
*DATABASE_GLSTAT
$ DT BINARY
1.0000E-08 1
*DATABASE_ABSTAT
$ DT BINARY
1.0000E-08 2
$-----1-----2-----3-----4-----5-----6-----7-----8
$
$ DATABASE CONTROL FOR BINARY
$-----1-----2-----3-----4-----5-----6-----7-----8
$
$ *DATABASE_BINARY_D3PLOT
$ DT/CYCL LCDT BEAM NPLTC
3.0000E-08 0 0 0
$-----1-----2-----3-----4-----5-----6-----7-----8
$
$ PART CARDS
$-----1-----2-----3-----4-----5-----6-----7-----8
$
$ *PART
$ SHEADING
$ WS
$ PID SECID MID EOSID HGID GRAV ADPOPT TMD
2 1 1 1 0 0 0 1
*PART
$ SHEADING
$ solidP
$ PID SECID MID EOSID HGID GRAV ADPOPT TMD
4 2 2 0 0 0 0 2
$-----1-----2-----3-----4-----5-----6-----7-----8
$
$ SECTION CARDS
$-----1-----2-----3-----4-----5-----6-----7-----8
$
$ *SECTION_SOLID
$ ^P-1
$ SECID ELFORM AET
1 1 0
*SECTION_SOLID
$ ^P-2
$ SECID ELFORM AET
2 1 0
$-----1-----2-----3-----4-----5-----6-----7-----8
$
$ MATERIAL CARDS
$

```


This page left intentionally blank

APPENDIX C

MATERIAL PROPERTIES

C.1 Material property specifications

This appendix contains material property information relevant for the study

C.1.1 Material property data sheets for AISI 1020 steel

The following data sheet for AISI 1020 steel was obtained from the Matweb website.

Physical Properties	Metric	English	Comments
Density	7.87 g/cc	0.284 lb/in ³	
Mechanical Properties			
Hardness, Brinell	121	121	
Hardness, Knoop	140	140	Converted from Brinell hardness.
Hardness, Rockwell B	68	68	Converted from Brinell hardness.
Hardness, Vickers	126	126	Converted from Brinell hardness.
Tensile Strength, Ultimate	420 MPa	60900 psi	
Tensile Strength, Yield	350 MPa	50800 psi	
Elongation @ break	15 %	15 %	In 50 mm
Reduction of Area	40 %	40 %	
Modulus of Elasticity	205 GPa	29700 ksi	Typical for steel
Bulk Modulus	140 GPa	20300 ksi	Typical for steel
Poisson's Ratio	0.29	0.29	
Machinability	65 %	65 %	Based on AISI 1212 steel. as 100% machinability
Shear Modulus	80 GPa	11600 ksi	Typical for steel

C.1.2 Material property data sheets for AISI 1006 steel

The following data sheet for AISI 1006 steel was obtained from the Matweb website.

Physical Properties	Metric	English	Comments
Density	7.872 g/cc	0.284 lb/in ³	

Mechanical Properties

Hardness, Brinell	95	95	
Hardness, Knoop	113	113	Converted from Brinell hardness.
Hardness, Rockwell B	55	55	Converted from Brinell hardness.
Hardness, Vickers	98	98	Converted from Brinell hardness.
Tensile Strength, Ultimate	330 MPa	47900 psi	
Tensile Strength, Yield	285 MPa	41300 psi	
Elongation at Break	20 %	20 %	In 50 mm
Reduction of Area	45 %	45 %	
Modulus of Elasticity	205 GPa	29700 ksi	Typical for steel
Bulk Modulus	140 GPa	20300 ksi	Typical for steel
Poisson's Ratio	0.29	0.29	Typical For Steel
Machinability	50 %	50 %	Based on AISI 1212 steel. as 100% machinability. The machinability of Group I bar, rod, and wire products can be improved by cold drawing.
Shear Modulus	80 GPa	11600 ksi	Typical for steel

Electrical Properties

Electrical Resistivity	1.74e-005 ohm-cm	1.74e-005 ohm-cm	Typical for steel
------------------------	----------------------------------	------------------	-------------------

Thermal Properties

CTE, linear 20°C	12.6 μm/m-°C	7 μin/in-°F	0 - 100°C
CTE, linear 250°C	13.5 μm/m-°C	7.5 μin/in-°F	from 0-300°C (68-570°F)
CTE, linear 500°C	14.2 μm/m-°C	7.89 μin/in-°F	from 0-500°C (68-930°F)
CTE, linear 1000°C	13.7 μm/m-°C	7.61 μin/in-°F	0-1000°C
Heat Capacity	0.481 J/g-°C	0.115 BTU/lb-°F	50 - 100°C

C.1.3 Material property data sheets for UHMWPE

The following data sheet for Tivar 1000 UHMWPE was obtained from the Poly Hi Solidur material data catalogue (2001).

Material Selection TIVAR Product Specifications

TIVAR PRODUCT SPECIFICATIONS

Property*	Units	Test Method**	TIVAR 1000	TIVAR Marble/Unblend	TIVAR 1000 Artistic	TIVAR DrySlide	Ceram P	TIVAR 91 Filled
DENSITY	GM/CC	ASTM D-792	0.93	.935 - .945	0.93	0.93	0.964	0.928
TENSILE PROPERTIES								
Yield Strength	PSI	ASTM D-638	3050	2800 - 3553	3000	2770	2800	2600
Tensile at Break	PSI		5800	3600 - 5200	4000	4815	3800	4527
Elongation at Break	PERCENT		200	50 - 350	140	200	300	280
TENSILE MODULUS	PSI	ASTM D-638	120,000	90,100 - 127,500	156,900	118,643	130,970	76,000
FLEXURAL MODULUS (1% SLOPE)	PSI	ASTM D-790B	110,000	86,000 - 101,000	100,000	106,459	99,933	63,818
IMPACT STRENGTH								
Notch Impact		ASTM D-256A	NO BREAK	NO BREAK	NO BREAK	NO BREAK	NO BREAK	NO BREAK
Tensile Impact	FT-LBS/IN ²	ASTM D-1822	715	255 - 540	400	653	750	1366
WEAR PROPERTIES								
Sand on Wheel	MG WEIGHT LOSS	ASTM G-64	100	100 - 250	100	100	85	100
Abrasion Index	1018 STEEL=100	SAND SLURRY	10	10 - 22	10	10	8	12
COEFFICIENT OF THERMAL EXPANSION								
-30° To +60° C	IN/IN/°C	ASTM D-696	2 x 10 ⁻⁴	1.8 X 10 ⁻⁴	2 X 10 ⁻⁴	2 X 10 ⁻⁴	1.6 X 10 ⁻⁴	2 X 10 ⁻⁴
-54° To +140° F	IN/IN/°F		1.1 x 10 ⁻⁴	1 X 10 ⁻⁴	1.1 X 10 ⁻⁴	1.1 X 10 ⁻⁴	.9 X 10 ⁻⁴	1.1 X 10 ⁻⁴
COEFFICIENT OF FRICTION (Polished Steel)								
Static		ASTM D-1894	.15 - .20	.15 - .20	.15 - .20	0.15	0.18	.20 - .25
Kinetic			.10 - .14	.10 - .14	.10 - .14	0.08	0.12	.10 - .15
HARDNESS								
	SHORE D	ASTM D-2240	68	64 - 70	68	68	70	68
ELECTRICAL PROPERTIES								
Static Decay Time	SECONDS	FTS-101C			< 0.1 SEC			
Dielectric Constant		ASTM D-150	2.30 - 2.35					
Dissipation Factor		ASTM D-150	< .5 X 10 ⁻¹					
Surface Resistivity	OHMS	ASTM D-257	10 ¹¹	10 ¹⁰	10 ¹⁰ - 10 ⁹	10 ¹⁰ - 10 ⁹	10 ¹¹	10 ¹¹
Volume Resistivity	OHMS-CM	ASTM D-257	10 ¹¹	10 ¹⁰	10 ¹⁰ - 10 ⁹	10 ¹⁰ - 10 ⁹	10 ¹¹	10 ¹¹
FDA STANDARDS								
			YES	NO	NO	NO	NO	YES
TEMPERATURE RANGE								
MAXIMUM***		ASTM D-648						
CONSTANT	° F		180	180	180	180	220	180
INTERMITTENT	° F		200	200	200	200	240	200
MINIMUM			N/A	N/A	N/A	N/A	N/A	N/A

* Values are averages and not specifications.
 ** ASTM test methods are under current procedures.
 *** Maximum operating temperatures may reach 250°F (121°C) under no load conditions for steam cleaning purposes.

C.1.4 Material property data sheets for VER

The following data sheet for Derakane 441-400 vinyl ester resin (VER) was obtained from Dow plastics (2001).

DERAKANE Epoxy Vinyl Ester Resins Typical Physical Properties

	411-350	441-400	470-300	510A-40	510C-350	510N	8084
LIQUID PROPERTIES							
Epoxy base	Bisphenol-A	Bisphenol-A	Novolac	Brominated Bisphenol-A	Brominated Bisphenol-A	Brominated Novolac	Elastomer Modified Bisphenol-A
Viscosity, cps @25°C	350	400	300	350	350	250	350
Styrene content, wt%	45	33	33	40	35	37	42
PROPERTIES OF 3mm CLEAR CASTINGS							
Tensile strength, MPa	83	90	85	69-76	76-83	69-76	69-76
Tensile modulus, GPa	2.9	3.6	3.6	3.4	3.4	3.4	3.2
Elongation, %	7-8	7-8	3-4	4-5	4-5	3-4	10-12
Flexural strength, MPa	148	165	131	110-124	110-124	124-138	110-124
Flexural modulus, GPa	3.4	3.5	3.8	3.7	3.9	3.7	3.0
HDT, °C	99-104	118	149-154	104-110	104-110	118-124	77-82

REMARKS:

1. The above data are typical properties only, which are not to be construed as specifications.
2. This table does not contain the entire range of DERAKANE® resins. For further information, please contact your local Dow business office.

NOTICE: No freedom from any patent owned by Seller or others is to be inferred. Because use conditions and applicable laws may differ from one location to another and may change with time, Customer is responsible for determining whether products and product information in this document are appropriate for Customer's use and for ensuring that Customer's workplace and disposal practices are in compliance with applicable laws and other government enactments. Seller assumes no obligations or liability for the information in this document. **NO WARRANTIES ARE GIVEN; ALL IMPLIED WARRANTIES OF MERCHANTABILITY, OR FITNESS FOR A PARTICULAR PURPOSE ARE EXPRESSLY EXCLUDED.**



EVERYWHERE YOU NEED PROTECTION.

C.1.5 Material property data sheets for piezo-electric material

The following data sheet for the piezo-electric material PIC 151 was obtained from the PI Ceramics website.

PZT characteristics	PIC 110	PIC 140	PIC 181	PIC 151	PIC 155	PIC 255
Density [gcm ³]	5,60	7,60	7,85	7,80	7,80	7,80
Curie Temperature [°C]	150	330	325	250	345	350
Relative Permittivity $\epsilon_{33}^T / \epsilon_0$ $\epsilon_{11}^T / \epsilon_0$	980	800 680	1200 1500	2400 1980	1500 1400	1800 1650
Dielectric Loss tan δ [$\xi \cdot 10^{-3}$]	15	10	4	15	20	15
Resistivity [$\Omega\mu$]		10^{10}	10^{10}	10^{11}	10^{11}	10^{11}
Coupling Factors k_p k_{33} k_{31}	0,28 0,38 0,17	0,50 0,60 0,25	0,56 0,67 0,32	0,62 0,69 0,34	0,62 0,69 0,35	0,62 0,69 0,35
Mechanical Q_m	350	350	1400	120	80	80
Frequency Constants N_p N_t [Hzm] N_b N_t	2980 2280 2500	2200 1680 1800 2100	2270 1635 2010 2290	2100 1500 1680 1950	1950 1500 1985	2000 1420 2000
Charge Constants [$\times 10^{-12} \text{ mV}^{-1}$] d_{31} d_{33} d_{15}	-55 140	-60 200 265	-120 265 475	-210 450 580	-165 360 450	-180 400 500
Voltage Constants [$\times 10^{-3} \text{ VmN}^{-1}$] g_{31} g_{33}	-6,3 16,1	-8,5 28,2	-11,2 25,2	-11,5 22,8	-12,4 27,0	-11,3 25,1
Elastic Constants [$\times 10^{-12} \text{ m}^2 \text{ N}^{-1}$] s_{11}^E s_{33}^E	8,5	11,7 14,7	11,8 14,2	15,0 19,0	15,6 19,7	16,1 20,7
Aging Rate [% per Time Decade] C_f C_k C_ϵ	+1 -8,5 -5	+0,3 -1,0 -0,25	+0,3 -2 -4	+0,2 -2 -4	+0,15 -2 -3	+0,13 -1 -2,5

